The Pennsylvania State University

The Graduate School

CHEMICAL SOLUTION DEPOSITION OF POTASSIUM SODIUM NIOBATE THIN FILMS

A Thesis in

Materials Science and Engineering

by

Leonard Jacques

Submitted in Partial Fulfillment
of the Requirements
for the Degree of

Master of Science

May 2021

The thesis of Leonard Jacques was reviewed and approved by the following:

Susan E. Trolier-McKinstry
Steward S. Flaschen Professor of Ceramic Science and Engineering
Director, W.M. Keck Smart Materials Integration Laboratory and Nanofabrication Facility
Thesis Advisor

Clive. A. Randall
Director, Materials Research Institute
Professor of Materials Science and Engineering

Veronika Kovacova
Research Scientist

John C. Mauro
Professor of Materials Science and Engineering
Chair of the Intercollege Graduate Degree Program in Materials Science and Engineering

ABSTRACT

Potassium sodium niobate (KNN) shows promise as a lead-free alternative for lead zirconate titanate, a material utilized in piezoelectric thin films. However, the successful production of these films via the Chemical Solution Deposition (CSD) process remains challenging. This thesis presents detailed solution methods for KNN deposition via CSD. It was found that the electrical properties of 0.5% Mn-doped KNN films depended on both the composition homogeneity and the heat treatment. The best films exhibited breakdown fields over 600 kV/cm and showed well-developed ferroelectric hysteresis loops.

The nucleation and growth phenomena in KNN thin films produced by CSD were studied to obtain activation energies for KNN perovskite phase transformation and growth. The films were annealed in a rapid thermal processor (RTP) with a hold step in a temperature range of 500 to 550°C. During early crystallization of KNN films, it was found that individual nuclei grow as circular regions called rosettes. FESEM was used to determine the size of KNN rosettes, the volume fraction crystallized, and the number of rosettes on partially crystallized samples prepared to determine the activation energies for nucleation, growth, and phase transformation. The results show a linear growth rate with rate law exponents of 1.4, 1.3, and 1.1 at 550°C, 525°C, and 500°C, respectively. The rate laws suggest rapid growth, possibly due to excess alkali additions to the chemical solution. The activation energies for perovskite transformation and growth are 687 ± 13 kJ/mol and 194 ± 10 kJ/mol. The effective activation energy for nucleation calculated from these is 493 ± 23 kJ/mol. Crystallization in KNN is nucleation-limited, and the crystallization temperature can be reduced by crystallizing on a seed layer. Energy dispersive spectroscopy (EDS) revealed the segregation of excess sodium acetate during the drying steps and subsequent transformation to oxalates during pyrolysis as the source of composition segregation.

TABLE OF CONTENTS

LIST OF FIGURES

LIST OF TABLES

ACKNOWLEDGEMENTS

I owe thanks to the committee who reviewed my thesis, which is composed of my advisor, Prof. Susan Trolier-McKinstry, Prof. Clive Randall, and Dr. Veronika Kovacova. Prof. Trolier-McKinstry is distinguished as the Steward S. Flaschen Professor of Ceramic Science, a member of the National Academy of Engineering, and co-director of the Center for Dielectrics and Piezoelectrics (CDP). Prof. Randall is the director of the Materials Research Institute at Penn State, and is a former co-director of CDP and was director of its predecessor, the Center for Dielectric Studies, for 16 years. Dr. Veronika Kovacova is well off into a career in ceramic science and continuing work on the electrocaloric effect in PZT and PVDF for piezoelectric applications in Luxembourg.

The undertaking to develop potassium sodium niobate films was a daunting task at first and there was little hope for success. But due to the collaborative efforts of the McKinstry group, this undertaking was successful, with its first glimpses of fruit before the onset of the COVID-19 pandemic. This work was a great collaborative effort between colleagues whose invaluable contributions reared this project in the right direction.

Jung In Yang and her husband, Song Won Ko, have contributed greatly by introducing processes for solution A and solution B. This work would not have been possible without the insight of Song Won Ko who provided advice for these solutions. Veronika Kovacova provided modifications to solution A which turned out to benefit the film density and leakage current properties. Both Jung In Yang and Veronika Kovacova contributed much time towards developing processing conditions for solutions A and B. Thank you Beth Jones and Wanlin Zhu, who introduced me to solution preparation and the art of spin-coating.

I am especially thankful to Bangzhi Liu for his diligent work during the COVID-19 pandemic to take FESEM cross-sections and angled images of rosettes, and for providing

composition maps for the nucleation and growth study when training was not allowed. Thank you TJ Zimundi and Josh Stapleton in MCL for performing FTIR on critical samples during the pandemic, and for going above and beyond in collaborative efforts to analyze the spectra. I am thankful to the whole Materials Research Institute at Penn State for careful instruction, training, and advice.

I owe many "thank yous" to my advisor, Prof. Susan Trolier-McKinstry, whose great patience has allowed me to develop as a scientist. I believe Dr. Trolier-McKinstry's vast wealth of knowledge of materials science and her devotion to students makes for a sure path to success in any undertaking in materials science. I was especially privileged to have her as my advisor. I extend my thanks to the whole community of piezoelectric ceramic and CSD scientists whose work has contributed either directly or indirectly to this thesis.

Thank you, Lionel and Clunie Jacques who only showed love and support for my efforts in graduate school. Most of all, thanks be to Elohim, my Father Ahnsahnghong and Mother Jerusalem, for being with me always.

If I have seen further, it is by standing upon the shoulders of giants.

- Sir Isaac Newton

This project is a portion of the Center for Nanoscale Science, a Materials Research Science and Engineering Center (MRSEC) supported by the National Science Foundation under grant DMR-2011839 (2020 - 2026) and DMR-1420620.

*Findings and conclusions do not necessarily reflect the view of the funding agency.

Chapter 1

Organization of Thesis and Statement of Goals

This thesis summarizes KNN thin film processing via chemical solution deposition (CSD) and contains collaborative efforts to develop a viable manganese-doped KNN solution for the CSD spin coating process. Solutions A and C, as discussed below, show the most promise for further development and use in thin film-based devices.

Developing a successful solution for CSD and mitigating the challenges presented by a system with two volatile components, sodium and potassium, were of particular interest in this study. A literature review was performed to investigate factors that are known to decrease overall film quality such a composition segregation, microstructural defects, secondary phases, and retained organics. Next, a literature review on post deposition heat treatment discusses the effects on microstructure, composition homogeneity, and conductive pathways in KNN thin films.

Chapter 4 summarizes three different solution methods, solution A, B and C, and discusses variances in microstructure, crystallography, and electrical properties. A comparison between one-step pyrolysis and 2-step pyrolysis for solution A, and a comparison of the results produced by annealing in standing air or an oxygen rich environment follows. Chapter 5 discusses nucleation and growth phenomena in KNN thin films deposited from solution C. Activation energies following Johnson-Mehl-Avrami-Kolmogorov (JMAK) kinetics are provided for nucleation, growth, and perovskite transformation.

The ultimate goal of this thesis is to explain the deposition process of KNN thin films via CSD spin-coating, allowing researchers to experiment knowledgeably and produce high quality films with desired results.

Chapter 2

Literature Review

2.1 Introduction

The purpose of this thesis is to determine suitable processing conditions for piezoelectric potassium sodium niobate (KNN) thin films prepared via chemical solution deposition (CSD). This literature review begins with an introduction to the fundamental terminology of piezoelectricity. It then discusses the fundamental issues in KNN processing, including volatile elements and phase segregation. This review also discusses the effect of different solution methods and doping elements on the electrical properties of the resulting films. A historical overview and review of extant data, as reported in the literature, follows.

2.2 Piezoelectricity

Since 1880, when Pierre Curie and Jacques Curie discovered piezoelectricity in a handful of different crystals, scientists have studied the piezoelectric effect [1]. The prefix "piezo" derives from the Greek "πιέζω" which means "to push" or "to squeeze". Piezoelectric materials are a class of materials which couple electric polarization linearly with stress or deformation. The direct piezoelectric effect describes induced polarization in response to a mechanical strain or stress. The converse effect describes a strain that develops in response to an applied electric field.

Piezoelectricity arises from an arrangement of atoms in a non-centrosymmetric crystal structure, with the exception of crystal class 432 [1]. Of the 32 crystal classes, 21 have no center of symmetry. 20 of the crystal classes which exhibit no center of symmetry are piezoelectric. Of

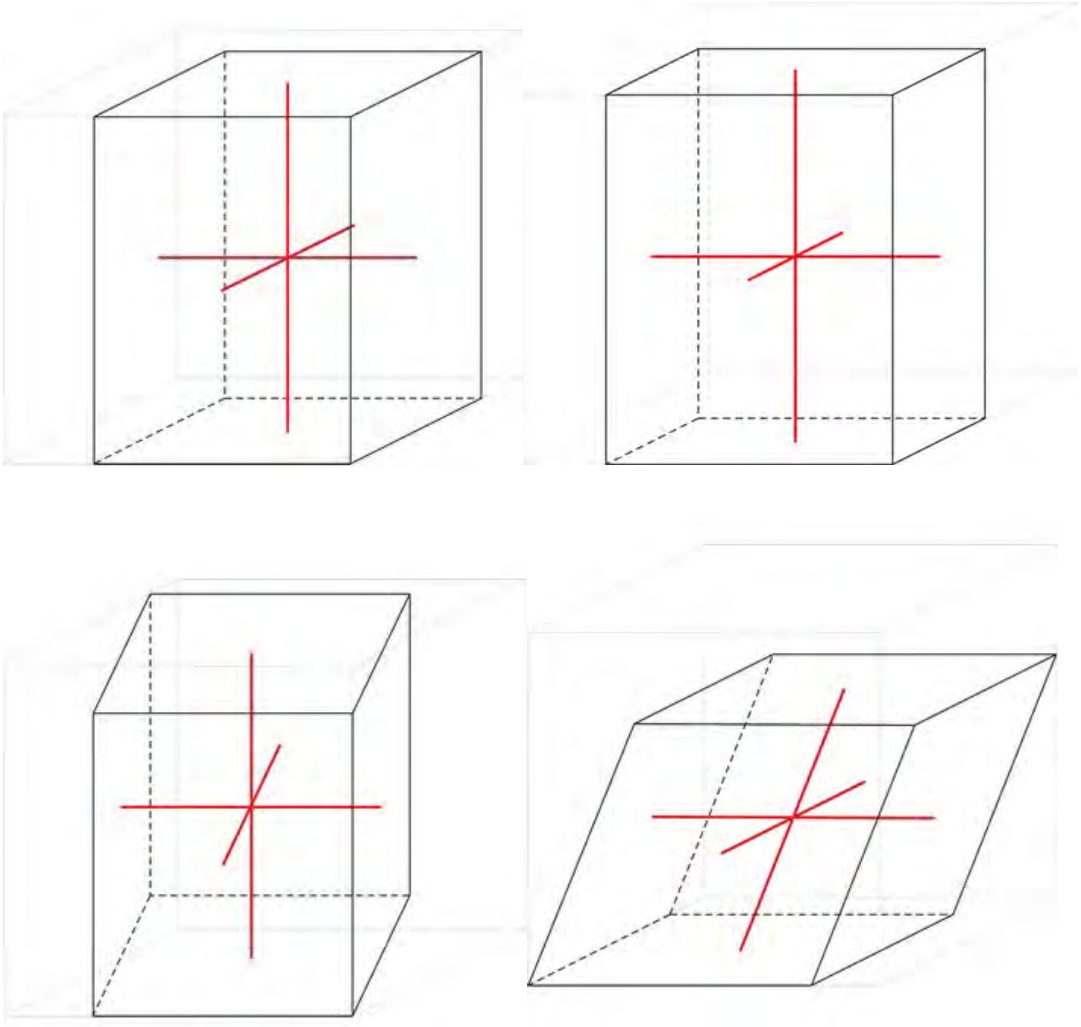

Figure **2-1**: The tetragonal (top left) crystal system has 2 axes of equal length and all three axes are perpendicular to each other. The orthorhombic (top right) structure has no axes of equal length and all axes are perpendicular to each other. The monoclinic (bottom left) structure has no axes of equal length and 2 unit cell angles are 90°. The rhombohedral structure (bottom right) has all sides of equal length and none of the axes are perpendicular to each other, but all the cell angles are the same [2].

the 20 piezoelectric crystal classes, 10 have a unique polar axis and exhibit a spontaneous polarization, because there is a static displacement between the centers of positive and negative

charge. This last group of materials can generate charge when uniformly heated due to a temperature-moderated change in their dipole moment. This class of materials is pyroelectric [3].

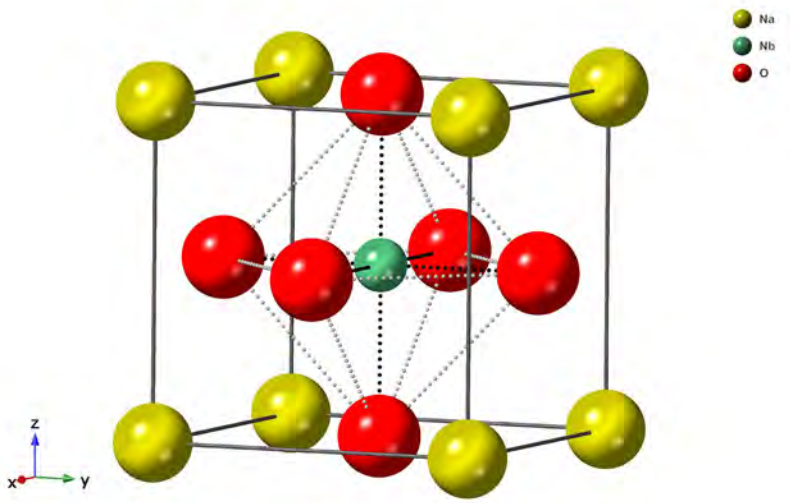

Figure **2-2**: The cubic perovskite structure with space group Pm-3m. The A-site is yellow, B-site is teal, and the oxygen site is red.

Ferroelectricity occurs in a subset of the piezoelectric crystal classes in which there is a spontaneous polarization that can be reoriented between crystallographically-defined directions by an applied electric field. The polarization response exhibits hysteresis upon polarization switching; the hysteresis loop is discussed later in this chapter [4]. Switching depends on domain nucleation and growth. As KNN has the perovskite structure, only the perovskite structure will be discussed here.

2.3 The Perovskite Structure

The prototype perovskite structure is a simple cubic structure with three crystallographic sites: the A site (at the unit cell corners), the B site (in the center of the unit cell), and the O site (on the centers of the faces, see Figure 2-2). The A-site contains positively charged ions with low

valence (often +1 or +2), and relatively large atomic radii. The B-site contains an ion with high valence (often +4 or +5), and small atomic radii. Lead, sodium, potassium, calcium, and barium are A-site ions with +1 or +2 valence. Niobium, titanium, and zirconium are B-site ions with +4 or +5 valence.

In the perovskite structure, piezoelectricity arises from the displacement of the B-site atom from the center of the unit cell toward one of the six oxygen atoms located on or near the face-centers of a pseudocubic unit cell. The resulting net polarization can be changed by an applied stress. In ferroelectric perovskites, a large applied electric field can reorient the direction of the spontaneous polarization. In tetragonal perovskites, such as PZT, this causes the B-site atom to move toward the oxygen atom in closest alignment with the electric field, as seen in Figure 2-3. In the orthorhombic structure the polarization can be in any of 12 directions.

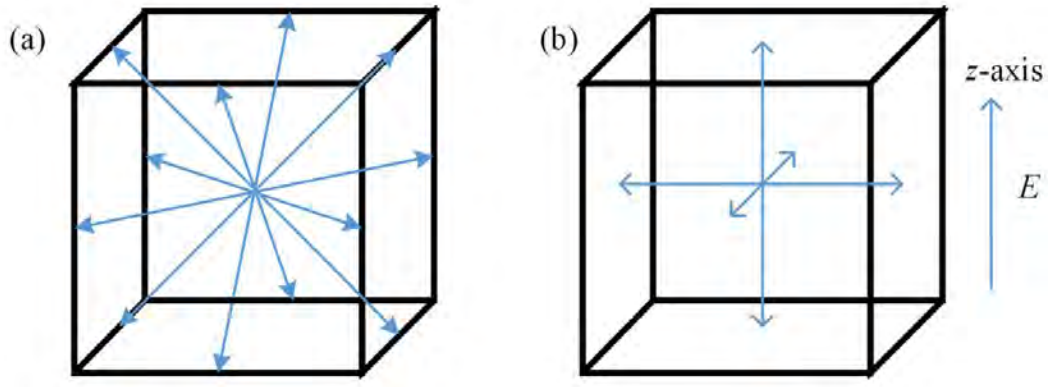

Figure **2-3**: Spontaneous polarization directions in the orthorhombic (left) lattice along the <110> axes, and the tetragonal (right) lattice along the <001> axes [5].

The net piezoelectric response depends on the way all the unit cells distort in response to the applied stress/electric field. There are, in general, two types of ferroelectric materials: extender and rotator ferroelectrics. In extender ferroelectrics (e.g. $PbTiO_3$), the highest piezoelectric coefficients are along the polar axis (discussed later) [4]. “Extender” means the

ferroelectric extends along the polar axis when an electric field is applied parallel to this direction. In rotator ferroelectrics (e.g. $K_{0.5}Na_{0.5}NbO_3$), the highest piezoelectric coefficients are not along the polar axis [4]. “Rotator” means the polar vector rotates in the direction of the applied field, if it is not applied along a polar axis. Because KNN situated at the morphotropic phase boundary (MPB) is a mixture of orthorhombic and monoclinic phases, and the crystallographic anisotropy holding the polarization in a single direction is relatively small, an applied field in the <001> direction will force the polarization vector to rotate from the crystallographically defined <110> direction. Strong polarization rotation is also reported for the monoclinic phases in PZT compositions [6].

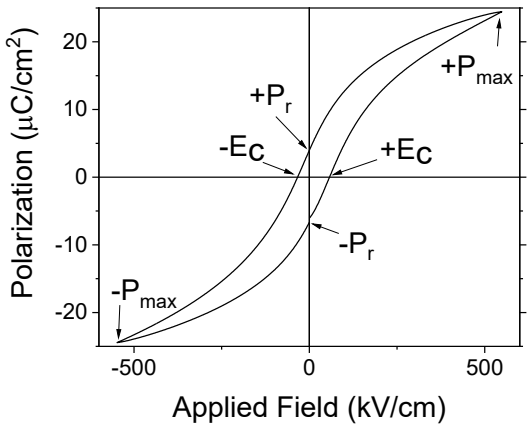

Figure **2-4**: A polarization-electric field (P-E) hysteresis loop of manganese doped potassium sodium niobate. The coercive field, E_c, remanant polarization, P_r, and maximum polarization, P_{max}, are labelled.

The ferroelectricity of a material can be tested by applying a large signal alternating electric field across two electrodes and measuring the change in polarization to observe the hysteretic properties. This is known as a Polarization-Electric field hysteresis loop, or a P-E hysteresis loop (see Figure 2-4). If the material shows a remanent polarization at 0 field ($+P_r$ or $-P_r$), and the polarization direction is defined by the crystallography, then it is considered to be

ferroelectric. A minimum voltage drive is required to reverse the polarization of a ferroelectric; this coercive voltage is used to define the coercive field (E_c). As a ferroelectric is driven to high electric field, the polarization response will exhibit a maximum polarization (P_{max}). Polarization on ferroelectric ceramics is typically measured in $\mu C/cm^2$ and the electric field is measured in kV/cm or kV/mm.

2.4 Piezoelectric Constants and Terms

The dielectric constant or relative permittivity of a material describes its capacitance relative to that of a parallel-plate capacitor with a vacuum dielectric of the same dimensions.

$$C = \frac{\varepsilon' \varepsilon_0 A}{d}$$

where ε' is the relative permittivity, ε_0 is the permittivity of a vacuum, A is the area of the electrodes, d is the thickness of the material between the electrodes, and C is the capacitance. The dielectric constant is related to its electric susceptibility (χ_e) which describes the polarization response of a dielectric to an electric field.

$$\chi_e = \varepsilon' - 1$$

$$P = \chi_e \varepsilon_0 E$$

$$D = \varepsilon_0 E + P = \varepsilon_0 \varepsilon' E$$

where D is the dielectric displacement, P is the polarizability, E is the electric field, and ε' is the total dielectric constant.

Depending on the application, piezoelectrics with both high and low dielectric constants are useful. A piezoelectric with low ε' produces a large electric field across the device when stressed, which enhances the receive sensitivity for voltage-based sensors. On the other hand, the

piezoelectric d_{ijk} coefficients tend to be maximized in materials with high relative permittivities. Thus, for actuators, a piezoelectric with high ε′ is often desired.

Measurements of the dielectric constant are performed under an alternating electric field. In addition to the out-of-phase capacitive components, there is also an in-phase response. The loss tangent describes this.

$$\tan\delta = \frac{\varepsilon''}{\varepsilon'}$$

where ε′ is the real part of the relative permittivity, ε″ is the imaginary part, and δ is the loss angle. The dielectric loss generates loss currents and dissipates energy [7]. Energy dissipation is proportional to both the magnitude of ε′ and tanδ.

$$P = 2\pi f \varepsilon' \frac{V_0^2}{2} \tan\delta$$

where P is the power dissipation, f is the frequency, and V_0 is the maximum voltage. Therefore, a piezoelectric material with high ε′ must have a low loss tangent (tanδ) to avoid significant heating [6].

The piezoelectric response is quantified in the form of coefficients. The direct effect (where stress is converted to charge) and the converse effect (where strain is generated in response to an electric field) are shown below.

$$D = d\sigma$$

$$\epsilon = dE$$

where D is the dielectric displacement, σ is stress, ϵ is strain, and E is the electric field. A list of piezoelectric coefficients follows:

$$d_{ij} = \frac{P_i}{\sigma_j}$$

$$-g_{ij} = \frac{E_i}{\sigma_j}$$

$$-e_{ij} = \frac{P_i}{\in_j}$$

The coefficients “i” and “j” indicate direction in Einstein notation. Direction “3” is the direction parallel to the remanent polarization direction in a ferroelectric that is not a single crystal. Directions “1” and “2” are parallel to the electrode and perpendicular to each other. The symbol $\in$ indicates strain.

In their as-sintered or unpoled state, piezoelectric ceramics do not exhibit piezoelectricity, although individual unit cells have a spontaneous polarization; for the net material, the polarization vectors cancel. Volumes of materials in which the spontaneous polarization are aligned (or at least nearly so) are referred to as “domains”. The polarization vector of an adjacent domain will be one of the allowed polarization directions based on the crystallography, as shown in Figure 2-3. In the case where the sum of the polarizations in the domains cancel each other out, no net piezoelectric response is generated.

To make such a material piezoelectric, it must be poled, such that a strong electric field is applied, typically at an elevated temperature, to orient the domains in the direction of the applied electric field. Since poling typically drives the bulk ferroelectric material from equilibrium, the magnitude of the piezoelectric effect decays over time as some domains reorient to lower energy configurations; this is referred to as aging. The piezoelectric effect can be recovered by poling the material again. In this work poling was performed on thin films under a DC field at nearly three times the coercive field [8]. Recently, it was reported that AC poling at low frequencies is effective for bulk materials [7].

The properties of many piezoelectric materials are temperature dependent [9,10]. Above the Curie Point, most ferroelectrics revert to a non-polar state [11]. In the KNN system, the cubic space group Pm-3m exists above the Curie point [11], as shown in Fig. 2-5. Below the Curie point, KNN becomes tetragonal (space group P4mm). At temperatures near 200°C, KNN becomes either monoclinic (space group Pm) or orthorhombic (space group Amm2), depending on composition. Some KNN samples become rhombohedral at low temperatures (space group R3c or R3m), depending on the composition.

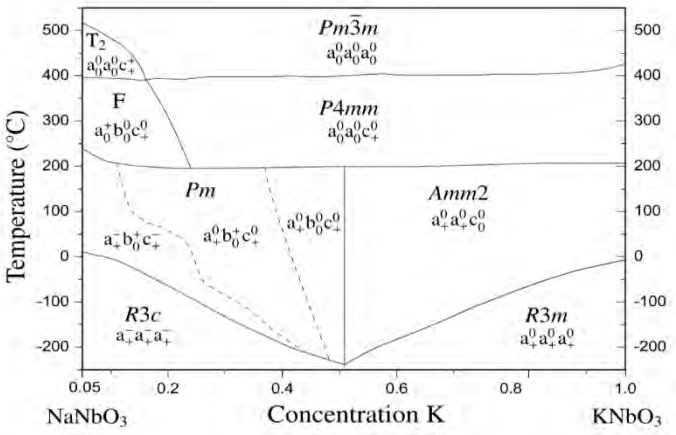

Figure **2-5**: A phase diagram of the $KNbO_3$ – $NaNbO_3$ solid solution [11].

Anomalies in piezoelectric coefficients are expected in the vicinity of phase transitions. Phase transitions can be driven by either temperature or composition. A temperature dependent phase transition occurs at a polymorphic phase boundary. A composition driven phase transition occurs at a morphotropic phase boundary (MPB). For example, at room temperature, lead zirconate titanate shows a significant increase in piezoelectric coefficients at the nearly temperature-independent boundary between the rhombohedral and tetragonal phases, at its MPB composition; 52 at.% Zr and 48 at.% Ti [1,3]. At this phase boundary, the material polarizability increases, as do domain wall contributions to the properties [1,3].

At room temperature, KNN exhibits a MPB at composition near 50 at.% K and 50 at.% Na (see Figure 2-5). The transition is between a monoclinic phase and an orthorhombic phase, with a small change in the beta angle from 90.26° in the monoclinic phase to 90° in the orthorhombic phase [11]. While not a universally accepted model, KNN's strong piezoelectric properties have been reported to be associated with a maximum in local structural disorder near the 50:50 Na:K composition [12]. Work in PZT has ascribed part of the piezoelectric anomaly at the MPB to the appearance of monoclinic phases which facilitates polarization rotation [13,6,14]. If this is applied in KNN, the piezoelectric anomaly at the MPB (see Figure 2-6) may be enhanced by the monoclinic phase on the sodium rich side of the boundary (see Figure 2-5).

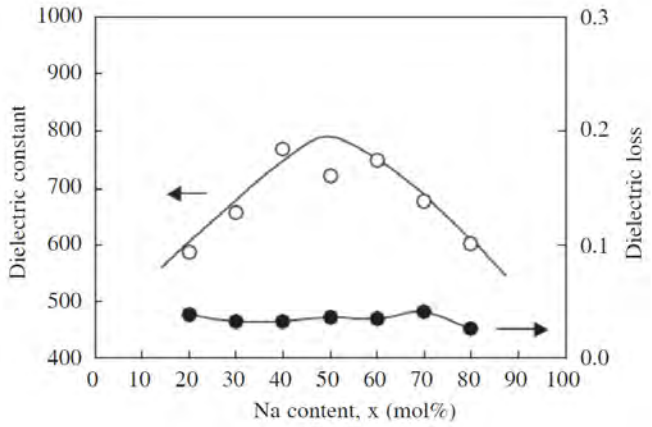

Figure **2-6**: Composition dependence of the dielectric constant in spark plasma sintered KNN shows evidence of an MPB near 50:50 Na:K composition [15].

2.5 CSD: A Solution Approach to Film Synthesis

In this thesis, chemical solution deposition (CSD), specifically using the spin-coating method, was employed for film growth. Thus, this section details important mechanisms in the

CSD process. The first step in the CSD process is making a solution suitable for deposition. This involves choosing the right solvent, precursors, and if necessary, adding a chelating agent to increase the shelf-life and stability of the solution. Herein, key characteristics of the solution that are known to affect the resulting metal-oxide thin film are discussed.

Beginning with the solvent, it is important to choose a polar solvent with adequate solubility for the cations of interest and a low boiling point. A common solvent for non-aqueous based solutions is polar 2-methoxyethanol, or 2-MOE. 2-MOE was chosen for this work because it can dissolve a wide variety of materials and is able to form stable solutions [16]. A less toxic replacement for 2-MOE is 2-butoxyethanol [17].

The alkali metals sodium and potassium can be introduced to the solvent in their respective acetate or ethoxide salts. These metal-organic precursors can be dissolved in 2-MOE at room temperature via mixing. Niobium ethoxide, a liquid at room temperature, can be added to 2-methoxyethanol, and upon mixing with alkali acetates or ethoxides forms new compounds in the solution. Long reflux times up to 70 hours and at elevated temperatures above 100°C are necessary to react niobium ethoxide with the alkali precursors in the solution [18,19,20]. Reaction side products include acetic acid and ethanol from the alkali acetate precursors and the ethyl group on the niobium precursor (see Figure 2-7). If ethoxide precursors are used, their side product is ethanol.

Under heated mixing or refluxing, ethanol boils out of the solution immediately due to its low boiling point of 78°C. The boiling point of acetic acid is 118°C, which is 6°C below the boiling point of 2-MOE. Exposing the mixture of 2-MOE and acetic acid to temperatures around 120°C can result in esterification, forming large precipitates and making the solution unfit for deposition [21]. Therefore, when using acetate precursors, a reflux temperature below 120°C allows acetic acid to remain in the solution without forming large esters. In situations where

acetate precursors can limit the reflux temperatures, vacuum distillation is the preferred method to remove acetic acid from the solution [22].

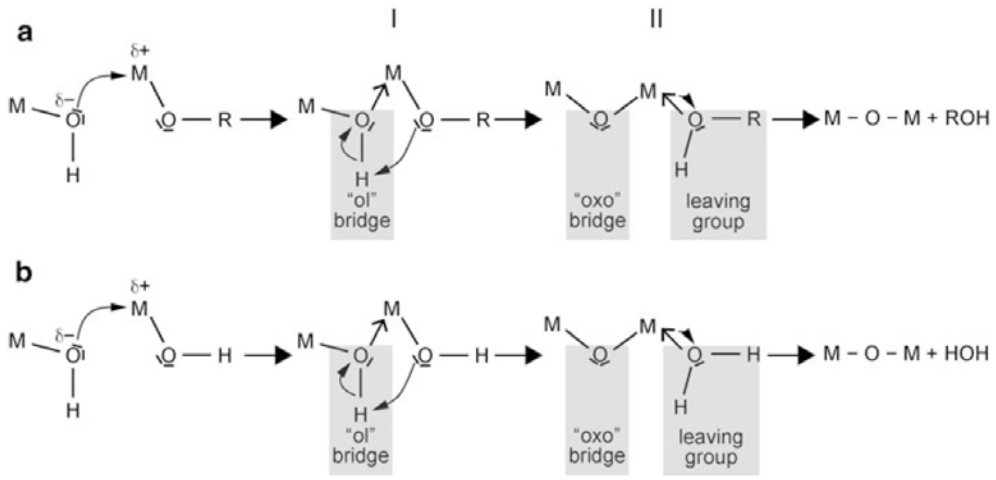

Figure **2-7**: A schematic of the condensation process where nucleophilic attack occurs in alkoxylation (a) and oxolation (b) and results in the M-O-M linkage and leaving group [23]. Common R-OH leaving groups in KNN solutions are ethanol and acetic acid.

Use of sodium and potassium acetate favors a lower crystallization temperature than their respective ethoxides [24]. The acetate leaving groups from alkali precursors also act as a stabilizing chelating agent in KNN solutions by reducing the reactivity of niobium ethoxide, especially with water which would cause it to precipitate [17,25]. Chelating agents help make viable solutions for CSD by preventing precipitation of metals from solution [26].

Proper mixing of the precursors in the solvent is required to produce a homogeneous solution [16]. In PZT, it was reported that mixing the A-site and B-site precursors separately favors a homogeneous distribution of the two B-site ions, Ti^{4+} and Zr^{4+} [26]. Then the A-site (Pb) is added to the B-site (Ti, Zr) precursor solution. The opposite order has been used for KNN solutions, where the acetate or A-site precursors are mixed separately from Nb-ethoxide, then the Nb-ethoxide mixture is added to the first mixture [27,28,29,30]. After mixing precursors, they

must be refluxed, which is a form of mixing where evaporated liquids continuously condense and return to the flask. Refluxing the solution for the proper amount of time is important, so the precursors react to form metal-oxygen-metal (M-O-M) linkages (see Figure 2-7). The formation of M-O-M bonds is favored over long reflux times [18]. Compared to the titanium isopropoxide and zirconium propoxide precursors for PZT, niobium ethoxide is significantly more difficult to react with 2-methoxyethanol; in principle, the reaction should replace ethoxide groups with 2-methoxyethoxide groups [16]. In the $K(Ta,Nb)O_3$ system, the formation of oligomers between K and Nb saturated after 24 hours of refluxing [31]. Only solutions with adequate formation of K-O-Nb-O-… bonds formed single phase films, whereas films from the solution refluxed for only 1 hour experienced composition segregation and had heterogeneous microstructures.

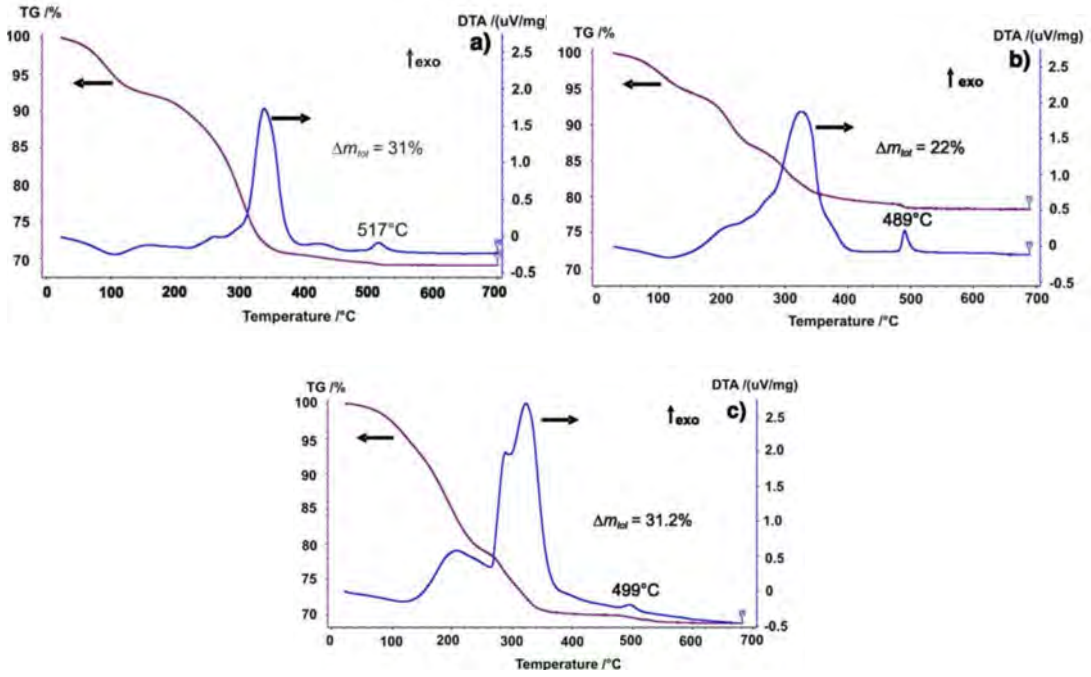

Figure **2-8**: TG/DTA profiles of $Na_{0.5}Bi_{0.5}TiO_3$ solution (a) refluxed at 124°C with acetylacetone, solution (b) refluxed at 124°C without acetylacetone, and solution (c) refluxed at 30°C without acetylacetone [19].

Choice of reflux temperature is also important. For a $Na_{0.5}Bi_{0.5}TiO_3$ solution process, it is reported that higher reflux temperatures are more conducive to making ferroelectric films than low reflux temperatures [19]. In that work, a reflux temperature of 124°C was chosen to eliminate esters from the solution. Compared to a reflux temperature of 30°C under vacuum, the improved ester elimination in the 124°C reflux resulted in an insulating film with measurable electrical properties. This was attributed to the removal of unnecessary organic species before deposition or "gelation", where a M-O-M matrix begins to form. The mass loss reported from thermogravimetric analysis (TGA) shows approximately 50% greater mass loss in the low reflux temperature solution, compared to the high temperature solution (see Figure 2-8). The low temperature reflux solution also had a crystallization temperature 10°C higher than the high temperature reflux because it had a greater retained organic content. Additionally, excess organic species in solution can lead to phase segregation.

From the same report [19], the use of the chelating agent acetylacetone combined with refluxing at 124°C results in $Na_{0.5}Bi_{0.5}TiO_3$ films with high leakage currents. Similar to the solution with low reflux temperature, the film with acetylacetone had a greater amount of retained organic content due to the chelating β-diketonate ligands introduced by acetylacetone. These ligands are known to be difficult to pyrolyze [32]. Consequently, the TGA profile for this solution showed a delayed mass-drop and a crystallization temperature 28°C higher than the high temperature reflux solution without acetylacetone (see Figure 2-8). Crystallization of a pyrochlore secondary phase before the perovskite phase occurred from this solution.

Next, the reactions of metalorganic precursors with solvent and chelating agents in solution is discussed in detail. Reactions of Nb-ethoxide with acetic acid and acetylacetone (Hacac), respectively, are shown below [33].

$$Nb(OC_2H_5)_5 + xCH_3COOH \rightarrow Nb(OC_2H_5)_{5-x}(CH_3COO)_x + xC_2H_5OH$$

$$Nb(OC_2H_5)_5 + xHacac \rightarrow Nb(OC_2H_5)_{5-x}(acac)_x + xC_2H_5OH$$

This shows that the amount of chelating agent added to the solution will affect the chemistry of the final solution. One molar equivalent of acetylacetone is known to react fully with niobium ethoxide, whereas greater ratios of acac:Nb result in free acetylacetone in the solution [16]. Three molar equivalents of acetic acid has been found to be beneficial in the syntheis of niobium oxide thin films by a CSD method [31]. Ethanol (C_2H_5OH), a by-product of both reactions, with a low boiling point of 78°C can be boiled off and distilled during the reflux step. Distillation of ethanol is known to drive the reaction of niobium ethoxide with the solvent, 2-methoxyethanol (C_3H_8O), to replace the ethoxide (C_2H_5O) groups on Nb with 2-methoxyethoxide (C_5H_7O) groups [16]. This reaction is preferable for the best solution homogeneity:

$$Nb(OC_2H_5)_5 \xrightarrow{C_3H_8O_2} Nb(OC_2H_5)_{5-x}(C_3H_7O_2)_x + xC_2H_5OH$$

Low acetic acid content favors bridging chelating complexes, and a high acetic acid to B-site ratio will form monomeric unidentate, or non-bridging structures in solution [33], which is counterproductive to forming M-O-M linkages. Use of acetylacetone is especially important to consider in complexes involving a Nb-ethoxide precursor, since Nb-ethoxide reacts very slowly with the solvent 2-MOE. Acetylacetone can speed its reaction with 2-MOE, but the chelating ligands remain bound to Nb, thus limiting its potential to react fully with the solvent, and requiring pyrolysis at high temperatures, which is counterproductive to forming homogeneous films [16,19]. Another way to drive the reaction of Nb-ethoxide with 2-MOE is increasing the molar ratio of solvent in the absence of acetylacetone. Excess solvent in the presence of acetylacetone hinders its reaction with Nb-ethoxide.

$$Nb(OC_2H_5)_5 + xHacac \xrightarrow{C_3H_8O_2} Nb(OC_2H_5)_{5-x-y}(C_3H_7O_2)_x(acac)_y + (x+y)C_2H_5OH$$

In summary, a careful selection of solution parameters is critical to producing a ferroelectric KNN film with decent electrical properties. Long reflux times and high temperatures

are generally preferred to react the rate limiting constituent – niobium ethoxide – with the rest of the solution [16]. The reaction with solvent 2-MOE can be driven and the final solution can be stabilized by the introduction of a chelating agent, such as acetylacetone.

2.6 Heat Treatment and Crystallization

This section discusses various factors during heat treatment that affect the resulting film, including pyrolysis, consolidation steps (-OR and -OH removal), atmospheric effects, intermediate phases, free energy considerations, nucleation and growth, and competing kinetics during crystallization.

After the solution is made and stored for the proper amount of time to allow slow reactions to complete, it can be used for spin-coating. The solution should be uniformly deposited on the substrate. The solution can be deposited dropwise while the substrate spins at a few hundred RPM. This step is followed by ramping to a few thousand RPM and remaining at that speed for the remainder of the spin cycle. Both higher spin speed and longer spin time result in a thinner coating. The main events during the spin cycle are fluid flow and solvent evaporation [17]. By the end of this step, the viscosity of the coated layer has increased significantly, and flow has nearly stopped. The as-spun layer is usually below 1 μm in thickness, and it may undergo over 70% consolidation throughout the heat treatment process until it is fully crystallized (see Figure 2-9) [17].

Immediately after spin coating, the substrate is placed on a hotplate for drying. The purpose of drying is to evaporate the remaining solvent, water, and hydroxyl groups from the film [17]. Thermogravimetric analysis (TGA) and evolved gas analysis (EGA)/mass spectrometry (MS) measurements on powders and xerogels from solutions show water evolution (more

generally solvent evolution) at temperatures of 200°C, and this is characterized by an endothermic peak in differential scanning calorimetry (DSC) data [17].

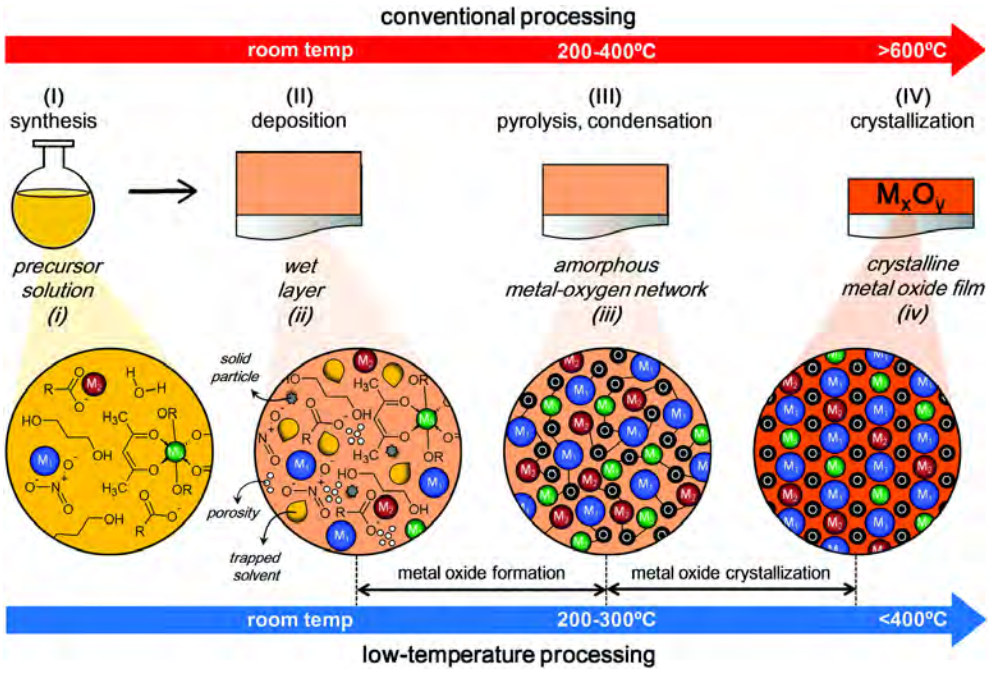

Figure **2-9**: A summary of steps from solution to final crystalline thin film in the chemical solution deposition process [34].

After the drying step, an amorphous film remains, consisting of metals bound to organic functional -OR groups (e.g. acetate and alkoxide (ethyl) groups) [17]. Higher temperatures from 250°C to around 500°C are required to further consolidate the film by removing these groups. This step is called “pyrolysis”. Ideally, removal of these groups in an oxidizing environment results in CO_2 gas and water evolution. However, regions of low oxygen partial pressure over the film can create locally reducing environments. Thermolysis, which is pyrolysis in the absence of oxygen [17], occurs in these regions. Thermolysis can cause defects to form and will be discussed in more detail later in this section.

Appropriate temperatures for pyrolysis vary by solution. A general rule is that shorter organic molecules with lower boiling points will pyrolyze at lower temperatures than larger organic molecules with higher boiling points. As mentioned in the previous section, KNN solution modified with acetylacetone, which also has a higher boiling point than 2-MOE and acetic acid, delays the mass drop on TGA to higher temperatures [19,32]. Therefore, solutions modified with acetylacetone will require higher pyrolysis temperatures than unmodified solutions.

Pyrolysis must precede crystallization because remaining organics and residual carbon will raise the crystallization temperature and affect almost every aspect of the film thereafter [17]. If either the pyrolysis temperature is too low, or the pyrolysis time is too short, high amounts of gas can evolve quickly at the beginning of the crystallization step and cause porosity. In some systems where high pyrolysis temperatures are required to remove organic groups and residual carbon, it is detrimental to the film to immediately subject it to high temperatures [35]. In this case, it is better to perform two pyrolysis steps, one at a lower temperature, and another at a higher temperature. Cracking in the final film can be avoided by performing gradual decomposition steps following this method.

Ideally, at the end of pyrolysis, a dense amorphous film with M-O-M linkages should exist. A dense film minimizes the distance species have to diffuse through the film to crystallize, and minimizes the chance of pores forming. Therefore, significant improvements in film density can result from a carefully optimized pyrolysis procedure.

The last heat treatment step is crystallization of the amorphous film. For many perovskites, this process can occur at temperatures above 550°C in conventional processes and at lower temperatures in assisted processes, as discussed later. The minimum temperature required for crystallization can be determined by differential scanning calorimetry (DSC) measurements on dried powders or xerogels from the solution. The crystallization temperature is identified by an

exothermic peak after the pyrolysis peak. Films annealed under the crystallization temperature indicated by DSC sometimes show weak XRD peaks [36]. Many simultaneous processes occur during crystallization including nucleation, growth, densification, interdiffusion, loss of volatile alkali components to the atmosphere (in KNN and some other perovskites), and, in some cases, transformation of and from intermediate species [17].

The first step of crystallization is nucleation. A nucleus is the precursor of a crystal [37]. There are two types of nucleation: homogeneous nucleation and heterogeneous nucleation. Homogeneous nucleation describes the formation of a nuclei with equal probability throughout the bulk of the film. Heterogeneous nucleation is the formation of nuclei on a pre-existing surface, such as a substrate or a previously crystallized layer. In some systems, heterogeneous nucleation is desired to preferentially orient crystalline layers of film from the substrate [38,39]. This is most favorable when the lattice spacing of the substrate or previous layer matches that of the crystalizing film, to produce “epitaxial” growth. On the other hand, homogeneous nucleation produces randomly oriented films. Increased wettability of the solution to the substrate increases the probability of heterogeneous nucleation [38].

Once a nucleus reaches a critical size, it grows at the rate that atoms diffuse to the interface at its surface. Because of the anisotropy in thin films, much of the growth occurs in directions parallel to the substrate. If a specific orientation is desired, it must nucleate from the substrate and grow across the film surface before crystals with another orientation nucleate homogeneously and grow. This is easiest in systems where the activation energy for nucleation is much higher than that for growth. In some systems, nuclei from the substrate and from the bulk of the film or the top surface can grow simultaneously to crystallize into a randomly oriented film. There are fast growing planes and slow growing planes in crystals, so the growth rate is anisotropic. For example, in KNN the {100} family which controls the morphology is the slowest growing plane family, and the {110} family grows faster since it has more dangling bonds for

atoms to attach [38,40]. When {100} preferential orientation is desired, grains with this orientation must nucleate and spread across the substrate first. Films grown on a substrate that encourages epitaxial growth can be post-annealed to recrystallize them from the substrate, as in the case of $KNbO_3$ on $SrNbO_3$ [41,42]. Further efforts to preferentially orient thin films are mentioned later in this literature review.

The remainder of this section discusses phenomena during pyrolysis and crystallization which may be important to consider for the KNN system. Many problems with ferroelectric films come from unwanted composition segregation, undesirable intermediate phases during processing, residual secondary phases, and porosity.

Composition segregation can occur during nucleation for solid solutions if one phase nucleates before another phase [17]. This can be overcome by ramping to the desired crystallization temperature with a rapid thermal annealer (RTA) if the constituents are not bound by some organic phase or residual carbon [20,23]. Nucleation behavior can be controlled via solution methods by choosing modifications that delay organic removal [17].

Thermolysis occurs where there is locally low pO_2 and can cause defects. Elemental metal can form in locally reducing conditions due to the formation of carbon monoxide from combustion in low pO_2 regions [43]. In one example involving PZT, rapid pyrolysis to 400°C caused the formation of metallic Pb, while pyrolysis at 300°C did not produce the metallic phase. Rapid pyrolysis can facilitate incomplete combustion and evolve CO gas, which is a strong reducing agent. Metallic or reduced phases present in the film have high mobility and can segregate to grain boundaries and behave as a conductive pathway to reduce the resistivity of films, as has been reported in KNN [43].

Much of the crystallization phenomena can be described by free energy considerations [17]. Volume free energy, ΔG_v is the difference between the free energy of the amorphous (dried) film and the crystalline film. ΔG_v increases with an increase in the volume of the amorphous

phase. The number of side -OH groups and -OR groups can increase the volume of the amorphous phase, thereby increasing ΔG_v. Increase in ΔG_v equates to a more exothermic crystallization reaction. This means crystallization will be more favorable. Nucleation is so sensitive to changes in the volume free energy that a 10% increase in ΔG_v can correspond to a nearly 10-fold increase in the nucleation density at 600°C [17]. Note that the magnitude of ΔG_v is dependent on the organics that can be removed from the film, so only the addition of groups that can easily be removed during the crystallization step can increase ΔG_v. Remaining organic groups and residual carbon decrease ΔG_v and hinder nucleation because they cannot be removed at once. However, adding -OH groups to the amorphous film can increase ΔG_v since they are easier to remove from the film [17]. For this reason, introducing water vapor to the anneal environment increases the thermodynamic driving force for crystallization and may improve densification [44,45,46,47,48]. Below is an example of how hydrated species in $BaTiO_3$ aid crystallization by increasing the thermodynamic driving force [44].

$$BaO + TiO_2 \rightarrow BaTiO_3 \quad \Delta H = -162.1 \frac{kJ}{mol}$$

$$Ba(OH)_2 + TiO_2 \rightarrow BaTiO_3 \quad \Delta G = -180 \frac{kJ}{mol}$$

As can be seen, $BaOH_2$ will have a higher driving force for cyystallization than BaO. Keeping the same principle in mind, it is apparent that formation of a secondary phase can reduce the thermodynamic driving force for crystallization. A secondary phase can nucleate first if its nucleation is kinetically favored, even if the primary phase has a lower free energy.

The well-known PZT system will be used as an example to explain the formation of secondary phases. In PZT, pyrochlore nucleates outside the composition tolerance of the perovskite phase. Although the perovskite phase is quite tolerant of non-stoichiometry [8], the

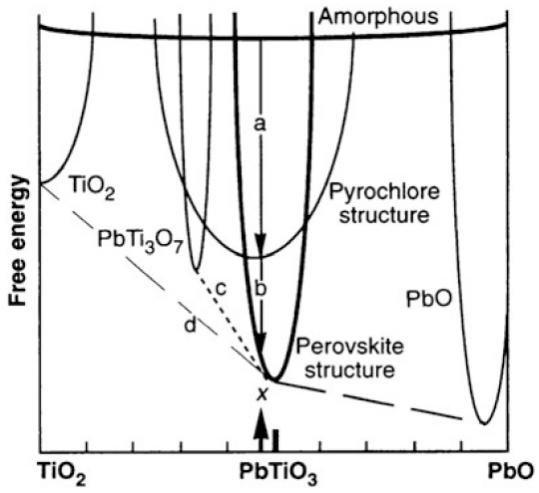

Figure **2-10**: A free energy diagram of $PbTiO_3$ with varying composition in between 400°C and 800°C. From reference [49].

pyrochlore phase accepts even greater non-stoichiometry (see Figure 2-10). As seen in Figure 2-10, formation of a pyrochlore phase first reduces the thermodynamic driving force for crystallization of the perovskite phase, compared to crystallization directly from amorphous $PbTiO_3$. Formation of a secondary phase before the perovskite phase can have a significant effect on the microstructure. For example, the formation of an oxycarbonate phase in the $BaTiO_3$ system delays crystallization and results in larger grains due to a lower nucleation density [50,51].

To summarize this section, final film properties depend strongly on heat treatment. Locally low oxygen partial pressures, which are common with rapid ramping to high pyrolysis temperatures (~400°C), should be avoided to prevent evolution of CO gas, a strong reducing agent. Formation of intermediate phases can generally be avoided by avoiding composition segregation and enabling timely removal of organics, to maximize the driving force for crystallization.

2.7 Special Conditions in Potassium Sodium Niobate

The processing of potassium sodium niobate differs from many other ABO_3 type perovskite films due to its two volatile alkali metal constituents with variable reaction and diffusion rates. Researchers report that care is needed to design the KNN processing route to achieve a phase pure perovskite KNN [52].

Potassium sodium niobate films are highly conducive to forming organic intermediates that are difficult to decompose. Sodium and potassium acetates are notably different from other acetate salts because they decompose into oxalates as an intermediate before decomposing into the final carbonate [17,53]. Further, reactions of the B-site transition metal may promote formation of an oxalate intermediate phase. V_2O_5, from the same transition metal group as Nb on the periodic table, is a known catalyst for oxalic acid [54]. Amorphous niobium oxide below 500°C, also referred to as niobic acid, is an effective solid catalyst [55,56]. Therefore, catalytic activity of niobic acid toward the formation of oxalates is possible during pyrolysis and prior to crystallization. If water is introduced to the system, NaOH and KOH become good fluxes for oxalic acid production [54,55]. It is difficult or impossible to avoid the oxalate phase when working with sodium and potassium acetates over amorphous niobium oxide.

Furthermore, understanding the diffusion of sodium and potassium in niobium oxide is critical to understanding composition segregation in KNN. Potassium and sodium diffuse through niobium oxide at different rates, and it was found that KNN ceramics with small grains have the best homogeneity [52]. When sodium and potassium are reacted together with niobium oxide, they are more likely to produce the perovskite phase with a (K+Na)/Nb ratio of 1, than when reacted separately (see Figure 2-11). When a stoichiometric mixture of potassium and sodium carbonates is reacted with Nb_2O_5 in a diffusion couple, stoichiometric KNN is favored at the

interface and to some critical length depending on the time and temperature for diffusion, shown in Figure 2-11.

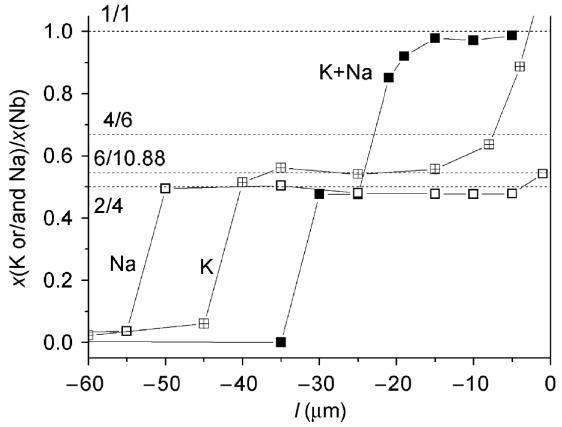

Figure **2-11**: Sodium carbonate (Na_2CO_3), potassium carbonate (K_2CO_3), and together reacted with niobium oxide (Nb_2O_5) reacted in a diffusion couple [52].

When reacted separately, potassium tends to diffuse more extensively at the interface of Nb_2O_5 and is apt to form the potassium excess $K_4Nb_6O_{17}$ phase due to high concentrations of potassium near the couple interface. Sodium diffuses into Nb_2O_5 at a relatively consistent concentration to some critical length at a Na:Nb ratio of 1:2, which is stoichiometric for KNN at the MPB. As a result, sodium is less likely to form secondary phases in KNN. Segregation of potassium to ratios of K:Nb = 0.7:1 favors formation of $K_4Nb_6O_{17}$. Sintering time and temperature can be increased to promote compositional homogeneity [52].

Prior reports show that the insulating properties in KNN films may depend on the niobium oxide component [31]. Thus, the chemical solution deposition process for niobium oxide thin films is of interest. Here, thin films deposited from niobium ethoxide mixed with 2-methoxyethanol and chelating agents acetic acid or acetylacetone were studied. The electrical properties were dependent on the chelating agent, their molar equivalent, and the molar ratio of H_2O:Nb added to the solution. Controlled hydrolysis was reported to have a profound effect on

the electrical properties of chemical solution derived niobium oxide thin films [31]. This effect is mainly due to the enhanced removal of organics from the film during crystallization. While acetylacetone is an effective stabilizing agent, preventing hydrolysis of niobium within the solution, the addition of acetylacetone to niobium is detrimental to the insulating properties. Without the addition of acetylacetone, the threshold field increases with the addition of water up to 1 equivalent H_2O per Nb. The threshold field is the maximum electric field applied before an appreciable gradual rise in the leakage current density occurs. This is different from a breakdown field where an instantaneous rise in current of several orders of magnitude occurs. Low threshold fields were associated with porous and non-uniform microstructures, while dense films and smooth surfaces were associated with high threshold fields. The latter was not achieved from acetylacetone modified solutions without the addition of 1 mol H_2O per mol Nb. In this case, an average threshold field of about 350 kV/cm was reached [31].

On the other hand, the addition of 3 mol glacial acetic acid per mol Nb was beneficial to the electrical properties without the addition of water [31]. A maximum average threshold field of 550 kV/cm was observed at this ideal molar ratio. The addition of acetic acid still resulted in residual carbon after pyrolysis. Nevertheless, the pyrolyzed film was highly susceptible to hydrolytic decomposition, even with a short exposure to the humidity in ambient cleanroom air prior to crystallization, which improved densification and electrical properties [31].

2.8 UV Assisted Crystallization

For some applications, conventional pyrolysis and crystallization temperatures are too high [34,46]. Ultraviolet light radiation can break atomic bonds, facilitating the removal of organic species from the film at lower temperatures (350-500°C) than conventional processing temperatures (600-750°C) [33,57,46]. The crystallization temperature decreases when organic

functional groups and residual carbon are eliminated. Some amorphous films can be exposed to ultraviolet light at a lower-than-normal pyrolysis temperature (~250°C) to break bonds with organic functional groups (-OR) and promote densification by forming a metal oxide matrix [46]. After this, the film can proceed to crystallization at a relatively low temperature (~450°C) [46]. UV assisted pyrolysis is most effective when photosensitive precursors, such as acetylacetone, are used [34].

2.9 Volatile Alkali Metals and Alkaline Oxides

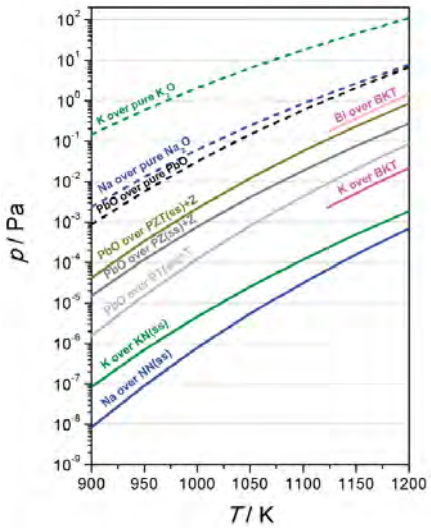

Figure **2-12**: Vapor pressures of potassium, sodium, and lead over their respective oxides [58].

In the KNN system, the loss of volatile alkali ions during heat treatment has a profound effect on the resulting films. Typically, between 10 and 20% excess of alkali precursors are added to the solution to compensate for alkali loss during heat treatment [59,36]. The literature suggests that the most significant loss of alkali metals occurs before crystallization, during pyrolysis or the anneal step before all the amorphous phase crystallizes [58]. A Knudsen cell experiment on KNN

powder conducted under vacuum showed that after 21 hours at 890°C and an additional 23 hours at 990°C there was a 5 mol % loss of potassium and about a 0.5 mol % loss of sodium from KNN powder (see Figure 2-12). The evaporation rates in air were found to be 50 times lower than that in a vacuum. Therefore, extensive loss of volatile sodium and potassium from perovskite KNN is unlikely at conventional thin film crystallization temperatures.

Emphasis should be placed on the observation that most of the volatility of alkali ions is during heat treatment prior to crystallization. TGA-MS was performed on dried gels from KNN solutions modified with monoethanolamine (MEA), diethanolamine (DEA), and ethylenediaminetetraacetic acid (EDTA) at different ratios [60]. All of them showed release of atomic masses corresponding to NaO^- and KO^- between 200°C and 550°C in the mass spectrometer data (see Figure 2-13). NaO^- was detected at a lower temperature than KO^- for all mixtures of MEA, DEA, and EDTA. Onset of crystallization was observed between 510 and 540°C, accompanied by an exothermic peak, for the solution prepared with MEA, DEA, and

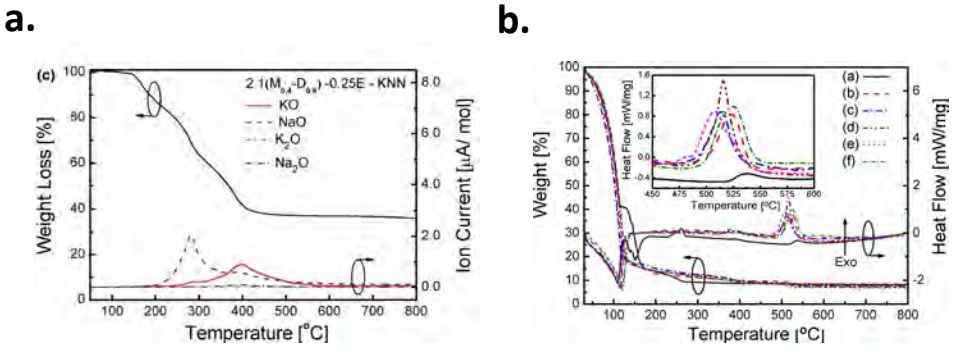

Figure **2-13**: TGA-MS (a) and TGA-DSC (b) of CSD KNN powders from solutions modified with monoethanolamine (M), diethanolamine (D), and ethylenediaminetetraacetic acid (E) show significant ion currents for NaO and KO below 550°C [60]. Crystallization is accompanied by a large exothermic peak on the TGA-DSC plot only in modified solutions [60]. In Figure b, (a) indicates unmodified KNN solution, and (b) – (f) indicate modified KNN solutions.

EDTA. The exothermic peak at crystallization was significantly lower for the unmodified solution.

2.10 Alkali Excess Effects

Changing the alkali excess content in KNN films notably changes the grain size. Increasing alkali content typically results in increased grain size [61], stronger {100} orientation [62,23], and retention of {100} orientation to greater thicknesses, as with increasing lead excess in PZT thin films [8]. Homogeneous nucleation and growth rates are also affected by the alkali excess [62]. In the literature, typically an excess of potassium is required to react with niobium [3,20,29]; the element potassium is more volatile than sodium over crystalline KNN [58], as seen in Figure 2-12.

2.11 Film Orientation

The growth of {100} oriented KNN films by chemical solution deposition presents a series of challenges that are discussed here, along with possible solutions. {100} oriented KNN films will theoretically provide the strongest piezoelectric strain response at the MPB due to polarization rotation [4,63].

Because it is hypothesized that nucleation controls orientation, depositing thin layers should encourage strongly {100} oriented films by reducing the opportunity for nucleation within the bulk of the film or on the film surface [38]. To accomplish this, care must also be taken to remove as much organic matter from the film as possible. For example, at 21 nm/layer, CSD KNN films maintained strong {100} preferential orientation up to 15 layers [64]. Each layer was pyrolyzed for 8 minutes at 350°C and crystallized before the next layer was added. Films that

were not crystallized after every layer, but were annealed only after the final layer had weak X-ray diffraction (XRD) peaks with no preferential orientation. In another example, after pyrolysis at 550°C, heavily modified KNN deposited with a thickness of 40 nm/layer maintained a texturing factor of 91.7% {100} at 5 layers [28].

The ability to achieve {100} preferred orientation can be strongly affected by excess alkali content in the solution. However, for very thin layers (21 nm/layer) excess alkali had no effect on the (100) orientation, suggesting that heterogeneous nucleation from the substrate is the most important contributor to {100} preferred orientation in KNN thin films [36, 22]. Additionally, intermediate phases or foreign particles can affect the orientation of the perovskite phase by favoring heterogeneous nucleation [8].

2.12 Conduction Mechanisms in CSD (K,Na)NbO_3 Thin Films

Prior reports suggest that it is challenging to produce KNN thin films with low leakage currents and measurable ferroelectric properties [22,31]. As mentioned earlier, the electrical properties of KNN thin films are somewhat dependent on the niobium component (see Figure 2-14) [31], and on the extent of hydrolysis and the amount of chelating agent used in the solution. Electrical properties for niobium oxide were found to degrade with the addition of acetylacetone due to considerable amounts of residual carbon retained to high temperatures. In this case, high conductivity was attributed to the consequent regions of amorphous niobium oxides in the film [31].

Determining what causes high conductivity becomes more complicated with the addition of alkali metals in KNN. Another reported contribution to conduction is composition inhomogeneity of the alkali constituents in the film after processing [22]. Kupec et al. used conductive atomic force microscopy (c-AFM) to probe the KNN surface and found conduction

along the grain boundaries, and not through the grains for a film deposited from a 10% excess K solution (see Figure 2-15) [22]. The film with 5% excess K had smaller grains and current flowed through the grains. Further transmission electron microscope and energy dispersive x-ray spectroscopy (TEM-EDXS) analysis revealed flush grain boundaries for the 5% excess film, and pockets of amorphous niobium-rich material in pores and grain boundaries in the 10% excess K film. The niobium rich phase was not detectable in XRD patterns.

Conductivity along the grain boundaries in the film with 10% excess K was attributed to the amorphous conductive phase in the grain boundaries. Formation of the amorphous phase was attributed to the different reactivities of the constituents [65, 31].

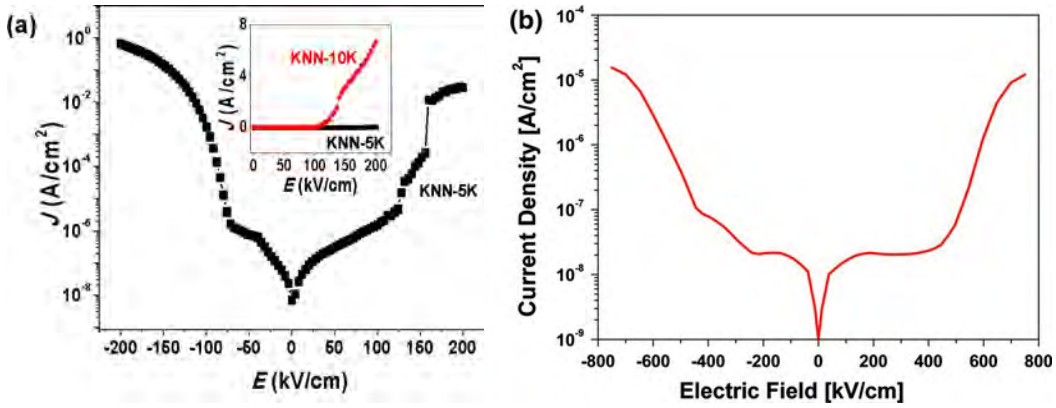

Figure **2-14**: A comparison between leakage current density profiles of thin films of KNN (a) and niobium oxide (b) deposited from unmodified solutions with solvent 2-MOE via spin coating [22,31]. The KNN solution (a) had 5 % excess potassium added to account for volatility during processing.

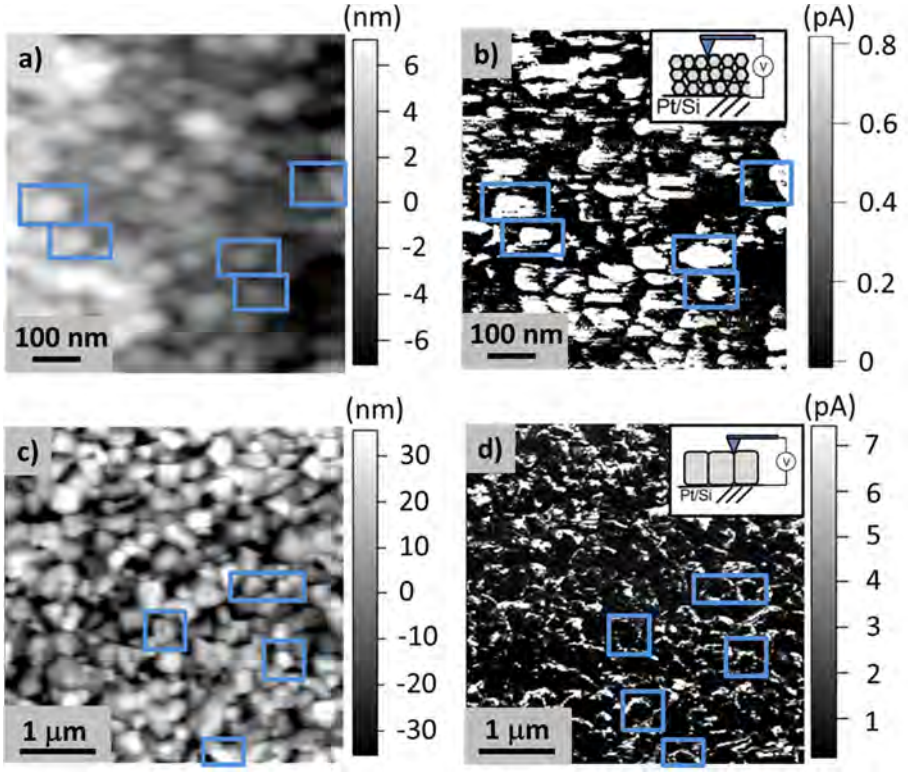

Figure **2-15**: Microstructure by AFM (left) and conductive AFM (right) images of KNN from solutions with 5% excess K (a,b) and 10% excess K (c,d) [22]. Lighter areas have higher leakage current density. Note the change in scale.

The defect chemistry of KNN influences the mode of conduction. Here is a brief summary of possible defects in KNN and what may cause them [66].

During annealing in the presence of a low pO_2, oxygen atoms in the lattice can volatize, as shown below.

$$O_O^x \leftrightarrow V_O^{\cdot\cdot} + \frac{1}{2}O_2(g) + 2e^-$$

Upon annealing in a high pO_2 atmosphere, such as under flow of oxygen, or post annealing in an oxygen-rish atmosphere, oxygen vacancies can fill to create holes.

$$V_O^{\cdot\cdot} + \frac{1}{2}O_2(g) \leftrightarrow O_O^x + 2h^{\cdot}$$

Alkali volatility is often associated with the generation of holes due to the charge balance reaction. In this case, the alkali ion reacts with atmospheric oxygen to form K_2O or Na_2O, leaving A-site vacancies and holes.

$$2Na_{Na}^x + \frac{1}{2}O_2(g) \leftrightarrow 2V_{Na}' + Na_2O(g) + 2h^{\cdot}$$

Lastly, alkali ions can react with oxygen in the lattice to volatize as K_2O or Na_2O, without generating new electronic charge carriers [66].

$$2Na_{Na}^x + O_O^x \leftrightarrow 2Na_2O(g) + 2V_{Na}' + V_O^{\cdot\cdot}$$

In semiconductors with an excess of electrons (e.g. in the case of KNN, where there are oxygen vacancies) the conduction is n-type. Where there is an excess of positive charge carriers called holes (as would be the case for excess alkali deficiency relative to oxygen vacancies in KNN) the conduction is p-type. When KNN is annealed in a low pO_2 environment, its conduction is n-type due to the presence of oxygen vacancies [67,68]. When KNN is annealed in air or a high pO_2 atmosphere, its conduction has been found to be p-type [67,68]. The alkali vacancy concentration depends on the partial pressure; low pO_2 favors alkali retention and high pO_2 favors volatility which generates hole carriers. N-type or p-type conduction governs the type of dopant which can be used to make the material more insulating. A donor dopant will donate electrons and should reduce the conductivity of a p-type semiconductor. An acceptor dopant accepts electrons and should reduce the conductivity where there is n-type conduction. Acceptor dopants such as Mn or Cu may in turn generate oxygen vacancies to compensate for the charge imbalance on the niobium site, as discussed in the next section.

An extra factor should be considered when firing materials with bound organics, such as in CSD KNN. The firing atmosphere at the onset of crystallization may be reducing in standing air, since CO and CO_2 evolution reduces the local pO_2 [17]. This can case the formation of

oxygen vacancies that accompany low pO_2 anneal atmospheres, and simultaneously suppress alkali volatilization during crystallization.

2.13 Doping Effects

Pure KNN films with good piezoelectric properties have been produced via sputtering [69,70]. However, it is difficult to produce pure KNN films via CSD that remain insulating at high electric fields [22,27]. High leakage currents at elevated fields make it difficult to pole the films for piezoelectric measurements.

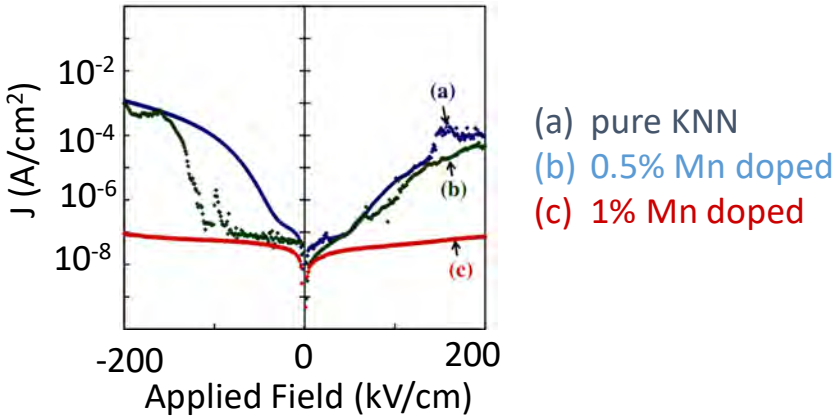

Figure **2-16**: Manganese doping significantly reduces the leakage current in KNN thin films [59].

It has been reported that doping with 1% manganese can reduce the leakage current (see Figure 2-16) [59]. Manganese occupies the Nb^{5+} site in a mixed valence state of Mn^{2+} and Mn^{3+}. Mn^{2+} should act as an acceptor dopant [71]; it may also lower the electron concentration relative to undoped films.

$$MnO \xrightarrow{NaNbO_3} V'_{Na} + Mn'''_{Nb} + O_O^{\times} + 2V_O^{\cdot\cdot}$$

It is difficult to determine the exact valence state of Mn [72]. It is possible that Mn^{2+} oxidizes to Mn^{3+} and traps a hole on the manganese site, creating another polaron conduction mechanism where positive charge carriers hop between Mn^{3+} sites [73]. In this case, Mn^{3+} reduces leakage currents when introduced at low concentrations where Mn^{3+} spacings larger than the polaron hopping distance exist, so trapped holes do not conduct (see Figure 2-17). Concentrations of Mn greater than 1% in KNN result in the appearance of a $K_2Mn_4O_8$ secondary phase [74].

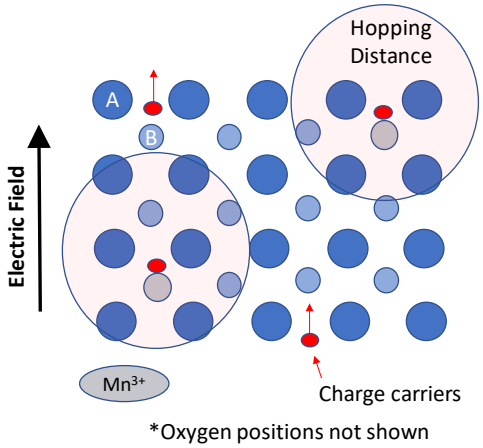

Figure **2-17**: A graphical description of the polaron hopping effect of an acceptor dopant, where holes are localized on Mn^{3+} because they cannot conduct by hopping between Mn^{3+} sites. A-site and B-site atoms are shown; oxygen atoms and vacancies are not shown.

Doping with lithium raises the Curie temperature of KNN to 500°C, and doping with Ta decreases the Curie temperature about 6°C for each mol% added [75]. Doping KNN with $CaZrO_3$ can reduce the leakage current [59].

A recent series of papers on antimony-doped KNN with strong piezoelectric properties reported easy polarization rotation [75,76,77]. Augmenting this, low domain wall energy and nanodomains within sub-micron domains maximize the extrinsic piezoelectric response, making these ceramics exceptionally responsive. However, it is important to note that Sb-doped KNN

relies on polymorphic phase boundaries between the tetragonal, orthorhombic, and rhombohedral phases near room temperature. This limits the temperature range where high performance is achieved and produces highly variable domain structures over the device lifetime. In undoped KNN the first polymorphic phase boundary above room temperature is around 200°C (see Figure 2-5), which makes it a suitable lead-free alternative for high temperature applications.

2.14 Microstructure

The microstructure of KNN films (grain size, grain structure, density/porosity) is closely related to their performance. While large grain size is sometimes preferred in lead-based piezoelectric ceramics, small grain size has been suggested to cause an increase in the extrinsic contribution to polarizability in KNN ceramics [78,15,79]. Homogeneous compositions in CSD films tend to have small grain sizes [52]. Large and columnar grains in KNN deposited via CSD are often associated with high leakage currents and conductive pathways along the grain boundaries [22].

Recent findings discovered that abnormal grain growth is associated with reduced dielectric and ferroelectric properties in bulk KNN ceramics [80]. Abnormal grain growth in potassium sodium niobate is linked to decreased ε_r, increased E_c, reduced fatigue resistance, and a decrease in latent heat at phase transitions [80]. Potassium sodium niobate, when produced by a route that is not optimized, can have a broad grain size distribution. Differences between the diffusion coefficients for sodium and potassium may be responsible for the non-uniform grain sizes [52].

2.15 Activation Energy for Nucleation and Growth

This thesis studied the activation energy for nucleation and growth of KNN thin films grown via chemical solution deposition following the Johnson-Mehl-Avrami-Kolmogorov (JMAK) model [81,82,83,84]. The experiments performed to determine the activation energies for crystallization were similar to those of Kwok and Desu on sputtered $PbZr_{0.55}Ti_{0.45}O_3$ thin films [85]. Their study used scanning electron microscope (SEM) images to calculate the activation energy by direct observation of crystalline rosette sizes. Their films were amorphous as sputtered and crystallized by annealing for various times. Three activation energies were generated: nucleation, growth, and perovskite transformation.

The perovskite transformation temperature was found to be around 550°C. Anneals were performed at 525°C, 550°C, and 575°C in a quartz tube furnace. Key assumptions were made for this study. Growth was assumed to be 3-dimensional until the diameter of the spherical nuclei equaled the thickness of the thin film (~350 nm). Afterwards, growth was assumed to be 2-dimensional in the plane of the substrate. The composition of the amorphous matrix and crystalline rosettes were similar, confirmed by SEM backscatter images.

The activation energy for growth was calculated using images from the early stages of annealing. The radii (r_{max}) of the rosettes were used to determine the rate constant, k.

$$r_{max} = kt^n$$

$$\ln(r_{max}) = \ln k + n \ln t$$

Thus, the y-intercept in a plot of $\ln(r_{max})\ vs.\ \ln t$ yields the rate constant, ln(k) (see Figure 2-18). The time exponent *n* indicates the type of crystal growth. Values for the rate constant, n, reported by Kwok and Desu were around 1, which indicates surface-mediated growth from the perimeter of the rosettes [85]. The rate constants were plotted on a ln(k) vs. 1/T plot and the slope was multiplied by the universal gas constant, R, to calculate the activation energy (E_a) for growth.

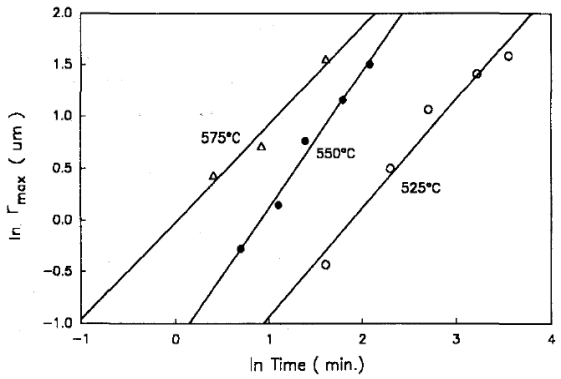

Figure **2-18**: ln(r_{max}) vs. ln(time) where the y-intercept (ln(k)) yields the rate constant and the slope (n) describes the crystal growth [85].

$$\ln k = \ln A + \left(\frac{-E_a}{R}\right)\left(\frac{1}{\mathrm{T}}\right)$$

The JMAK model describes a constant growth rate. However, since there are multiple nucleation events, only rosettes from the first nucleation event can be used to assess the growth activation energy. Growth occurs in "layers", where the first layer nucleates and grows at a constant rate, followed by the nucleation and growth of other layers along the time coordinate [85]. The rosettes from each "layer" of nucleation along the time coordinate will be the same size, within that layer, as shown in Figure 2-19.

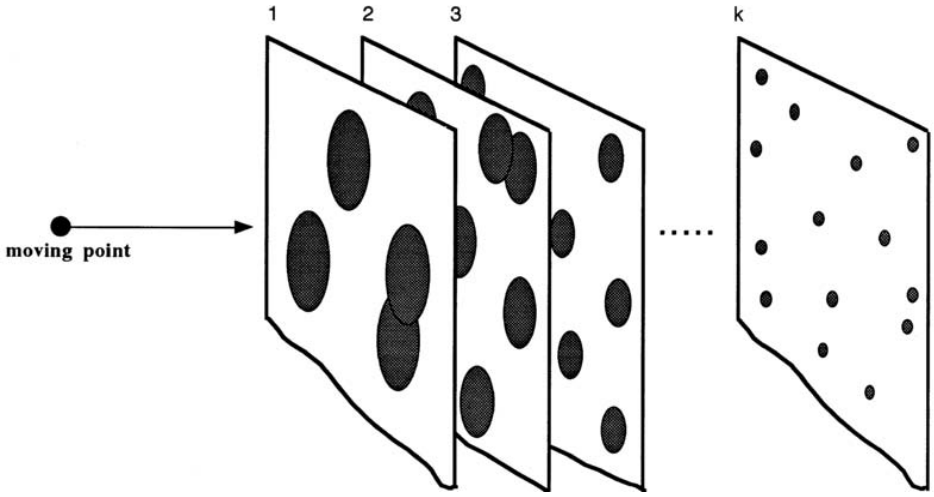

Figure **2-19**: Layered nucleation events where rosettes all of one size grow in each layer. The moving point travels along the time coordinate and through the layers that grow sudsequently during crystallization [81].

The activation energy for nucleation was calculated from the nucleation rate ($\dot{N}$). The density of nucleation sites per area was measured using SEM micrographs. There was a trend of rising nucleation rate followed by decreasing nucleation rate due to depletion of reactants in the amorphous matrix as the anneal progressed (see Figure 2-20). The average nucleation rate was calculated by the slope of nucleation density (N) per area vs. time (Δt).

$$\dot{N} = \frac{N_i - N_{i-1}}{\Delta t}$$

$$\ln \dot{N} = \ln A + \left(\frac{-E_a}{R}\right)\left(\frac{1}{\mathrm{T}}\right)$$

The perovskite transformation energy was calculated using the Avrami-Erofeev kinetic equation [84,85].

$$X_t = 1 - \exp\left(-kt^n\right)$$

$$\ln\left(\ln\frac{1}{1 - X_t}\right) = \ln k + n \ln t$$

where X_t is the volume fraction converted to the desired crystalline phase. In Desu's work it is the

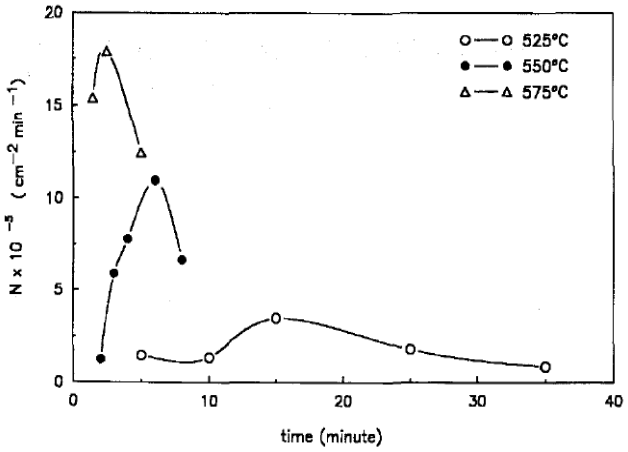

Figure **2-20**: Rising nucleation rate followed by falling nucleation rate trend in lead zirconate titanate films [85].

perovskite phase, and the y-intercept is the natural log of the rate constant, ln(k), at various temperatures. The rate constants were plotted on a ln(k) vs. 1/T plot (see Figure 2-21) and the slope was multiplied by the universal gas constant to calculate the activation energy. The n values were between 2 and 3 indicating 2-dimensional growth of crystallites in thin film PZT [17]. The perovskite transformation, nucleation, and growth activation energies follow an Arrhenius dependence between the rate constant and inverse temperature. The perovskite transformation energy is a sum of the activation energies for nucleation and growth [81].

In Kwok and Desu's work [85], the transformation, nucleation, and growth activation energies were determined to be 494, 441, and 112 kJ/mol, respectively. The activation energies did not sum to the total transformation, likely due to finite error in the determined parameters. Error bounds on values were not specified in their work. Significantly larger activation barrier for

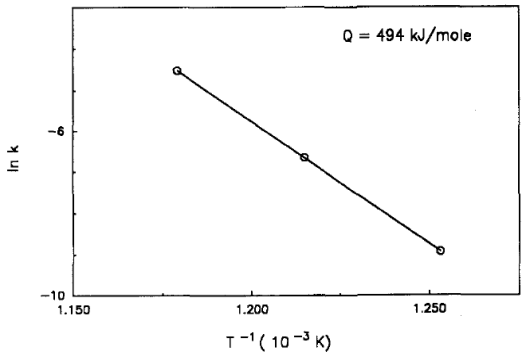

Figure **2-21**: The perovskite transformation energy was calculated from the slope of ln(k) vs. 1/T. From reference [85].

nucleation compared to growth indicates that perovskite transformation in PZT is nucleation controlled. PZT can be oriented by creating nucleation sites with a seed layer, effectively reducing the energy input for nucleation and reducing the crystallization temperature [41,86]. The activation energies for other compositions of PZT are shown below.

Table **2-1**: A comparison between activation energies for different compositions of PZT synthesized and characterized by different methods [87,88,89].

Material	Synthesis Method	Measurement Type	Activation Energy (transformation, nucleation, growth) (kJ/mol)
PZT 53/47 [85]	Sputtering, thin film	Scanning electron microscopy	494, 441, 112
PZT 60/40 [87]	CSD, spin-coat	Optical	n/a, 286, 83 ± 6
PZT 80/20 [87]	CSD, spin-coat	Optical	n/a, 296, 76 ± 5
PMN-PT (43% PT) [88]	Sol-gel, w/o PVP mod.	X-ray diffraction	305, n/a, n/a
PMN-PT (43% PT) [88]	Sol-gel, w/ PVP mod.	X-ray diffraction	168, n/a, n/a
PZT 40/60 [89]	Sol-gel, 100°C/s ramp	X-ray diffraction	610, n/a, n/a

Chapter 3

Experimental Procedure

3.1 Solution Preparation

In this study, potassium sodium niobate films were prepared from different types of solutions, via chemical solution deposition (CSD). The films were characterized to confirm their crystalline phase by X-ray diffraction, and their morphology, grain size, and compositional uniformity by field emission scanning electron microscopy and energy dispersive spectroscopy. The films were characterized electrically for dielectric constant and loss tangent, polarization hysteresis, and piezoelectric coefficients.

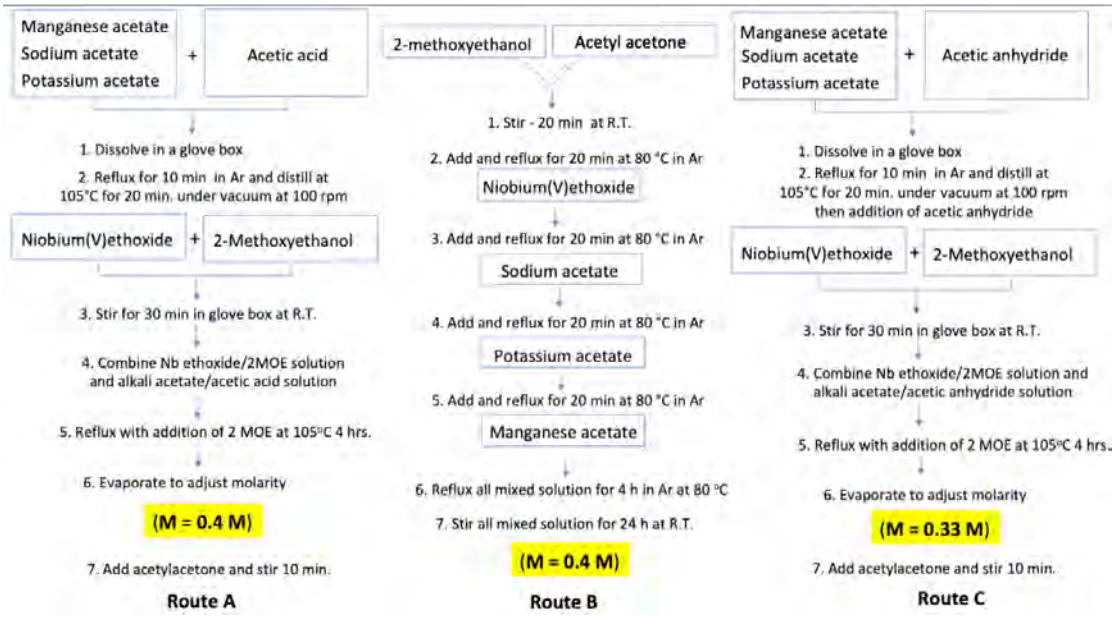

Figure **3-1**: Three different solution methods. Solution B was made in one flask [87].

Multiple methods were used to produce KNN thin films from solutions of different types; these will be referred to hereafter as solutions A, B, and C (see Figure 3-1). The solution

preparation method does, in fact, have a large effect on film growth [90]. Because the optimal amount of excess volatile species such as sodium and potassium oxides was originally unknown, solutions were prepared with different amounts of excess sodium and potassium to account for volatility during heat treatment. Most films in this thesis were prepared with 5 mol% excess Na and 10 mol% excess K.

Solutions were prepared with 2-methoxyethanol solvent by weighing anhydrous sodium acetate (CH_3COONa) from Sigma-Aldrich 99% purity, anhydrous potassium acetate (CH_3COOK) from Sigma-Aldrich 99% purity, and manganese acetate tetrahydrate $(CH_3COO)_2Mn{\bullet}4H_2O$ from Sigma-Aldrich 99.95% purity, in plastic weigh boats and adding them to acetic anhydride in the solution C method [91,92,93]. Specific details for the other methods are referenced in Figure 3-1. In a separate flask, niobium ethoxide 99.95% purity $(CH_3CH_2O)_5Nb$ from either Sigma-Aldrich or STREM Chemicals was added to 2-methoxyethanol and weighed to achieve a final concentration of 0.4 M [30]. It is important to note that niobium content by weight can vary slightly for different commercial niobium ethoxide precursors, which is highly undesirable for this application. A switch was made to STREM Chemicals for niobium supply because they report wt % Nb for the received batch. 10 mol% excess potassium acetate and 5 mol% excess sodium acetate were added to the precursor solution to account for volatility [94,61,22]. The detailed process for each step is outlined in Figure 3-1.

The acetate precursor complex was mixed in a 250 mL round bottom flask attached to a LABCONCO rotary evaporator. A silicone oil bath heated to 106°C was prepared to heat the flask upon mixing. After mixing the solutions separately for 30 minutes, the acetate solution complex was vacuum-stripped to powder to remove water. In the “solution A” method, 2-methoxyethanol was added to the stripped powder [92]. In the “solution C” method, acetic anhydride was added to the dried powder. Then the niobium complex with 2-methoxyethanol was

Figure **3-2**: Solution C is wrapped with Parafilm® and prepared for storage.

added to the flask with the dried powder. The powders dissolved completely immediately upon the addition of 2-methoxyethanol and heat. The solutions were refluxed in a rotary evaporator under 2 SCFH (standard cubic feet per hour) flow of Argon. Solutions A and C were refluxed at 106°C for 4 hours. Solution B was refluxed for 4 hours at 80°C, then stirred for 24 hours at room temperature and stored [95,36]. After refluxing solutions A and C, 3 mL of acetylacetone was added to stabilize the solution prior to storage. This is approximately 2 molar equivalents to niobium, or one molar equivalent to metal cations in the solution. The solutions were prepared to 40 mL at 0.4 M, and stored in glass bottles wrapped in Parafilm® for an airtight seal, as shown in Figure 3-2. Solutions were stored overnight at room temperature in a dry box, and transferred to a refrigerator to be stored for at least one week prior to deposition, as described in the literature [96]. Solution colors ranged from light to dark brown and showed no sign of precipitation for months after preparation. Their color was mostly dependent on the powder drying step, where longer drying steps resulted in darker colored powder.

The solution A method was similar to that of Kupec et al. and Ahn et al. [61,29]. Solutions of lower molarity were prepared for special purposes, such as improved {100} preferential orientation [92].

3.2 Solution Deposition and Heat Treatment

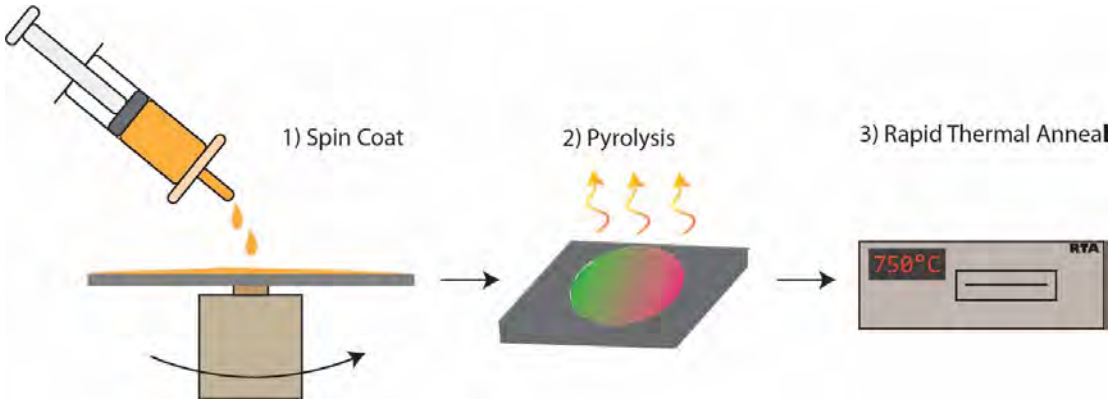

Figure **3-3**: A diagram of the chemical solution deposition process used in this thesis.

These solutions were deposited on platinized silicon wafers from Nova Electronic Materials following a spin coating and heat treatment process, depicted in Figure 3-3. The substrates were from top to bottom: 150 nm platinum, 20 nm titanium, 1 μm thermal oxide SiO_2, and 0.5 mm p-type silicon. 10 mL plastic BD syringes and 0.1 μm filters with a PTFE (polytetrafluoroethylene) membrane and polypropylene housing were used to dispense the solution onto the wafer for spin coating. The substrate was coated dynamically at a speed of 600 RPM and ramped to 3,000 RPM for 30 seconds immediately after the solution dispense step to form an even layer. This process was followed by heat treatment on hotplates with steel surfaces, as shown in Figure 3. The deposited film was dried at 200°C to remove the solvent. The heat treatment procedure for continued removal of organics varied by solution preparation method, and their corresponding thermogravimetric analysis profiles (TGA), as described later. Solutions A and B were pyrolyzed at 300°C for 3 minutes. Solution C was pyrolyzed at 300°C for 3 minutes followed by a second pyrolysis step at 430°C for 3 minutes [95]. The same two-step pyrolysis at 300°C and 430°C was also performed on solution A to compare with solution C.

After pyrolysis to remove organics, the films were rapid thermal annealed in an RTP-600S, manufactured by Modular Process Technology Corp. Samples were ramped at a rate of 10°C/s to temperatures ranging from 450°C to 750°C for 5 minutes to crystallize KNN. Samples made from the solution C method were cooled from the annealing temperature at a rate of 5°C/s to avoid cracking, which was likely due to higher density with less routes for stress relief (e.g. pores). The annealing atmosphere varied between standing air and 2 SLPM flow of oxygen or nitrogen.

Solution deposition (Figure 3-3) via sol-gel can be lengthy, so it is important to be aware of changing conditions as the process progresses. Precautions were made to control solution viscosity within the syringe by wrapping the syringes in aluminum foil and keeping them away from heat sources, such as hotplates, and changing syringes every 2.5 hours (set-up shown in Figure 3-4). Films were stored on hotplates at elevated temperatures during breaks to keep the surfaces from adsorbing water.

Figure **3-4**: Films were deposited in the spin system in a PSU Nanofabrication facility with a controlled atmosphere and at 21% relative humidity.

3.3 Other Solution Considerations

Solution preparation with acetic acid and acetic anhydride must be performed carefully. Provided an appropriate surface, acetic acid and 2-methoxyethanol will esterify above 120°C [21]. It is critical to be as clean as possible and to lower the silicone oil bath to 110°C before refluxing so that no ring of solid precipitates forms due to a potential rapid boil-off of 2-MOE at the onset of refluxing, of which the residue can act as a substrate for further esterification or precipitation [21]. The purpose of adding acetic anhydride to the final solution is to delay hydrolysis and to enhance the ability of the solution to form a columnar film [96], as it reacts readily with water to form acetic acid. Films produced by the solution C method which used acetic anhydride produced the most optically reflective films.

Different solution routes and heat treatments were used in attempts to deposit a KNN film with large and columnar grains, high breakdown field, high piezoelectric strain coefficient $e_{31,f}$, and good fatigue characteristics. From here on, the nomenclature for KNN films and powders made from solutions A, B, and C will be KNN-A, KNN-B, and KNN-C, respectively.

3.4 Electrode Deposition

Circular platinum electrodes with diameters ranging from 0.2 mm to 1 mm were deposited for electrical characterization. Platinum electrodes were patterned on samples using a photolithography technique. LOR 5A and SPR 3012 photoresists were spun on and soft baked, followed by patterning with a mask under ultraviolet light, and developing the pattern with MF® CD-26. The patterned surfaces were cleaned in a He/O_2 plasma before electrode deposition. Platinum top electrodes of 100 nm thickness were deposited via DC sputtering in a Kurt J. Lesker CMS-18 sputtering system (conditions in Table 3-1), using argon as the process gas. Following

deposition, photoresist was removed with acetone and MF® CD-26 developer. Then the sample was annealed at 300°C under nitrogen flow for 10 minutes.

Table **3-1**: Deposition conditions for top electrode sputtering from a metallic Pt target.

Process Parameter	Deposition Conditions
Process Gas	Argon
Pressure	2 mTorr
Temperature	17°C
Power	200 W
Time	417 s

3.5 Powder Preparation (for TGA)

Powders were prepared from solution for thermogravimetric analysis, evolved gas analysis, and differential scanning calorimetry to determine the optimal heat treatment recipe for each solution type. The solutions were dried in a glass container on a hotplate set to 150°C for 85 minutes. The dried powders were ground by hand with a metal spatula, then capped and sealed with Parafilm®.

3.6 X-ray Diffraction

X-ray diffraction (XRD) patterns of thin films were obtained to confirm the crystalline phase in KNN. XRD was performed using a Malvern Panalytical XPert Pro Multi Purpose Diffractometer with a θ-2θ goniometer. Samples were placed on an amorphous plastic holder. Cu radiation, predominantly at a wavelength of 1.54059 Å was produced from the X-ray tube.

Counts were produced by a PIXcel 1D silicon strip detector. A programmable divergence slit, 10 mm beam mask, 0.04 rad Soller slit, and a Ni K_β filter were placed in the beam path. A ½° anti-scatter slit was placed on the incident beam and a programmable anti-scatter slit on the reflected beam.

Scans captured the {100}, {110}, and {200} reflections from perovskite phase KNN, and the most prominent secondary phase peaks from the potassium tungsten bronze structure of $K_4Nb_6O_{17}$ [97].

3.7 Thermal Analysis and Mass Spectroscopy (TGA-MS/TGA-EGA)

Thermogravimetric analysis was performed with a Discovery Series TGA Q5500 with an attached Discovery MS (mass spectrometer), by TA Instruments. Approximately 12 milligrams of powder prepared as described previously was placed in a platinum crucible for thermogravimetric analysis. A heating rate of 5 to 20°C/min was used to heat dried powders from room temperature to 800°C. Air flow was set to 25 cc/min. Data generated simultaneously were % weight loss vs. temperature and ion currents for atomic masses from 1 AMU to 100 AMU. The Discovery MS is a quadrupole mass spectrometer which performs evolved gas analysis (EGA).

3.8 Thermal Analysis and Differential Scanning Calorimetry (TGA-DSC)

Simultaneous thermogravimetric analysis and differential scanning calorimetry was performed with a Q600 SDT (TA Instruments, New Castle, DE) with a calorimetric accuracy of ±2%. Approximately 10 milligrams of powder prepared as described previously was placed in an alumina crucible for testing. A heating rate of 5°C/min was used to heat dried powders from room temperature to 800°C. Air flow was set to 100 cc/min. Data generated simultaneously were %

weight loss and heat flow vs. temperature. Specific energies of the decomposition steps are reported (see Figures A-2, A-3, A-4, A-5).

3.9 Field Emission Scanning Electron Microscopy (FESEM)

Field emission scanning electron microscopy (FESEM) (Leo 1530, Merlin, G500) was used to obtain high resolution images of the KNN microstructure. Electrons accelerated at 5 kV were incident on the samples. In the activation energy study, the FESEM was used to determine the size of the nuclei. FESEM backscatter images were used to observe compositional differences on the film surface.

3.10 Energy Dispersive Spectroscopy (EDS)

A FESEM Merlin with an attached energy dispersive spectroscopy (EDS) detector was used to observe spatial composition changes at high resolution for the nucleation study. An acceleration voltage of 10 kV and beam currents of approximately 2 to 10 nA were incident of the samples. A Thermo Scientific Q250 SEM with an EDS attachment was used to generate lower resolution composition maps of the KNN thin films. A 10 kV acceleration voltage with a beam current of 93 nA were incident on the samples.

3.11 Fourier Transform Infrared Spectroscopy (FTIR)

Fourier transform infrared spectroscopy (FTIR) was used in combination with TGA-EGA and TGA-DTA to identify unknown organic compounds in partially crystalline and fully crystalline KNN thin films. A Vertex 70 spectrometer (Bruker Optics, MA) with a deuterated

lanthanum α-Alanine doped triglycine sulphate (DLaTGS) detector was used to collect IR spectra. Polarized spectra was collected in specular reflection mode at an incident angle of 75° on a Veemax II accessory (Harrick Scientific, NJ). Each spectrum was the average of 172 scans with a 6 cm^{-1} resolution. Absorbance spectra were referenced to clean gold.

3.12 Nucleation and Growth Kinetics in Thin Films

During early crystallization of KNN films, it was found that individual nuclei grow as circular regions called rosettes. FESEM was used to determine the size of KNN rosettes, the volume fraction crystallized, and the number of rosettes on partially crystallized samples prepared to determine the activation energies for nucleation, growth, and phase transformation for KNN-C. The nucleation study is similar to that performed by Kwok and Desu on lead zirconate titanate thin films [85]. The size of the rosettes was quantified using image J software by measuring the

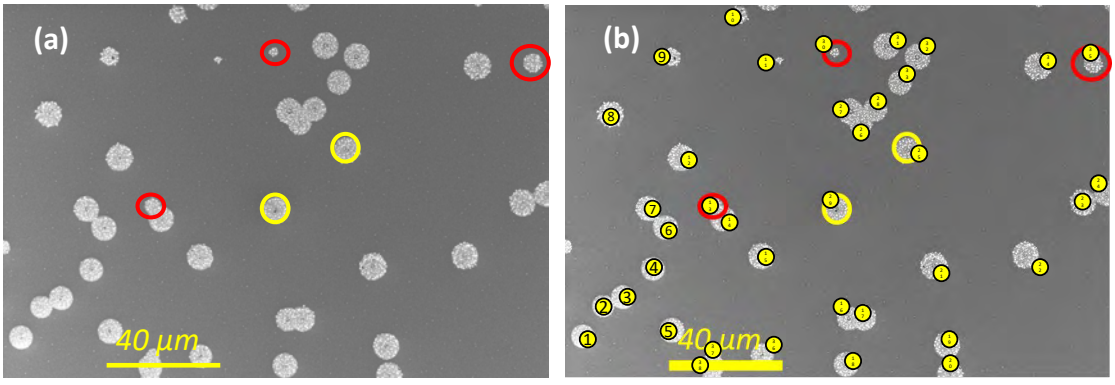

Figure **3-5**: Rosette radii were measured (a) by measuring the circumference (yellow outline) of 10 to 30 individual rosettes from the first nucleation event, over multiple areas of each film. Hollow yellow circles sample rosettes from the first nucleation event, and red circles sample those from later nucleation events. Rosettes were counted manually (b).

circumference of 10 to 30 rosettes on each sample. All rosettes are assumed to be circular. In cases where two rosettes impinged on each other, two circles were approximated, using image J software, as shown in Figure 3-5a. The average rosette sizes from the first nucleation event were used for this study. The surface density of the nuclei was calculated by averaging the number of nuclei per area over images of each sample's surface. The image J "Multi-point" counter was used to count the number of rosettes on each image, as shown in Figure 3-5b.

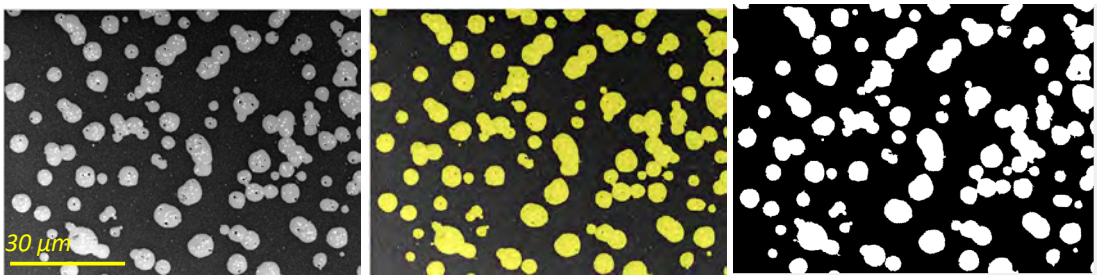

Figure **3-6**: Microscopy of a partially crystallized KNN film. The dark area is the amorphous matrix. The brighter areas are the crystalline rosettes. The raw FESEM image (left) was segmented using either an adaptive image segmentation or a graph-cut method (middle) to generate a binary image segregated by contrast (right).

Due to contrast gradients across the FESEM images, simple image segmentation software was not suitable for measuring the volume fraction crystallized. This parameter was measured using the MATLAB® Image Segmenter application (see Figure 3-6). The adaptive image segmentation threshold technique factors the contrast gradient across a film, an artifact on FESEM micgrgraphs, and discerns objects through local background contrast, as seen in Figure 3-6. Volume fractions were averaged over 10 surface images of each sample. For images where the adaptive image threshold did not distinguish rosettes from the background effectively, images were segmented via a graph-cutting technique where "bright" and "dark" areas were discerned

manually. Both image segmentation techniques accurately measured rosette area (see Appendix for error propagation).

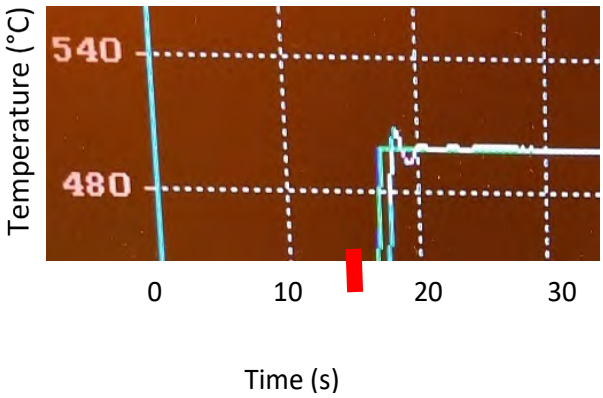

Figure **3-7**: Ramp overshoot in the rapid thermal annealer. The blue line is the programed temperature, and the white line is the actual temperature. The red tick marks the beginning of the ramp step after a 15 second hold at 300°C.

The bright portion of the segmented images was assigned to crystalline portions of the film. Binary images were generated; the bright pixels were assigned a value of 1 and the dark pixels, representing the background, were assigned a value of 0, as seen in Figure 3-4. The average of the sums of 10 binary images accounted for each data point representing the volume % crystallized (see calculations in the Appendix).

Samples for this nucleation study were deposited using the same procedures as outlined earlier. Prior to deposition, cut substrates were cleaned in two sonicating baths of isopropyl alcohol. Each sample was pyrolyzed following the 2-step pyrolysis for KNN-C, and annealed immediately after the second pyrolysis step. Single-layer films were annealed at 500°C, 525°C, 550°C, and 575°C. Ramp rates between 90°C/s and 93°C/s were used to minimize the formation of secondary phases. Overshoot by up to 15°C resulted from the high ramp rate; the temperature approached steady state approximately 3 seconds into the hold step at the target temperature, as

shown in Figure 3-7. Immediately at the end of the hold step, without allowing the carrier wafer to cool, the sample was removed from the rapid thermal annealer and placed on a stainless-steel workbench to quench to room temperature. All samples were deposited within 1 hour and 45 minutes to minimize solution aging within the syringe as much as possible. Samples were stored overnight in the deposition bay at 21% relative humidity for FESEM micrographs the following day.

3.13 Dielectric Constant and Loss Tangent

Electrical contact was made to electrodes with tungsten probe tips using micromanipulators. The low-field dielectric constant (ε_r) and dielectric loss (tan(δ)) were measured using a precision LCR meter 4284A (Hewlett-Packard, Palo Alto, CA). Frequency sweeps were performed from 100 Hz to 1 MHz with an amplitude of 30 mV to measure the capacitance and loss tangent, tan(δ).

$$\varepsilon_r = \frac{Cd}{\varepsilon_o A}$$

The dielectric constant was calculated from the measured capacitance, C, where d is the film thickness, A is the top electrode area, and ε_o is the permittivity of free space. Throughout this thesis, the dielectric constant and tan(δ) are reported from measurements at 1 kHz unless otherwise specified.

3.14 P-E Hysteresis Loops

Polarization (P)-electric field (E) hysteresis loops were measured by a Precision Multiferroic tester (Radiant Technologies, Albuquerque, NM). The testing frequency was 100 Hz.

The maximum electric field was increased in increments of 50 kV/cm until breakdown to obtain a series of nested hysteresis loops.

3.15 Current Density (J vs. E) Plots

Current density (J) vs. electric field (E) plots were gathered to test the dielectric strength of the films. Measurements were performed by a pA meter 4140B (Hewlett-Packard, Palo Alto, CA). Current measurements were taken in 0.5 volt steps, followed by a 50 second interval allowing the transient response to diminish, before measuring the leakage current. High temperature J vs. E tests were performed on a hotplate using the same setup.

3.16 DC Hot Poling

DC poling was performed prior to measuring the piezoelectric $-e_{31,f}$ coefficient. Electrodes were poled using a DC Voltage source 4140B (Hewlett-Packard, Palo Alto, Ca). Poling was performed on a hot plate at temperatures ranging from room temperature to 140°C, and with applied fields from 50 kV/cm to 400 kV/cm. The applied field was maintained until the samples cooled down to approximately 50°C.

3.17 Piezoelectric Strain Coefficient, $e_{31,f}$, by the Wafer Flexure Method

The transverse piezoelectric strain coefficient $e_{31,f}$ was measured using the wafer flexure technique [98,99,100]; the measurement set-up is shown in Figure 3-8. This method determines $e_{31,f}$ via the direct piezoelectric response:

$$e_{31,f} = \frac{Q}{A(x_1 + x_2)}$$

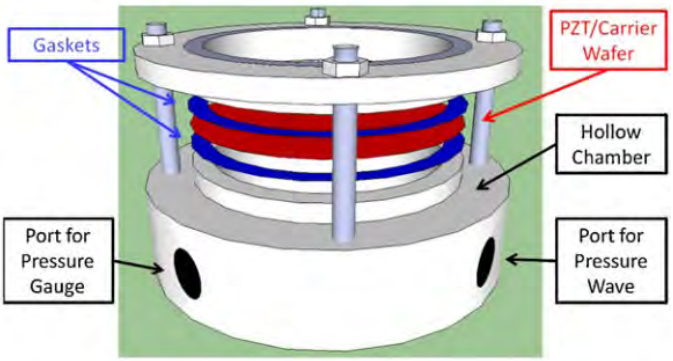

Figure **3-8**: The wafer flexure method to measure the piezoelectric coefficient. The port for the pressure wave was attached to a 10 in. speaker. Figure reproduced from [98].

where Q is the induced surface charge, A is the top electrode area, and x_1 and x_2 are the orthogonal components of strain in the plane of the film surface. This technique flexes the films by using the oscillation of a 10-inch speaker to generate pressure waves in an enclosed cavity. The changes in pressure flexed the wafer and generated strain in the film which in turn generated a surface charge through the direct piezoelectric effect. The rms current from the electrodes was measured with a SR830 Lock-In Amplifier (Stanford Research Systems, Sunnyvale, CA). The charge is generated from the rms current by the following equation:

$$Q = \frac{i_{rms}}{2\pi f}$$

Approximately 1cm x 1cm chips and biaxial strain gauges were attached to the center of the coated carrier wafers [99,100] with Loctite® superglue specially formulated for bending applications. Output from the strain gauge and top electrode were measured simultaneously on lock-in amplifiers. Once the charge response stabilized for both the top electrode and the strain gauge, the average of the last 10 measurements was recorded to calculate the transverse piezoelectric coefficient, $e_{31,f}$. The error for this measurement is within ± 10% [100].

Chapter 4

Comparative CSD Processing Routes for Mn-doped KNN Thin Films

4.1 Introduction

This chapter summarizes the data obtained from three solution methods used to synthesize potassium sodium niobate thin films – solutions A, B and C, hereafter referred to as KNN-A, KNN-B, and KNN-C, respectively. In each solution, characteristics of the films were studied and recorded: crystal structure was assessed using X-ray Diffraction (XRD), microstructure was studied using field emission scanning electron microscope (FESEM) images, and composition segregation was discerned with energy dispersive spectroscopy maps (EDS). The dielectric properties, leakage currents, polarization hysteresis loops, and transverse piezoelectric strain coefficient $e_{31,f}$ were measured. The purpose of this investigation is to determine an appropriate solution and processing route to produce KNN thin films with desirable electrical properties.

**Part of this chapter is reproduced from Kovacova, V., Yang, J. I., Jacques, L., Ko, S. W., Zhu, W., & Trolier-McKinstry, S. (2020). Comparative solution synthesis of Mn doped $(Na,K)NbO_3$ thin films. Chemistry–A European Journal. [91]*

4.2 Thermal Processing Studies

Thermogravimetric analysis (TGA) was performed on KNN-A, B, and C powders (see Figure 4-1). TGA results were used to determine appropriate temperatures for pyrolysis and crystallization. All solutions have two major mass drops centered at 280 ± 20°C and 560 ± 20°C [91]. A pyrolysis temperature of 300°C was chosen for all samples. For KNN-C, a second pyrolysis step was added at the maximum achievable hotplate temperature of 430°C for 3 min in an attempt to eliminate residual carbon and improve film density.

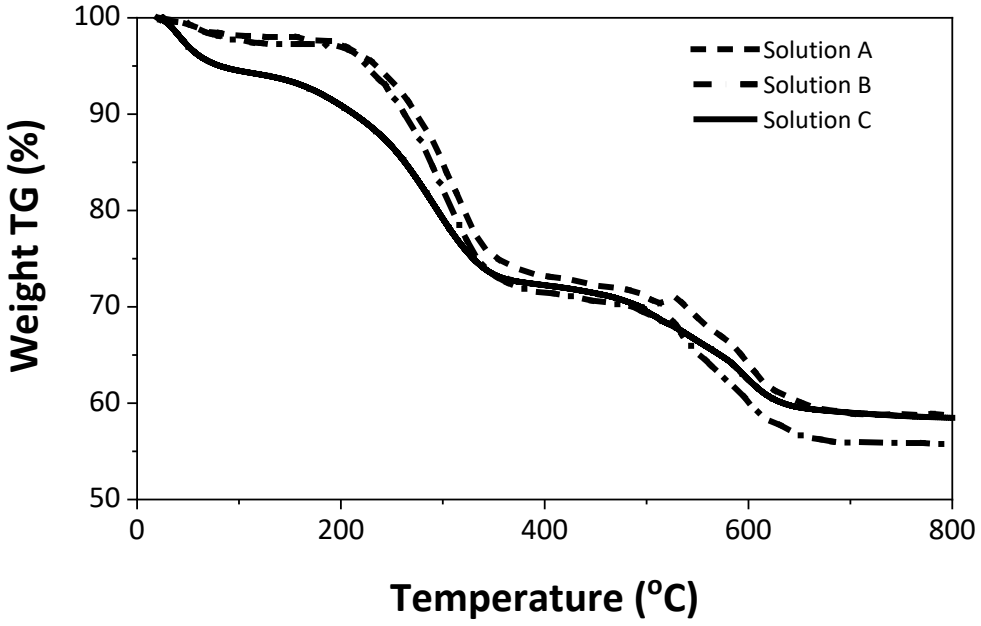

Figure **4-1**: Thermogravimetric analysis curve for KNN-A, B, and C powders. [91].

The TG profiles for all solution methods had two major mass losses centered around 300°C and 550°C. The higher temperature mass drop on TGA was likely due to retained chelating ligands from acetylacetone, or esterification reactions between 2-MOE and acetic acid during the powder drying step [32,21]. The mass loss between 300 and 500°C was attributed to the loss of

volatile alkali components and the decomposition of residual carbon [53]. The mass drop above 500°C is believed to be due to the decomposition of residual carbon and potentially oxalate or carbonate species, as these are the intermediate and final carboxylate species in the decomposition of acetates, respectively [53,101,102]. For all powders, simultaneous differential scanning calorimetry (TGA-DSC) measurements revealed multiple exothermic events above 500°C, attributed to decomposition of residual carbon species and consequent perovskite crystallization. It is believed that the mass-drop followed by mass gain at the onset of crystallization near 500°C is due to the adsorption of carbon monoxide by the crystalline metal oxide phase [101]. The adsorption of carbon monoxide is reported to reduce the decomposition rate of residual carboxylate phases [103].

TGA-MS was performed on powders from solutions A, B, and C. The most intense detections near 300°C are carbon monoxide, methane, water, and carbon dioxide. Neither Na_2O nor K_2O were detected; a trace amount of possible KO (55 AMU) was detected. The mass loss at AMU 39, which corresponds to either K^+ and/or NaO^-, is labeled in Figure 4-2, 3 as NaO^-/K^+. No Na^+ was detected at 23 AMU. Loss of Na from the powder is detected in the temperature range from 300 – 450°C, as will be discussed further below. This agrees with the literature that any significant loss of alkali precursors should occur before crystallization (c.f. Figure 2-12,13) [60]. Masses corresponding to NaO^- and KO^- were not detected above 500°C. Above 550°C there is a large release of heat, likely due to the decomposition of residual carbon species and formation of the perovskite phase [58]. The issue of detecting volatile NaO^-/KO^- remains unresolved.

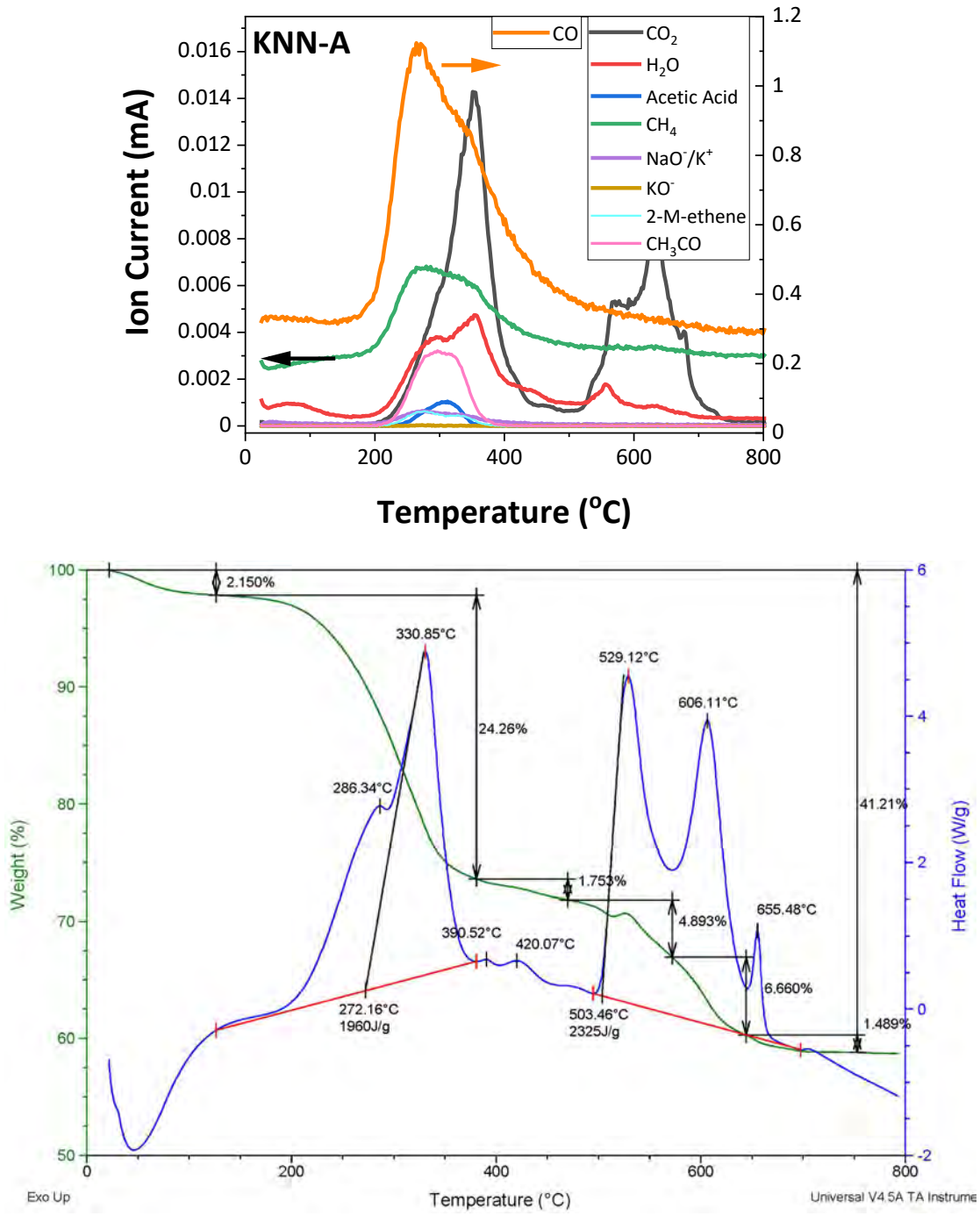

Figure **4-2**: MS profiles from EGA for KNN-A powder heated from room temperature to 800°C at a rate of 20°C/min (top). TGA-DSC profile of KNN-A powder heated at a rate of 5°C/min (bottom).

Acetic acid with a molar mass of 60 AMU was detected at 300°C, simultaneously with ethanone (CH_2CO) which is a decomposition product of acetic acid. It is especially interesting that acetic acid is found in dried powders since a vacuum distillation step was performed to remove acetic acid for solution A. Recall that the powders were dried at 150°C to remove solvent, so free 2-methoxyethanol, acetic acid, and acetylacetone should have evaporated prior to TGA experiments. The boiling point of acetic acid is 118°C, therefore, the detection of acetic acid in the MS spectra suggests that acetate groups were bonded to alkali metals; these groups then presumably volatized during the TGA experiment. To confirm this, FTIR was performed on KNN films dried at 250°C for 3 minutes, and acetates were detected (Figure 5-8). Energy dispersive spectroscopy was used to confirm the presence of sodium acetate in dried films (Figure 5-3).

The most common intermediate decomposition product of solvent 2-methoxyethanol is 2-methoxyethene, due to the fragmentation of water from 2-MOE [104]. Either 2-methoxyethene or acetone, a possible decomposition product of acetylacetone was detected at 240°C; both have a mass of 58 AMU [105]. The chelating modifier acetylacetone decomposes to CH_3CO or fragments to CH_2CO with molar masses of 43 and 42 AMU, respectively [105]. Both were detected simultaneously around 300°C (Figure 4-2,3).

CO was detected at highest concentration near 240°C from the powders, before CO_2 was detected. CO is a strong reducing agent, and thermolysis may cause reduced phases to form and segregate due to locally high diffusion rates [17]. However, in thin film processing the extent of thermolysis on a hotplate under a fume hood with flowing air may be very limited.

The second set of peaks above 500°C involve exothermic decomposition reactions that directly form CO_2 and water. Because the decomposition of carbonate is endothermic, the reaction is attributed in part to the decomposition of residual oxalates from the alkali precursors [17,101,102]. Trace amounts of compounds with atomic masses 46, 45 (fragment) and 12 AMU,

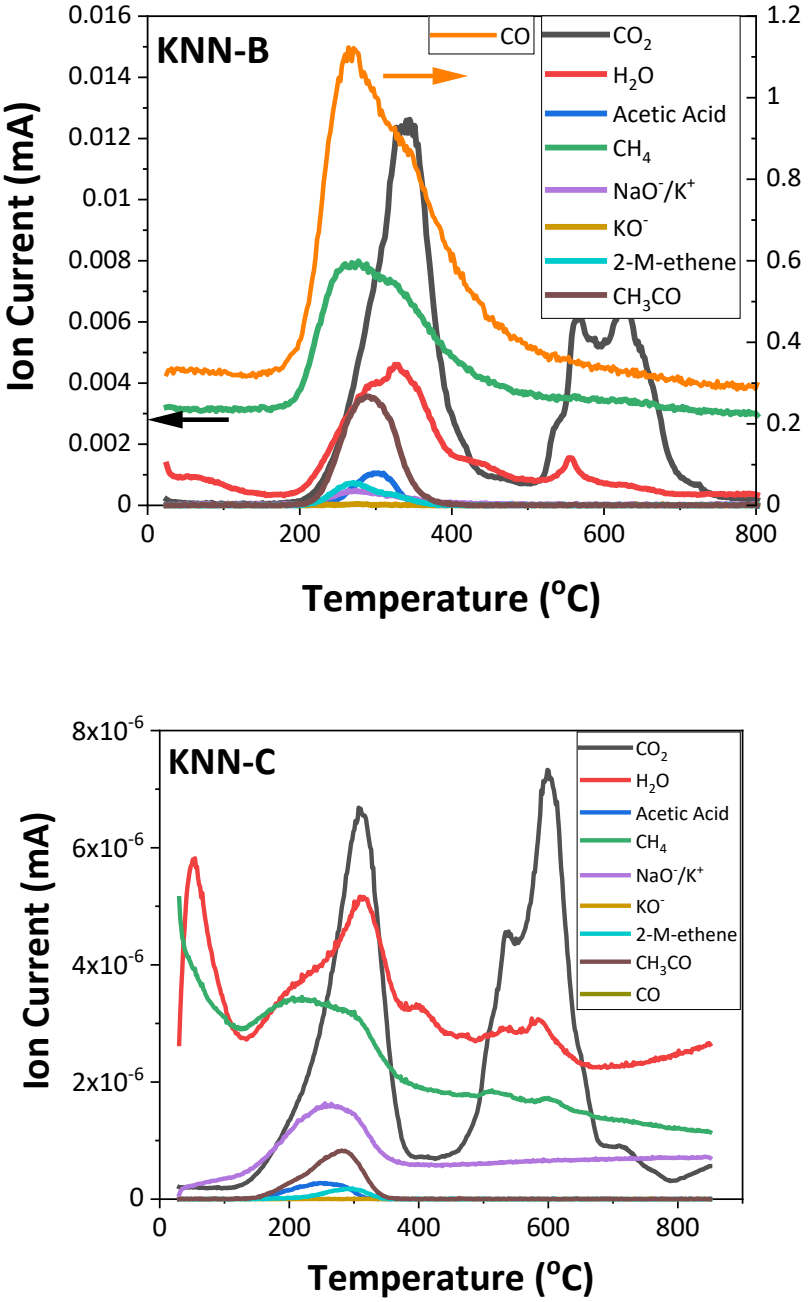

Figure **4-3**: MS profiles from EGA for KNN-B (top) and KNN-C (bottom) powders. The MS on KNN-C was performed to a maximum temperature of 850°C prior to a cleaning of the system, so reported ion currents are lower than those for solutions A and B, and this data is qualitative.

a

carbon radical, were detected as decomposition products above 500°C. Atomic masses 46 and 45 may identify formic acid and its fragment. In addition to the oxalate species, carbon retained to unusually high temperatures has been reported for both niobium [31] and sodium [106] when they are reacted with acetylacetone. Figure 4-2 shows three exothermic peaks centered at 530°C, 600°C, and 650°C on the DSC. Wang et al. show that the crystallization of KNN is not strongly exothermic when it is not coupled with a significant mass loss (c.f. Figure 2-13) [60]. Assuming this is correct, it is speculated that the first peak corresponds to the decomposition of residual carbon bound to sodium, and sodium oxalates [101]; the second peak corresponds to the decomposition of residual carbon bound to potassium, and potassium oxalates [102]. The third and highest temperature peak is not yet assigned. Further evidence that the three peaks are predominantly associated with organics decomposition is provided later.

Neither of the peaks reported in the TGA-DSC is solely attributed to crystallization of KNN, which is exothermic, because that peak is believed to be buried underneath those associated with organics decompositions. Polymer-modified KNN solutions show a similar behavior when compared to unmodified solutions (c.f. Figure 2-13), where unmodified solutions release significantly less heat for crystallization compared to polymer modified solutions [20,60,94]. The exothermic combustion reactions in this case are reported to lower the crystallization temperature according to the exothermic decomposition of the polymers. The weight loss correlates with the exothermic activity, showing that a majority of the exothermic activity in modified films is due to the decomposition of organics, and not the crystallization of KNN. In PVP modified KNN solutions, losses of NaO/Na_2O and KO/K_2O were reported simultaneously at the polymer combustion temperature [94].

In this work is reported similar phenomenon with regard to exothermic activity where the average specific energy of reactions above 500°C measured by TGA-DSC linearly correlates with the experienced weight loss. In Figure 4-4 is presented a plot of the average specific energy of

reactions vs. mass loss above 500°C. It should be noted the y-axis is the specific energy in units of Joules per gram of material lost, and not heat. Therefore, a change in the specific energy suggests a change in the (completeness of the) reactions taking place. The relationship of heat release versus mass loss for a simple organic compound is expected to be linear. However that is not the observation here; rather the specific heat versus mass loss is linear. This indicates the ability to remove residual carbon from the film above 500°C (which all the mass loss in that temperature regime is attributed to) depends on either the completeness of the reaction or promotion of decomposition by an induced exothermic activity. Otherwise, residual carbonates

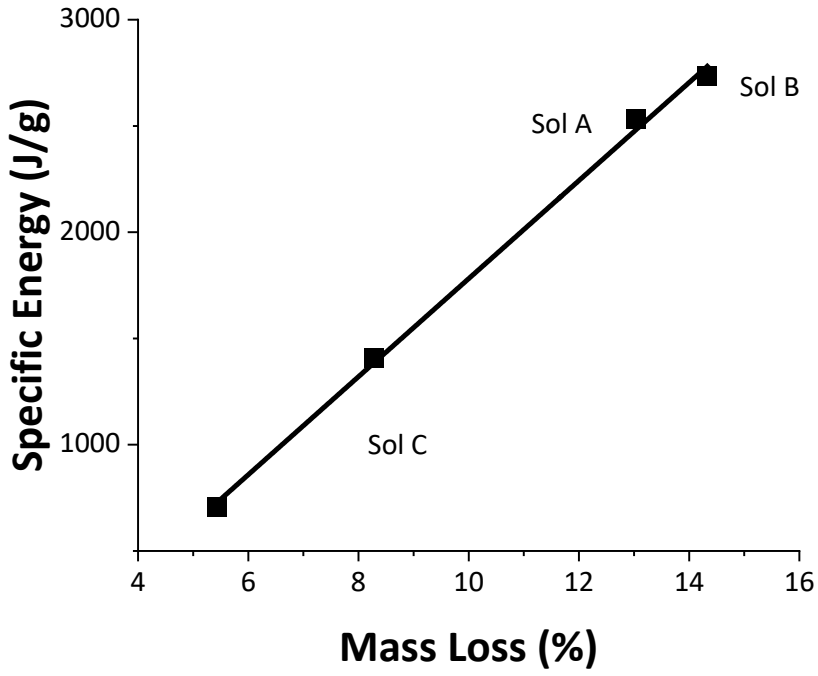

Figure 4-4: Specific energy vs. mass loss above 500°C for solutions A, B, and C. The specific energy was adjusted to account for the potential loss of excess sodium and potassium above the crystallization temperature (see Appendix). The specific energy is relative to the mass loss above 500°C.

which do not decompose appreciably at typical platinized silicon substrate processing temperatures (e.g. 750°C) will remain in the film as seen in Figure A-8, in the appendix.

Films from solutions with low specific energy of reactions above 500°C, such as aged solution C, tended to have more retained carbon at the end of the TGA experiment (see Figure 4-5), and in the final crystalline films (see Figure 4-6, c.f. Figure A-8). TGA-MS spectra in appendix Figure A-7 demonstrate the inability to fully remove carbon from the aged KNN-C powders at typical thin film processing temperatures. Such behavior is presumably related to a low specific heat of reaction indicated on Figure 4-4, and films from those solutions did not have desirable electrical properties.

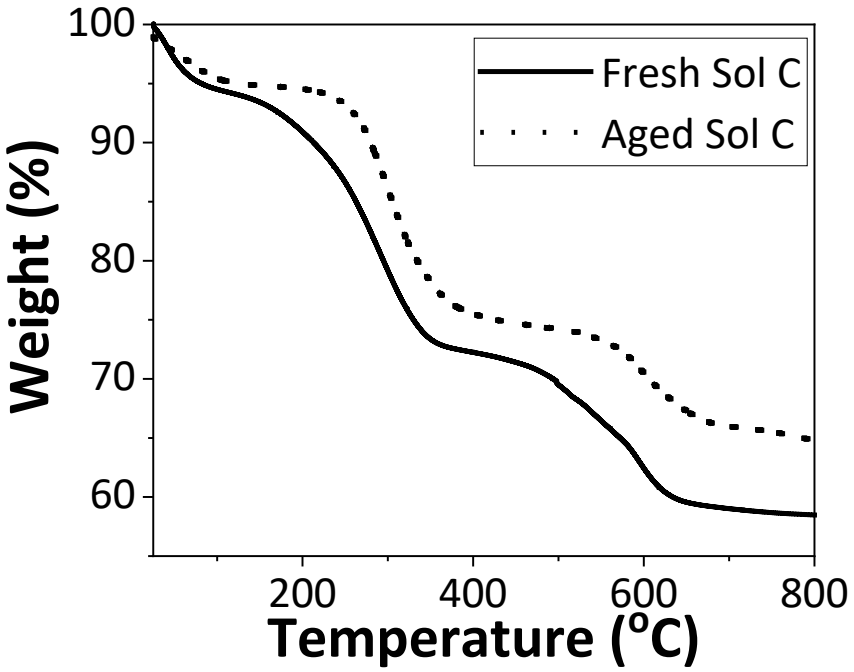

Figure **4-5**: A comparison of the TGA profiles of KNN-C powders from 1-week old solution and > 4-month old solution. Greater mass loss indicates better removal of organics.

The TGA-MS profiles for KNN-B and C powders from fresh solutions are remarkably similar to that of KNN-A (see Figure 4-3). The KNN-C powder was heated to 850°C; a rise in

CO_2 detection occurs above 800°C, correlating with an endotherm that appears on all the TGA-DSC plots (Figures A-2,3,4,5). This is attributed to the decomposition of residual carbon-containing species, including carbonates. Thermal data obtained for powders may not correlate completely with thin films due to the large surface area of films relative to the layer thickness, and more even heating, so that organics decompose more readily. Nonetheless, the data are helpful in understanding phenomena that occur in thin films.

Figure 4-6 confirms the presence of acetates below 300°C at 1016, 1046, 1421, and 1586 cm^{-1} [107]. Upon decomposition, potassium acetate decomposes to the intermediate oxalate [17], wich was identified at 1336 and 1650 cm^{-1} [108]. Sodium oxalate is expected to be present at similar wavenumbers. Spectra of fully crystalline KNN-C annealed at 650°C and 750°C reveal virtiually phase pure KNN, and a Nb-O peak is observed at 856 cm^{-1}. Na-O and K-O peaks are

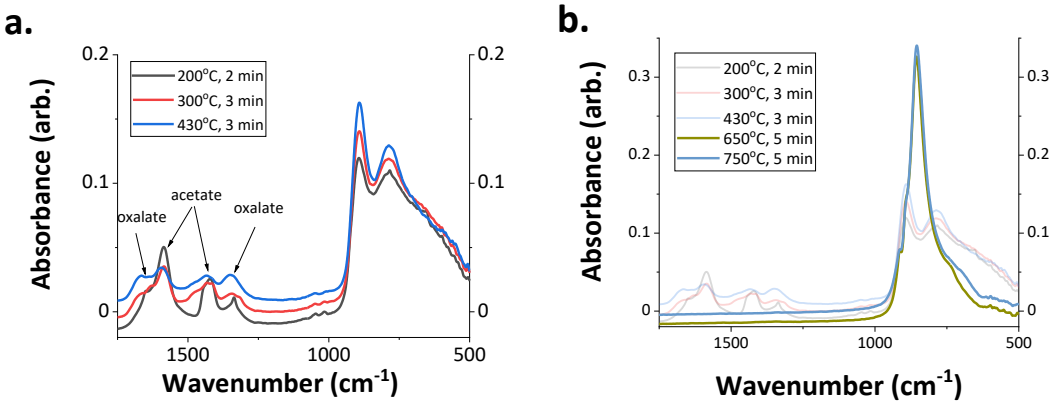

Figure **4-6**: FTIR spectra of partially and fully crystalline KNN-C deposited from 6-day old solution. (a) Following the drying and pyrolysis procedures for solution C from section 3.2, spectra of KNN-C after drying and pyrolysis steps. (b) Fully crystalline KNN-C is phase pure after crystallization at as 650°C and for 5 minutes. Oxalate and acetate identifications are according to NIST standard referecne spectra [107,108].

not observed because they are below 450 cm^{-1} which is the minimum detectable wavenumber by the instrument.

Simultaneous TGA-DSC on KNN-A, B, and C powders are reported in the Appendix. The rapid heat release above 500°C is attributed to exothermic decomposition reactions of the remaining carbon-containing groups. The crystallization of KNN is also exothermic, but the heat release is reported to be small compared to that from the decomposed organics (c.f. Figure 2-13) [60].

X-ray diffraction on post-thermal analysis powders (see Figure A-6) revealed significant amounts of hydrated potassium carboxylate salts only in KNN-C powders with the lowest specific energy of reaction above 500°C (see Figure 4-4). This suggests more complete removal of carbon is beneficial for crystallization. Similar techniques to promote crystallization have been reported elsewhere in the literature for PVP and EDTA modified KNN solutions [60,64,94,109,110].

Besides what was detected on the mass spectrometer, it is difficult to clearly discern the loss of excess Na and K during heat treatment in these experiments. Assuming all excess Na and K added to the solution volatizes as NaO/Na_2O and KO/K_2O, a mass drop of only 1-2% is expected (as shown in the Appendix). A 1-2% mass drop in between 300°C and 500°C and in-between the two major decomposition events was observed on all TGA-DSC plots (Figure A-2,3,4,5). Volatile alkalis have been reported in the literature for a range of polymer-modified KNN solution xerogels [60] in this same temperature range with 1-2% mass loss. Therefore, this mass loss prior to crystallization may be associated with to NaO/Na_2O and KO/K_2O volatility.

For all the manganese-doped solution methods reported here, three distinct peaks are observed above 500°C on DSC plots (see Figure 4-2, Figure A-2,3,4,5). In undoped KNN solutions, two distinct peaks are reported [20]. The two exothermic peaks reported elsewhere were attributed to decompositions of residual carbon-containing species and crystallizations

associated with sodium and potassium niobates. This is a source of sodium and potassium segregation in KNN [20]. In this work, for KNN-A powders, the first peak near 530°C is associated with sodium and is related to the decomposition of sodium oxalate [101]. The second peak near 606°C is associated with potassium and is related to the decomposition of potassium oxalate [102]. The affiliation of the third peak at 655°C, the least intense and at the highest temperature, is currently unknown. However, since it is accompanied with a mass loss and is observed on all TGA-DSC plots for KNN-A, B, and C, it may be related to the decomposition of an organic intermediate. For this reason, a crystallization temperature above 650°C should be chosen for Mn-doped KNN solutions.

4.3 Pyrolysis Study on KNN Films

The effect of pyrolysis conditions on the microstructure were observed for films made from the KNN-C solution. Films were dried at 200°C for 2 minutes, followed by a range of pyrolysis conditions, as described in Table 4-1. Samples were crystallized after each pyrolysis. This was repeated 4 times for samples 1, 2 and 5, and 3 times for samples 3 and 4. The average thickness per layer was 45 nm. Each sample had a distinct microstructure because of the altered pyrolysis conditions (see Figure 4-7).

Pyrolysis only at 300°C resulted in abnormal grain growth, with large grains over 100 nm and small grains 10s of nanometers in length (see Figure 4-7, a). Adding a second pyrolysis step at 430°C improved the homogeneity of grain sizes and reduced porosity (Fig. 4-7, c and e). Exposing the film to ultraviolet irradiation at 240°C without further pyrolysis produced microstructures similar to sample 1, with small pores and elongated grains (Fig. 4-7, b). Pyrolysis at 430°C after ultraviolet irradiation significantly improved grain uniformity and film density, but

some grains were slightly elongated (Fig. 4-7, c). This film had the densest cross-section and some indication of columnar growth half-way through the thickness (Fig. 4-7, f). Pyrolysis

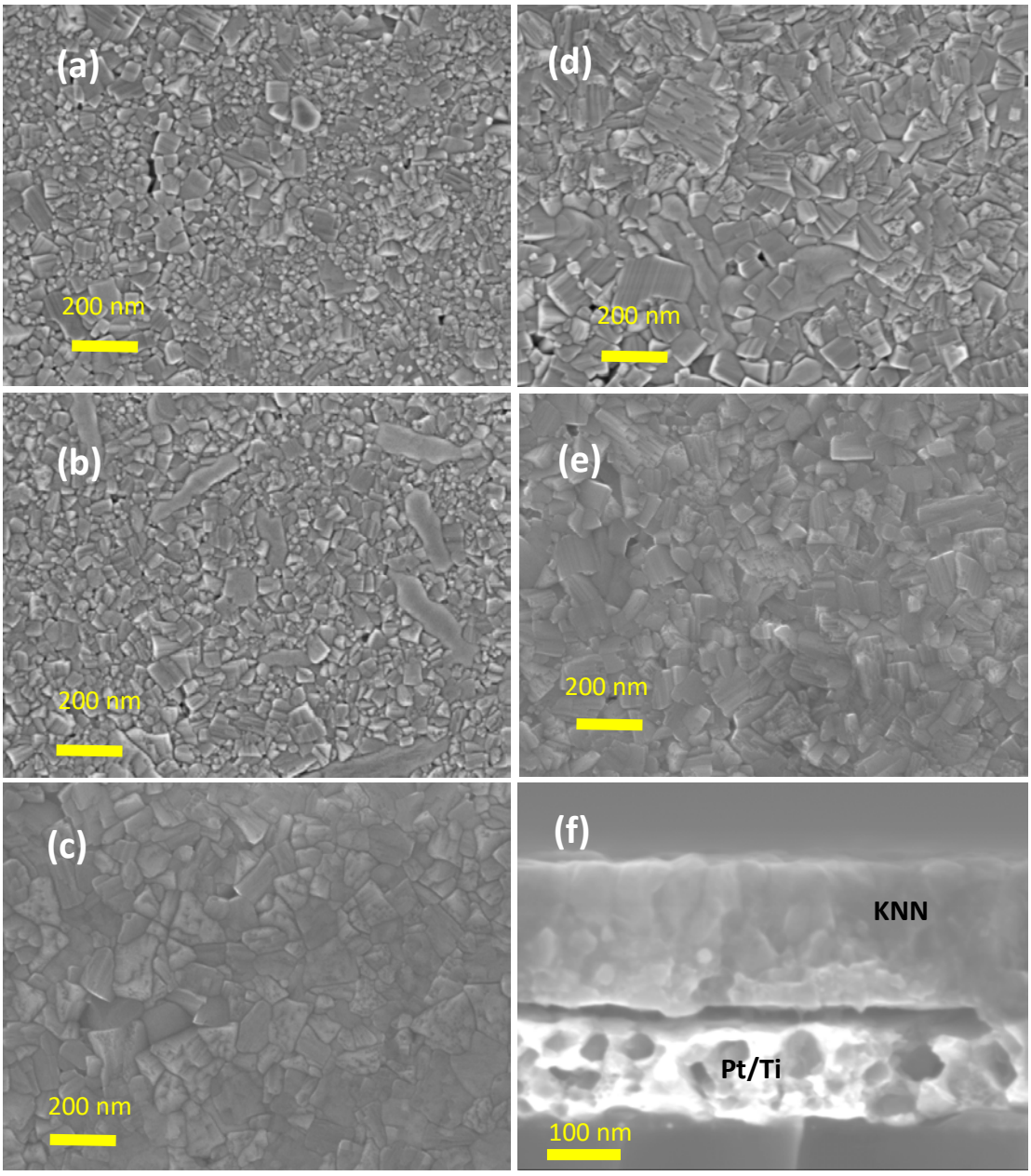

Figure **4-7**: Comparative study of the effect of pyrolysis temperature on the KNN-C microstructure. FESEM surface micrograph of samples 1, 2, 3, 4, and 5 in Table 4-1 are (a), (b), (c), (d), and (e), respectively. Image (f) is a cross-section of sample 3.

immediately to 430°C resulted in porosity and non-uniform grain sizes due to rapid removal of organics (Fig. 4-7, d) [35]. Improvements in film density were attributed to more effective burnout of organics before crystallization. From the results of this study, the sample 5 process was chosen for route C.

Table **4-1**: Comparative study of pyrolysis on microstructures from KNN-C films.

Sample	1	2	3	4	5
Dry at 200°C, 2 min	X	X	X	X	X
UV exp. at 240°C, 3 min		X	X		
Pyrolysis at 300°C, 3 min	X				X
Pyrolysis at 430°C, 3 min			X	X	X
Anneal at 750°C, 5 min	X	X	X	X	X

4.4 Microstructure

KNN-A, B and C films have distinct microstructures; their grain sizes, textures and film surfaces differ. Figure 4-8 show FESEM surface and cross-section images of approximately 1 μm thick deposited films from the three solutions. The average grain size in KNN-A, B, and C films are 91 nm, 227 nm, and 169 nm, respectively, when annealed in standing air. KNN-A films have non-uniform grain sizes and pores in-between grains. The small grain size generates a tortuous path between the top and bottom electrodes, which can contribute to high breakdown

strength since grain boundaries perpendicular to the applied field act as a barrier for the passage of current. The variance in grain sizes is quite small for KNN-A compared to the other two

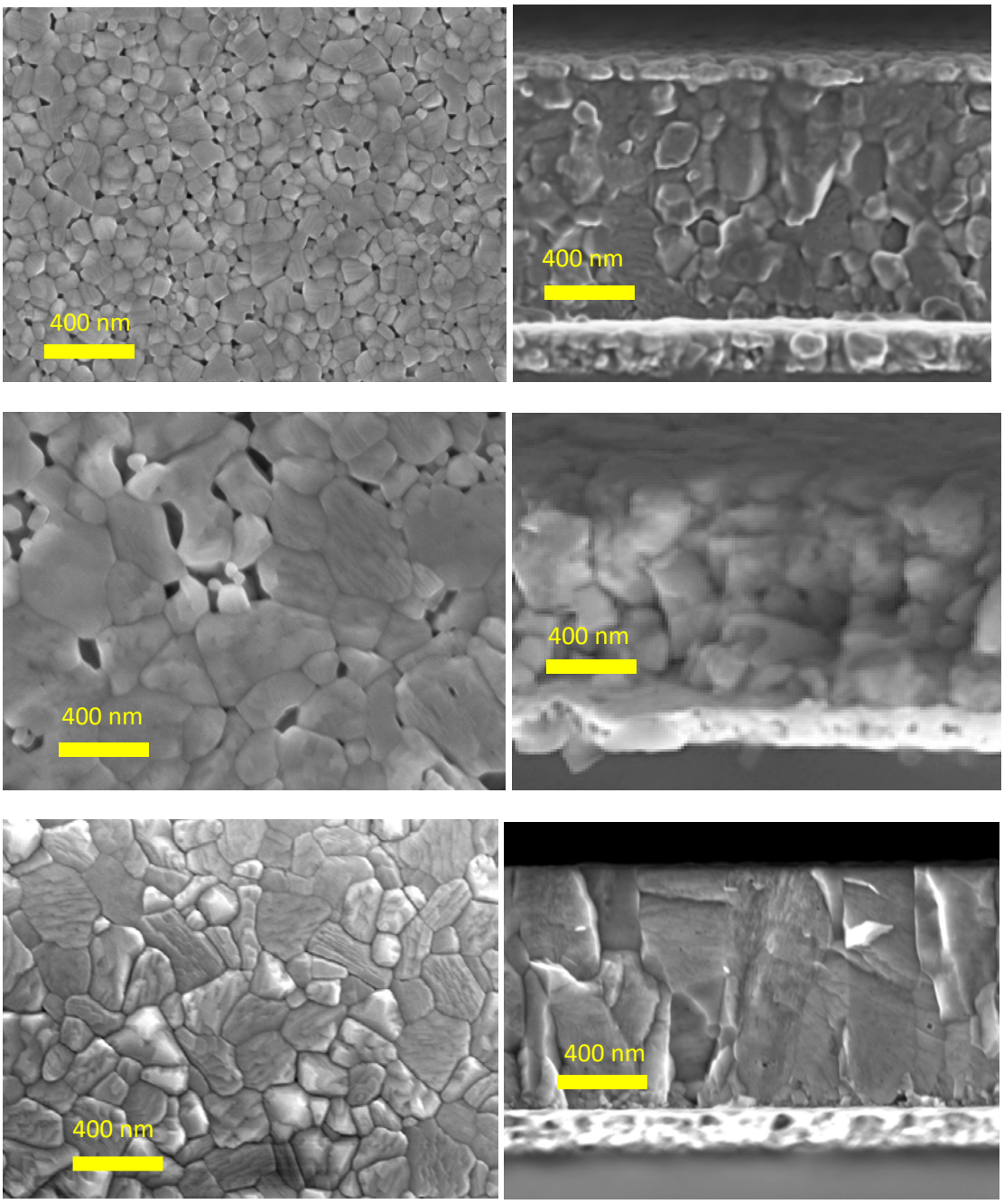

Figure **4-8**: FESEM images of KNN-A, B, and C films annealed in standing air. They are (a), (b), and (c) respectively [91].

solution methods. Grain size inhomogeneity is often an indicator of composition inhomogeneity since the grain growth is affected by the different diffusion rates of sodium and potassium [80]. KNN-B films have the largest grain size. Some grains span the whole thickness of the film; large pores exist in-between grains and the film surface is not smooth. Abnormal grain growth is observed here, and this microstructure is not characteristic of strongly insulating KNN films [80]. KNN-C films have columnar grains and small intragranular pores on the scale of a few nanometers; fewer pores are evident after two-step pyrolysis than after one-step pyrolysis at 300°C. KNN-C films have the densest microstructures; they are smooth and have optically reflective surfaces. Typically, columnar KNN films are not desirable from the CSD route because they are associated with intergranular leakage current pathways [22]. The density of this microstructure suggests there may not be a significant amount of secondary phase in the grain boundary to contribute to conduction.

4.5 Composition Segregation

The chemical homogeneity of KNN-A, B and C films was investigated using energy dispersive spectroscopy (EDS) [91], as seen in Figure 4-9. KNN-A was more compositionally homogeneous than KNN-B and C. The latter had regions rich in Na and K; the Na and K rich clusters (Figure 4-9) were believed to be due to either inadequate mixing during solution preparation or nucleation and growth phenomena discussed in the next chapter. Inhomogeneity also contributed to variations in grain size [81]. The Nb concentration was homogeneous across all film surfaces.

Composition segregation diminished with prolonged refluxing up to 60 hours [96,56]. KNN-A included an alkali homogenization step by mixing alkali acetate precursors in acetic acid prior to adding Nb-ethoxide; this step was not included in KNN-B and C.

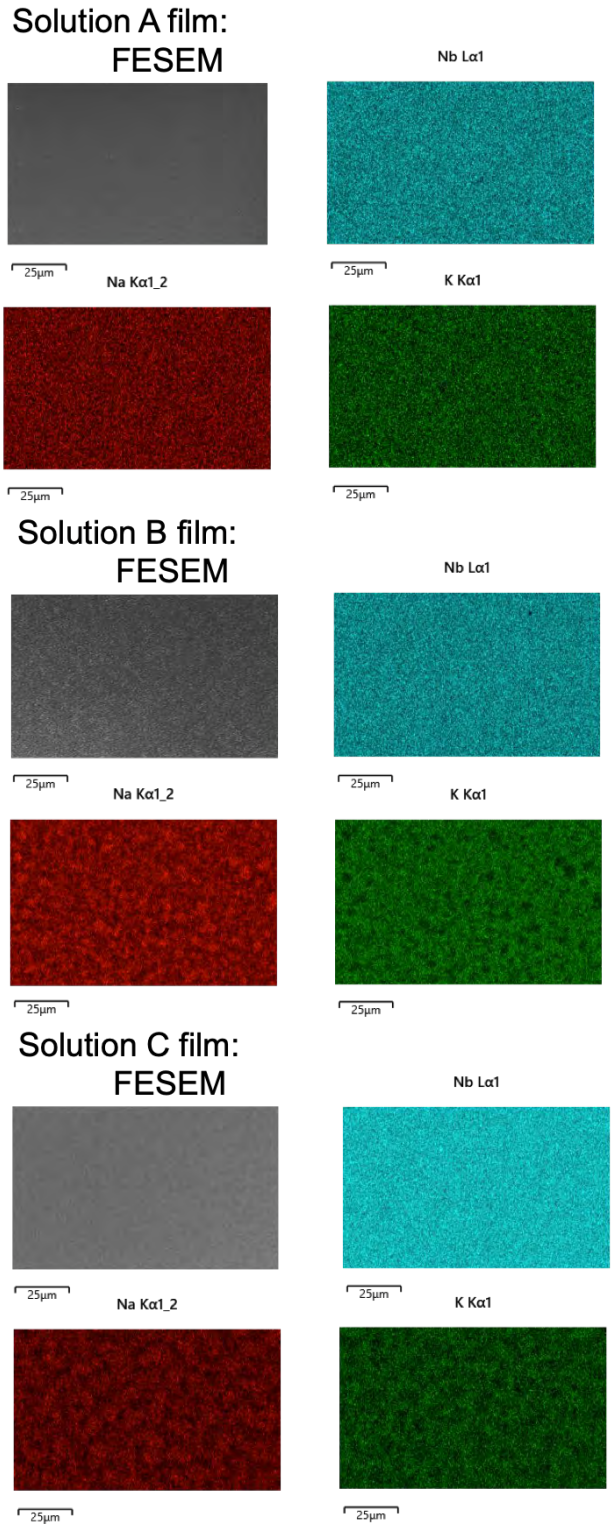

Figure **4-9**: Energy dispersive spectroscopy (EDS) maps show qualitative spatial composition data for KNN-A, B, and C films [91].

Sodium acetate and potassium acetate were added to solution B in staggered steps; it is unknown whether this favored the formation of Nb-O-Na linkages over Nb-O-K to offset the higher reactivity of potassium. The solution C process mixed alkali precursors together in acetic anhydride and they dissolved when the niobium complex with 2-MOE was added. A small modification to this method would be to mix alkali precursors in part acetic acid and part anhydride to encourage homogenization before mixing with niobium. This technique can also reduce the complexity of the solution-making process, eliminating the need for a vacuum distillation step since water adsorbed to the precursors will react with the anhydride to form acetic acid.

The literature discusses the cause of phase segregation in KNN films. Chowdhury et al. did not use an alkali homogenization step, which may have led to Na and K segregation. Segregation diminished with prolonged refluxing up to 60 hours [20,65]. They determined that one source of composition segregation was due to the separate nucleation and growth of Na and K rich phases, discerned by two distinct exothermic crystallization peaks in their thermal analysis of their solutions.

4.6 X-ray Diffraction

Figure 4-10 shows X-ray diffraction patterns for KNN-A, B, and C thin films. All films crystallized into the perovskite phase and are mostly phase pure. The Lotgering factor was used to compare the strength of (100) orientation in the films [111].

$$f_{(00l)} = \frac{P_{(00l)} - P_0}{1 - P_0}$$

$$P_{(00l)} = \frac{\sum I_{(00l)}}{\sum I_{(hkl)}}$$

$$P_0 = \frac{\sum I_{0(00l)}}{\sum I_{0(hkl)}}$$

$\sum I_{(00l)}$ is the sum of all the peak intensities for the (00*l*) family peaks and $\sum I_{(hkl)}$ is the sum of all the peaks in the XRD pattern. The subscript "0" indicates the peak intensities for a randomly oriented sample. Table 4-2 shows the Lotgering factors for KNN-A, B, and C. KNN-C were the most {100} oriented, likely due to their dense and columnar microstructure. (Columnar grains result from preferential growth over nucleation during early stages of crystallization, and cause the film to grow from the substrate or previous layer). Acetic anhydride effectively delayed hydrolysis, preventing the formation of large clusters prior to heat treatment. Fine clusters likely improved the sinterability of the thin films, improving their density and orientation.

Table **4-2**: Lotgering factors for {001} planes for KNN-A, B and C films [91].

Solution	Lotgering factor {001}
A	0.31
B	0.43
C	0.81

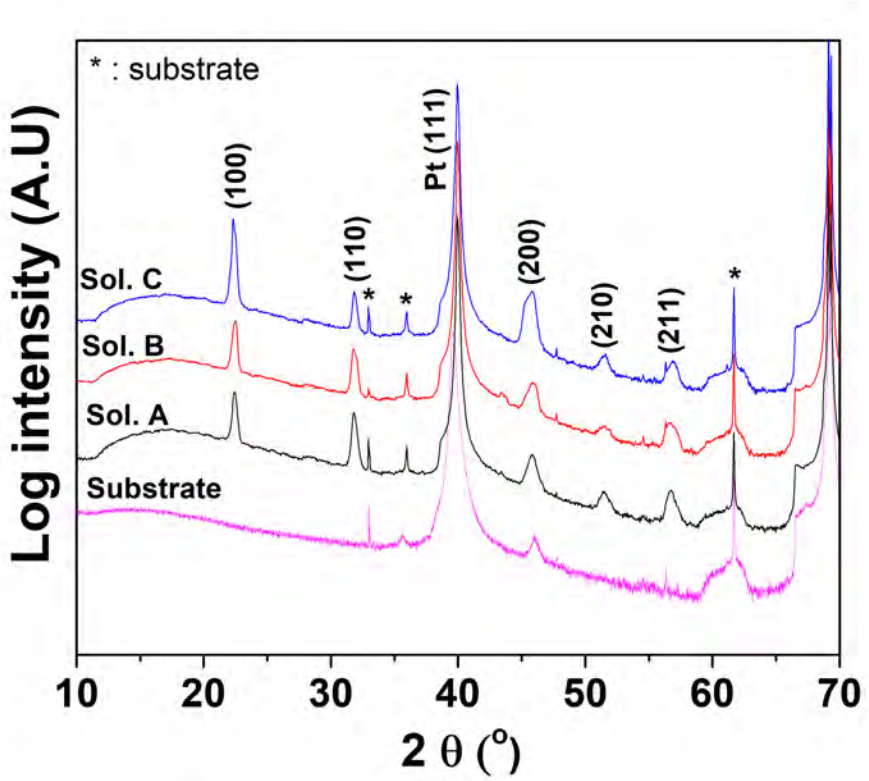

Figure **4-10**: X-Ray diffraction patterns for KNN-A, B, and C films. Substrate peaks are indicated by an asterisk [91].

Peak splitting was observed on the KNN-C sample more than KNN-A and KNN-B.

4.7 Electrical Properties

At 1 kHz KNN-C films had a relative permittivity of 893; films from solutions A and B both had a relative permittivity of 750. This is shown in Figure 4-11 (a). KNN-A and C have low dielectric losses near 1.6%; KNN-B had a higher dielectric loss near 2.5% at 1 kHz. The relative permittivity of KNN-C was close to that reported for dense Mn-doped KNN films [64,109].

The current density of KNN-A, B and C films varied. Current density as a function of electric field is shown in Figure 4-11 (b). KNN-B films had the highest leakage currents. KNN-C

films maintained low leakage current around 10 nA/cm^2 until breakdown at 280 kV/cm. KNN-A films also maintained low current density around 10 nA/cm^2 until breakdown at 610 kV/cm^2, despite the porous microstructure. As reported in the literature, 0.5% Mn-doped KNN has a leakage current around 360 nA/cm^2 and a breakdown field near 200 kV/cm [109].

The literature suggests that electrical properties are strongly related to film microstructure and that smaller grain sizes are preferable. Kupec et al. found that an increase in excess alkali content increased grain size however, a conductive amorphous material was found near pores and within grain boundaries [22]. The amorphous material was detected by transmission electron microscopy and atomic force microscopy with conducting probe tips.

The results in this thesis suggest the importance of chemical homogeneity for high breakdown strength. Although highly porous, KNN-A had the highest breakdown strength because of better chemical homogeneity.

Figure 4-11 (c) shows polarization-electric (P-E) field hysteresis loops in KNN-A, B, and C films. The coercive fields are 50 kV/cm, 36 kV/cm, and 25 kV/cm, respectively. KNN-B and C films have an imprint offset of 6 and 8 kV/cm, respectively. This might be due to internal fields as a result of composition segregation. The coercive field appears to reduce with increasing grain size and diminishing porosity. The remanent polarizations (P_r) are 5.7, 6.6, and 4.0 μC/cm^2 for routes A, B, and C, respectively. KNN-B has the largest P_r due to its large grain size and low {100} Lotgering factor. KNN-C has the lowest P_r, possibly because of its high {100} Lotgering factor.

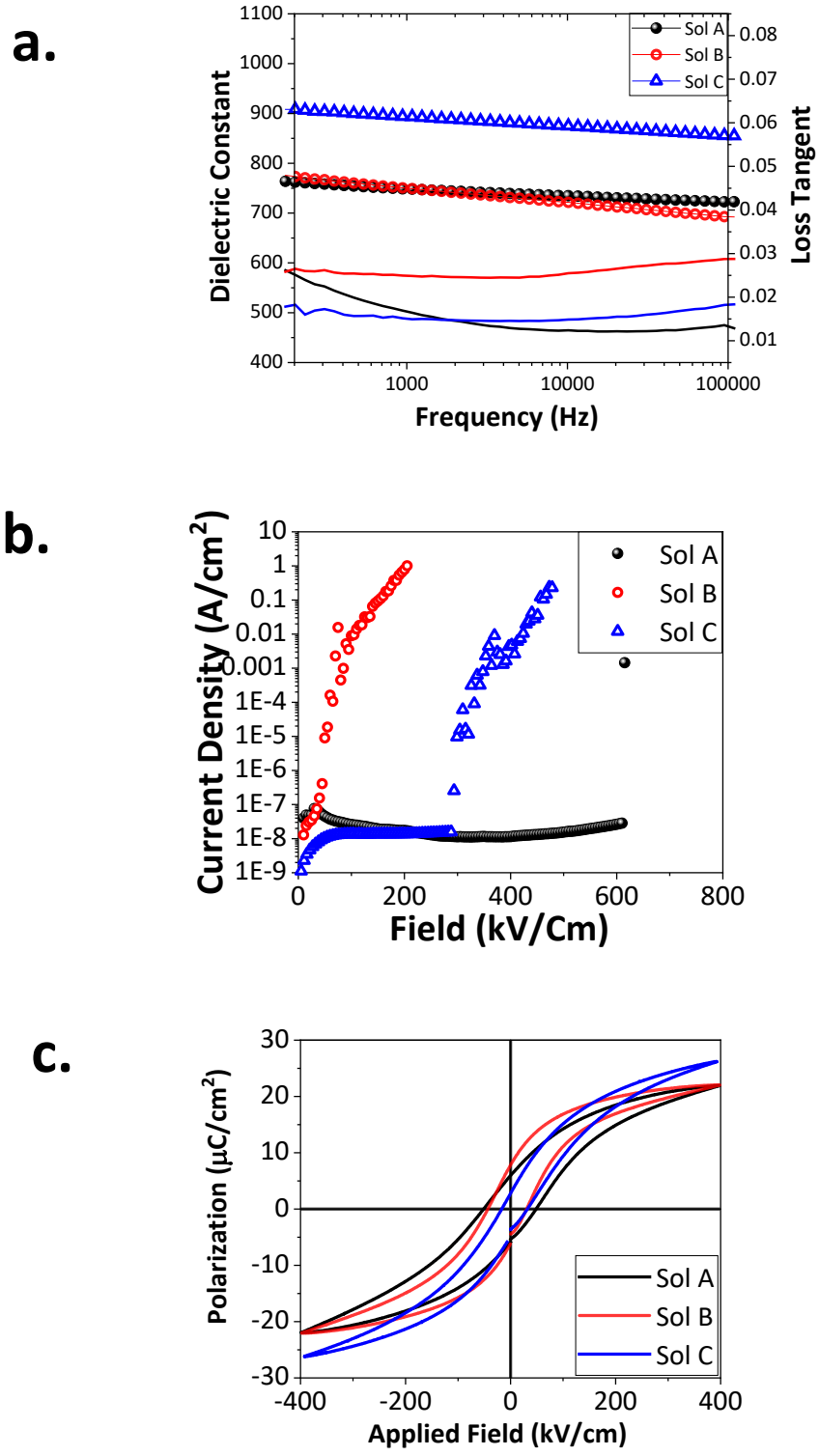

Figure **4-11:** Dielectric constant (ε_r) and loss (tan(δ)) (a); current density plots (b); Polarization-electric field hysteresis loops (c) for KNN-A (black), B (red), and C (blue) films [91].

Averaging of the polarization vector has been explained in the dissertation of Huseyin Yilmaz [112]. Consider the polarization measured between the top and bottom electrodes in the direction perpendicular to the film surface as

$$P_i' = \begin{bmatrix} 0 \\ 0 \\ P_3' \end{bmatrix}$$

The measured polarization is in the 3 direction, where 3 indicates the direction normal to the film surface, and directions 1 and 2 are perpendicular to each other within the plane of the film. In a sample with random orientation, there are grains oriented in many directions. Therefore, the polarization is an average of the "3" component of all the polarization vectors in between the electrodes.

In orthorhombic KNN, the spontaneous polarization axes are the <110> directions, so the greatest polarization will be achieved in grains with {110} orientation, shown in Figure 4-12. The unit cell will polarize in the direction closest to the direction of the applied electric filed, so the polarization direction with the smallest angle to the electric field is considered.

For the pseudocubic unit cell, the <110> makes a 90° angle with {110}, therefore 100% of the polarization of {110} oriented grains will contribute to the measured polarization, $P_{3,i}$.

$$P_{3,i}' = P\cos(\theta)$$

The polarization in grains which are not {110} oriented will contribute less response to the measured P_3'. For example, the minimum angle between the <110> and the normal of {100} – which is the direction of applied field in {100} oriented grains – is approximately 45°. Applying the equation above, about 71% of the polarization of {100} oriented grains will contribute to the measured polarization, $P_{3,i}$, assuming no polarization rotation.

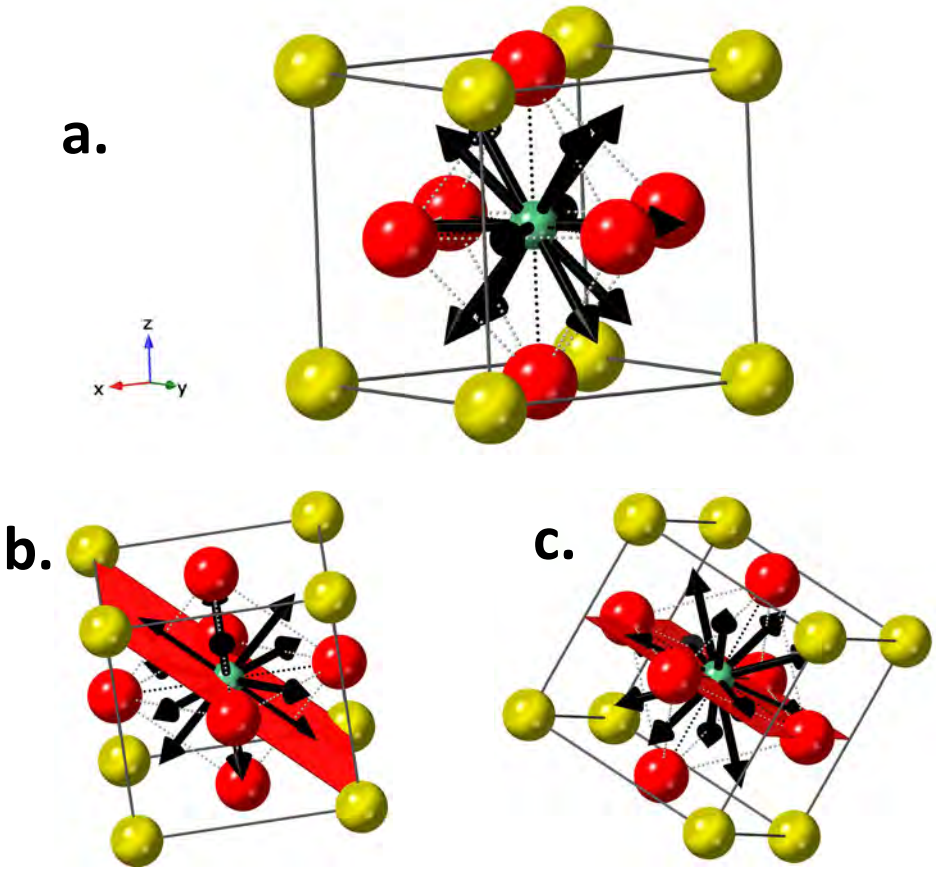

Figure **4-12**: A pseudocubic perovskite cell of KNN (a) orthorhombic unit cell of KNN showing the 12 <110> directions. The <110> directions relative to (110) (b). The <110> directions relative to (100) (c). Yellow atoms are the A-site, teal atom the B-site, and red atoms the O-site.

The actual polarization state between the electrodes will be

$$P_i = \begin{bmatrix} P_1 \\ P_2 \\ P_3 \end{bmatrix}$$

where P_1, P_2, and P_3 are due to the sum of the polarization vectors in all directions. The polarization of off axis grains will be at the smallest allowed angle to the applied electric field in the "3" direction. Therefore, textured {100} KNN will have approximately 71% of the possible polarization in textured {110} KNN.

Mixing rules can be applied based on the Lotgering factor, f, to estimate the total polarization. To simplify calculations, it is assumed that only {100} and {110} oriented grains exist in the films.

$$P_3' = f \times 0.707x + (1 - f)x$$

where x is the magnitude of the total polarization, and the coefficients are fractions of polarization in the "3" direction for {110} and {100} oriented grains. Not accounting for polarization rotation gives total remanent polarizations (P_i) of approximately 6.3, 7.6, and 5.2 $\mu C/cm^2$ for KNN-A, B and C, respectively.

4.8 Effects of 2-step Pyrolysis

When subjected to two-step pyrolysis, KNN-A films behave similarly to KNN-C films [93]. Film density improves and the average grain size increases from 91 nm to 132 nm (see Figure 4-13). The dielectric constant ε_r increases from 750 to 780 (see Figure 4-14). Although the cross-section was not columnar, there were fewer grains through the thickness. It is likely that a fully columnar film does not form due to one of two reasons: 1) partial hydrolysis of the solution upon exposure to humidity, or 2) porosity introduced at the drying step which increased the number of nucleation sites. The change in the microstructure of the KNN-A film with 2 step pyroloysis is due to more effective burnout of organics before crystallization. There is no improvement in orientation (see Figure 4-15), and a sharp $K_4Nb_6O_{17}$ (020) peak appeared at 28° on the XRD pattern [113], due to more extensive composition segregation [52]. The existence of the excess potassium $K_4Nb_6O_{17}$ phase indicates extensive composition segregation in the early stages of nucleation and growth, where local concentrations of potassium were 20% greater than stoichiometric values for KNN [52]. The breakdown strength decreased from 600 to 230 kV/cm,

resulting in leakage current profiles similar to films deposited from KNN-C with 2-step pyrolysis [31].

Conversely, KNN-C following 1 step pyrolysis were still columnar through the whole thickness, and had higher leakage current densities, lower breakdown fields, and large space charge contributions to the dielectric constant.

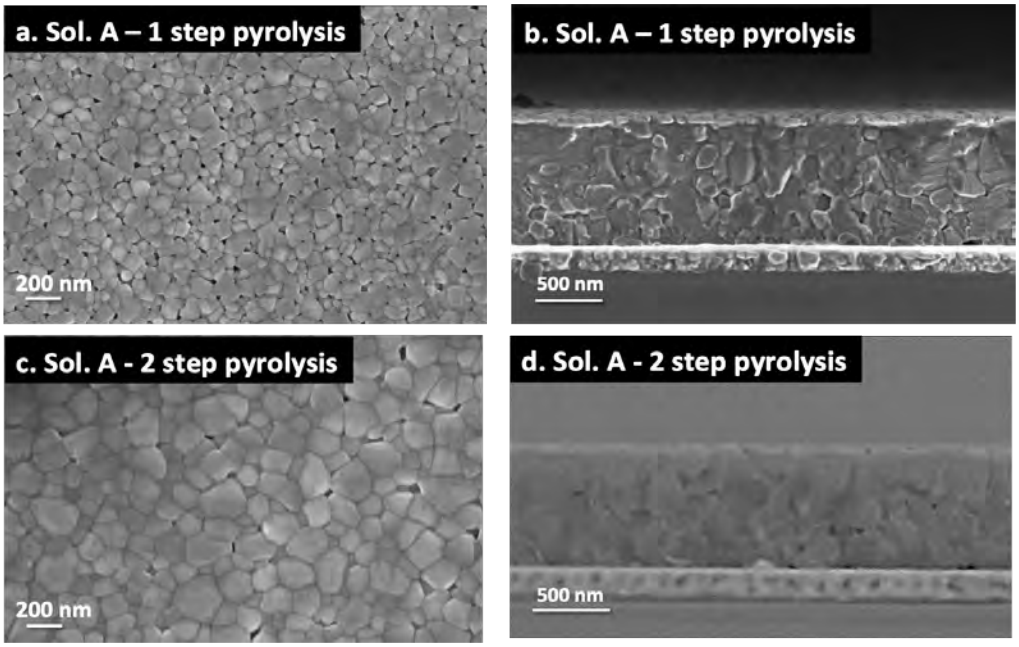

Figure **4-13**: Comparison between microstructures of films annealed after 1 pyrolysis step and 2 pyrolysis steps for KNN-A [91].

It was previously reported that conductive pathways in grain boundaries cause low breakdown strength [22]. Secondary phase $K_4Nb_6O_{17}$ is hydrophilic and may form a conductive pathway and cause low breakdown strength if situated in the grain boundaries [113,114]. Since grain boundary surface area decreases with increasing grain size, it is easier to form a conductive pathway in columnar or large grain microstructures [91]. This may explain why KNN-A with the two-step pyrolysis has a lower breakdown strength than with 1-step pyrolysis.

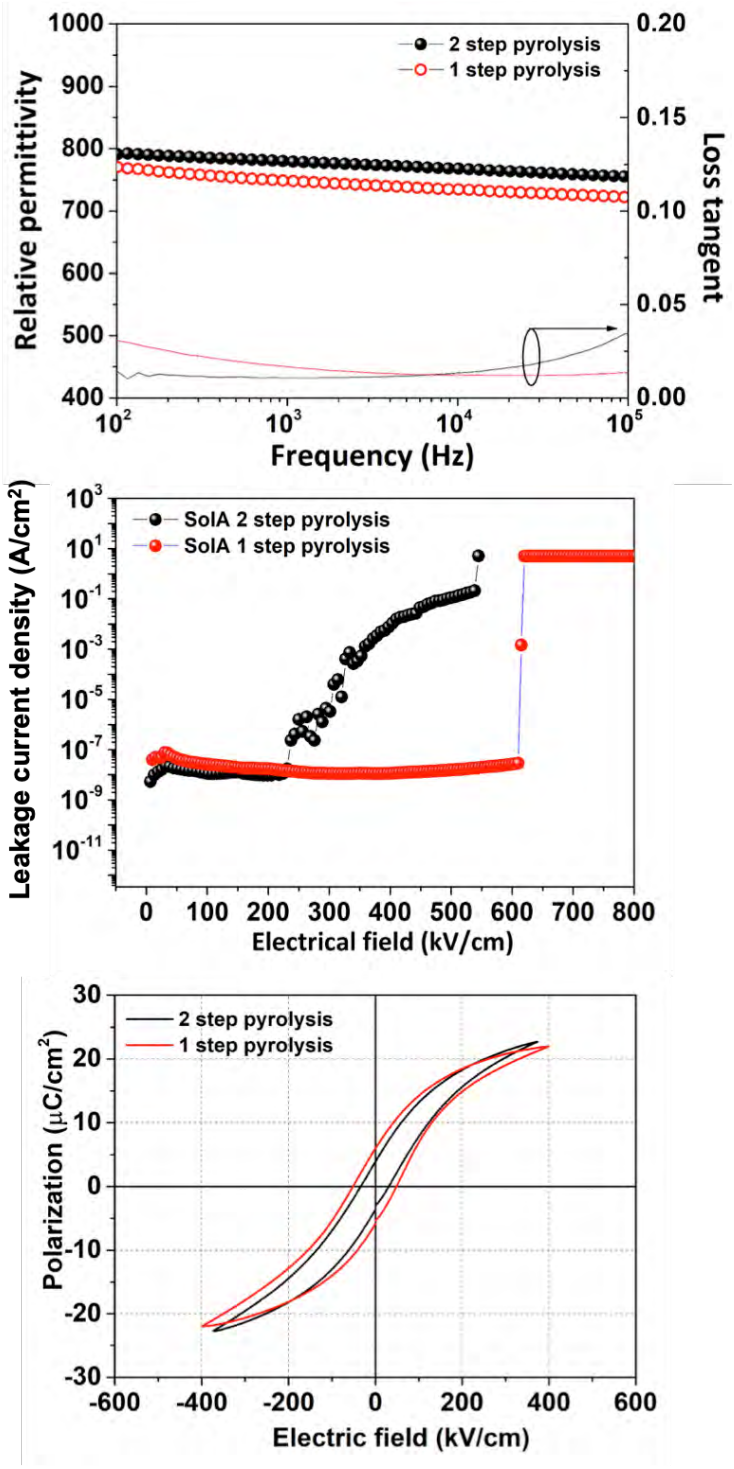

Figure **4-14**: Dielectric constant (ε_r) and loss (tan(δ)) (a); current density plots (b); Polarization-electric field hysteresis loops (c) for KNN-A films with 1-step and 2-step pyrolysis [91].

Finally, 2-step pyrolysis reduced the coercive field and remanent polarization of KNN-A films. In summary, varying processing conditions have a profound effect on KNN quality.

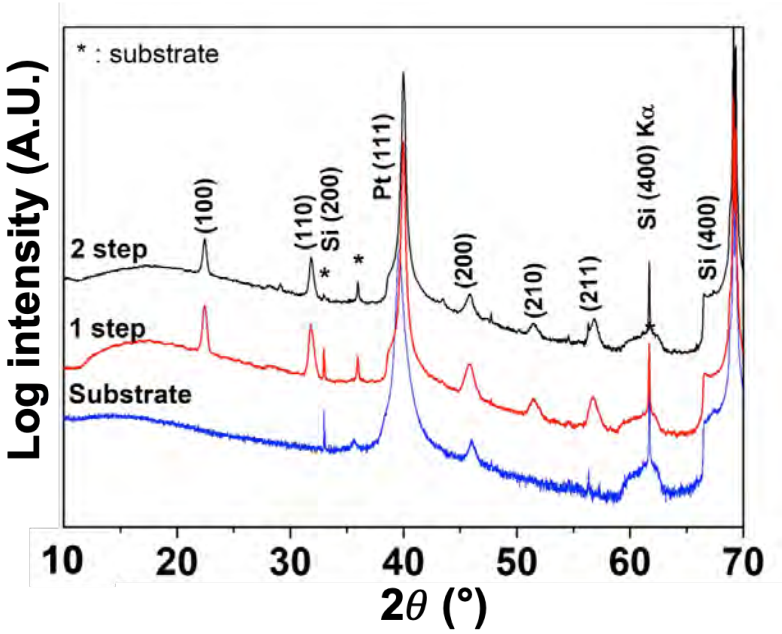

Figure **4-15**: X-ray diffraction patterns for films annealed after one pyrolysis step and two pyrolysis steps from solution A [91].

4.9 Comparative Anneal Atmosphere Study

The consequence of annealing KNN films in 2 standard liters per minute (SLPM) oxygen flow versus standing air was studied. The thin film designated KNN-D in this section follows the same process as solution A, but did not undergo a final distillation step in the solution-making process, and contains 1% Mn; hereafter this film type will be referred to as KNN-D. KNN-D was less porous than KNN-A, and had a higher breakdown field [91]. The average grain size of films deposited from solution D and solution B increased from 91 nm to 222 nm, and from 227 nm to

443 nm, respectively, when annealed in 2 SLPM oxygen flow, compared to standing air (see Figure 4-16). KNN-C had a negligible change in the average grain size. All routes experienced a reduction in porosity due to oxygen flow, likely due to the more effective removal of residual carbon. KNN-C experienced a reduction in layer thickness from 39 nm/layer to 33 nm/layer in 2 SLPM oxygen flow, while KNN-A experienced a negligible reduction in thickness.

The annealing environment influenced the dielectric properties (see Figure 4-17). 2 SLPM oxygen flow increased the ε_r of KNN-B from 750 to 1140, likely due to the increase in grain size and reduction in porosity [115]. Unfortunately, most electrodes from route B annealed in oxygen flow were shorted. The small increase in ε_r and tan (δ) for KNN-A were likely due to an increase in density and the elimination of pores. The reduction of ε_r of KNN-C annealed in oxygen may be due to a decrease in thickness.

Leakage current profiles responded differently in the different solution types (see Figure 4-18). In KNN-C, the breakdown strength increased and leakage current decreased by annealing in 2 SLPM oxygen in a very limited number of measuements. This is attributed in part to an increase in density and a reduction in intragranular porosity. KNN-D had an opposite trend, where annealing in oxygen increased the leakage current and reduced the breakdown strength, although there was a reduction in porosity. Although not investigated here, the literature supports that the concentration of oxygen vacancies was reduced for KNN-C by annealing in higher pO_2, and it was shifted higher for KNN-D under the same conditions [67,68]. This is attributed to differences in the reactions involving carbon during crystallization. For KNN-D, annealing in standing air produces a ferroelectric film with a breakdown field of 705 kV/cm, averaged over three electrodes. It is unclear whether reduction in porosity, doping with 1% Mn, or omitting the last distillation step caused an increase in breakdown field-6b. KNN-D was denser compared to KNN-A, and increase in breakdown strength is attributed in-part to this.

KNN-D and KNN-C films maintained leakage currents below 10^{-6} A/cm^2 prior to the breakdown field. KNN-C annealed in oxygen produced the lowest maintained leakage current: under 4 nA/cm^2 at 400 kV/cm, prior to breakdown. Films deposited from solution B could not maintain a low leakage current over a few 10s of kV/cm, and neither of them could be poled. Only KNN-A and KNN-C films could be poled adequately for piezoelectric measurements. Films from Solution A annealed in oxygen degraded over time to an extent where they could not be poled.

It is speculated that the trends observed in leakage current may be due to composition segregation during the initial stages of crystallization and the segregation of small amounts of non-perovskite material to the grain boundaries, compared to excessive amounts of secondary phase in Figure A-8. Secondary phases become apparent during processing; a white powder-like substance appeared on the film surface as the number of crystallized layers increased. This may indicate residual alkali form carbonates at the surface. Films with this feature are usually not measurable due to shorting of the electrodes. A cross section from one of the films is shown in Figure A-8.

KNN-A films have a small grain size and a tortuous path to the bottom electrode. This creates a large grain boundary area, as compared to columnar films. It would be important in future work to assess the distribution of any conducting secondary phases at the grain boundaries to determine whether they exist, and how the connectivity of this second phase changes with the grain size.

It was found that annealing in 2 SLPM nitrogen flow resulted in increased leakage current and lower breakdown strength for KNN-C films, most likely due to an increase in oxygen vacancies [67,68]. Despite having a columnar cross-section, multiple types of microstructures existed on the surface (c.f. Figure A-10) after annealing in 2 SLPM nitrogen, and the layer thickness increased by 9% relative to anneals standing air.

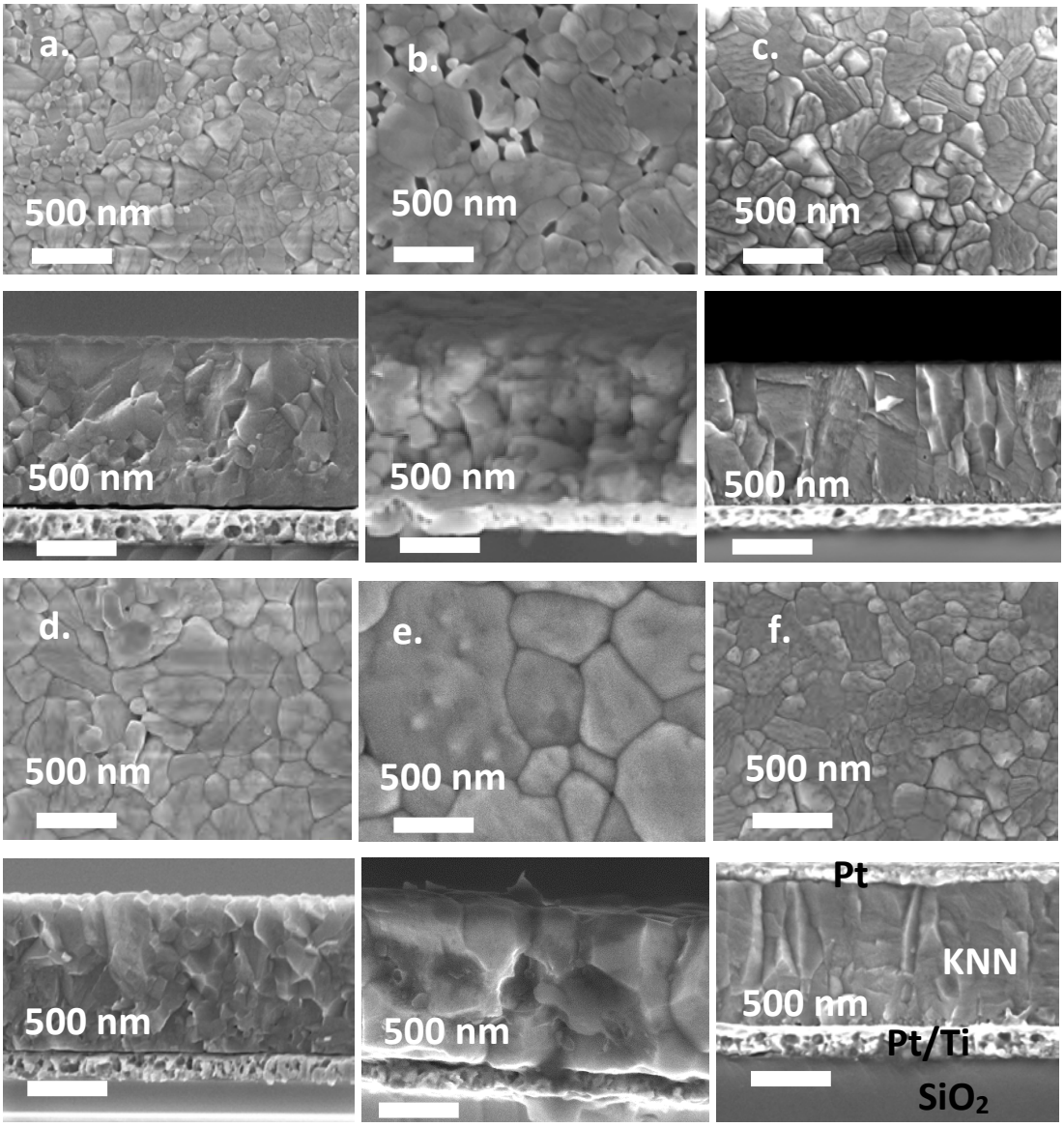

Figure **4-16**: FESEM surface (above) and cross-section (below) micrographs of films KNN-D, B, and C, annealed in standing air (a, b, and c) and 2 SLPM oxygen flow (d, e, and f), respectively.

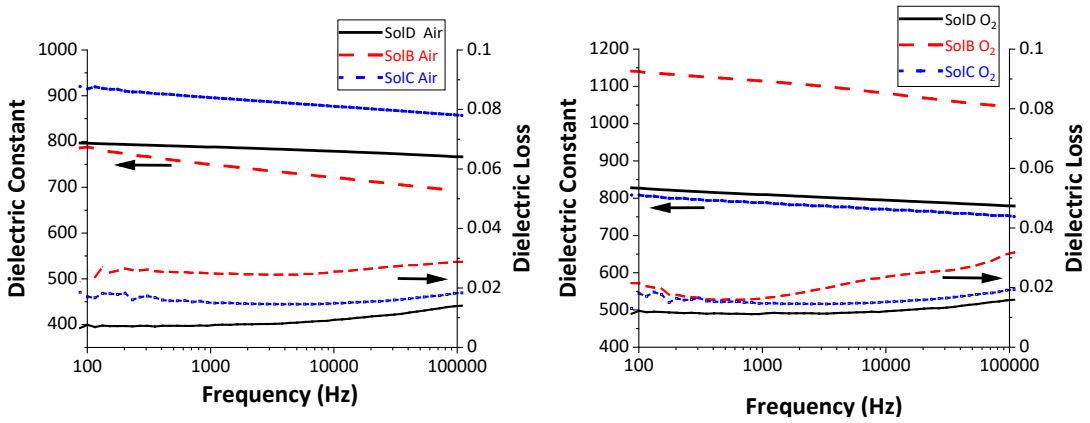

Figure **4-17**: Dielectric constant (ε_r) and loss tangent (tanδ) for KNN-D, B, and C, annealed in standing air (left) and 2 SLPM oxygen flow (right).

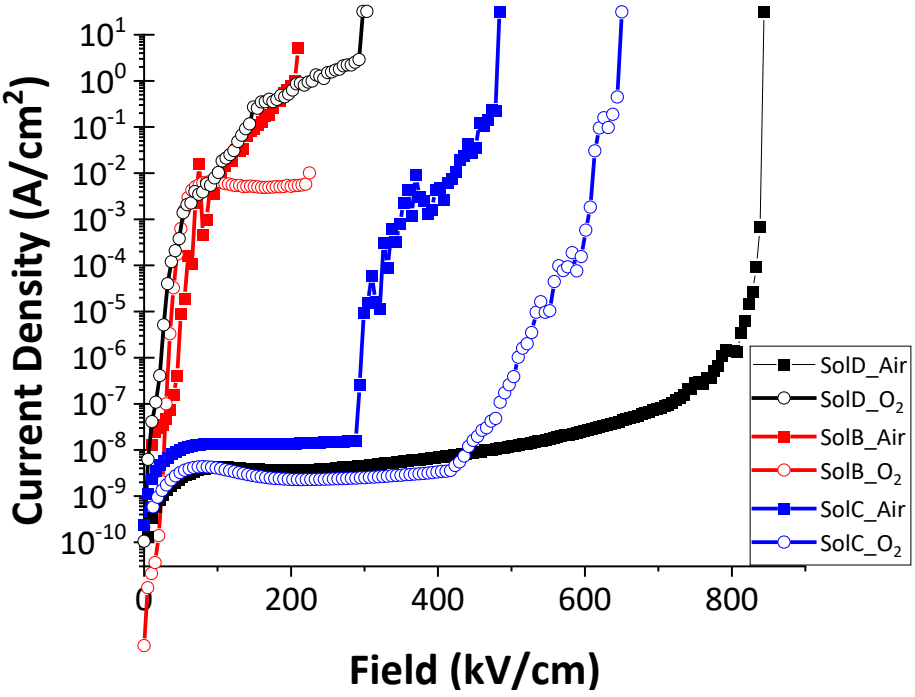

Figure **4-18**: Leakage current vs. applied field at the top electrode for KNN-D, B, and C, annealed in standing air or 2 SLPM oxygen flow.

Continuing from section 4.2: aged solution C is not useful for deposition due to changes in the decomposition behavior of the organics. TGA-MS spectra for powders from aged solution C showed a shift in decomposition products water and CO_2 to higher temperatures (see Figure A-7). Moreover, the TGA shows a decrease in the total mass loss by 6% at 800°C compared to powders from fresh solution, as shown in Figure 4-5. The lower total mass drop for powder from aged solution is due to retained carbonates and oxalates. The presence of oxalates and carbonates were confirmed in the FTIR spectra of the 1 μm film deposited from aged solution C, as shown in Figure 4-6.

Apart from considerations of morphology and crystallinity for KNN films deposited from acetylacetone modified solutions, in this work, a high specific heat of reaction above 500°C is characteristic of solution which produces ferroelectric KNN films. Solution B which had a high specific heat of reactions above 500°C and a large mass drop did not have a high breakdown field due to an inhomogeneous microstructure, but still produced a ferroelectric P-E hysteresis loop. Solution C with a large mass drop characteristic of high specific heat had a maximum breakdown field above 400 kV/cm and ferroelectric P-E hysteresis loops, despite its columnar microstructure and composition segregation which has shown in the literature to be linked with low breakdown strength for CSD KNN thin films [22]. Films deposited from the aged solution C did not show desirable electrical properties. This is unlike solution A which has a shelf-life under refrigeration that is still to be determined. It was found in this study the optimal time to deposit solution C is around 2 weeks after solution synthesis and storage in a refrigerator.

4.10 Piezoelectric Strain Coefficient -$e_{31,f}$ Measurements

Poling experiments were conducted on KNN-D films which exhibited a coercive field of 40 kV/cm by application of positive DC field to the top electrode (see Figure 4-20). This film was

highly insulating with good yield on multiple electrodes. Poling was carried out from 5 minutes to 15 minutes and at temperatures from room temperature to 140°C. It was found that poling was damaging to films when the current density rose above 0.1 A/cm^2. For example, an electrode poled at 150 kV/cm and 140°C for 5 minutes had a $-e_{31,f} = 1.7 \pm 0.2$ C/m^2 when the field was maintained throughout the cooldown and the current density surpassed 0.1 mA/cm^2. When the field was reduced to 100 kV/cm for the cooldown-step after the same poling procedure, to decrease the leakage current density, the measured $-e_{31,f}$ increased to 2.5 ± 0.3 C/m^2. Thus, highly insulating films with a low leakage current are desirable for KNN films.

KNN-D films annealed in air can be poled better than films annealed in 2 SLPM oxygen due to lower leakage currents. The best poling field was around 3.5 times the coercive field at 150 kV/cm. No trend in poling temperature dependence was observed between 70°C and 120°C for KNN-D films. The KNN films became more sensitive to voltage spikes at high temperatures, where high leakage currents indicated damage to the film and degradation of the piezoelectric properties. The voltage spikes were due to thermal breakdown events.

Milder poling recipes were attempted in an effort to raise the measured $-e_{31,f}$. Poling overnight at 70°C and 150 kV/cm resulted in an increase in $-e_{31,f}$ to 4.6 ± 0.46 C/m^2. The tan(δ) would typically increase from 0.7% to 1.5% after poling, and the capacitance would increase by about 10%, for electrodes which maintained a leakage current < 1 mA/cm^2 after poling.

Electrodes on KNN-C films annealed in oxygen could not achieve an $-e_{31,f}$ above 2 C/m^2 with the exception of one electrode which measured a value near 5 C/m^2 and was not reproducible. The KNN-C film annealed in 2 SLPM O_2 flow could be poled at fields higher than the coercive field, so the low measured was due to a defect other than leakage current. The maximum $-e_{31,f}$ near 2 C/m^2 could be due to a combination of composition segregation, tensile stress in the KNN film due to thermal expansion coefficient mismatch with the Si substrate, and incomplete poling.

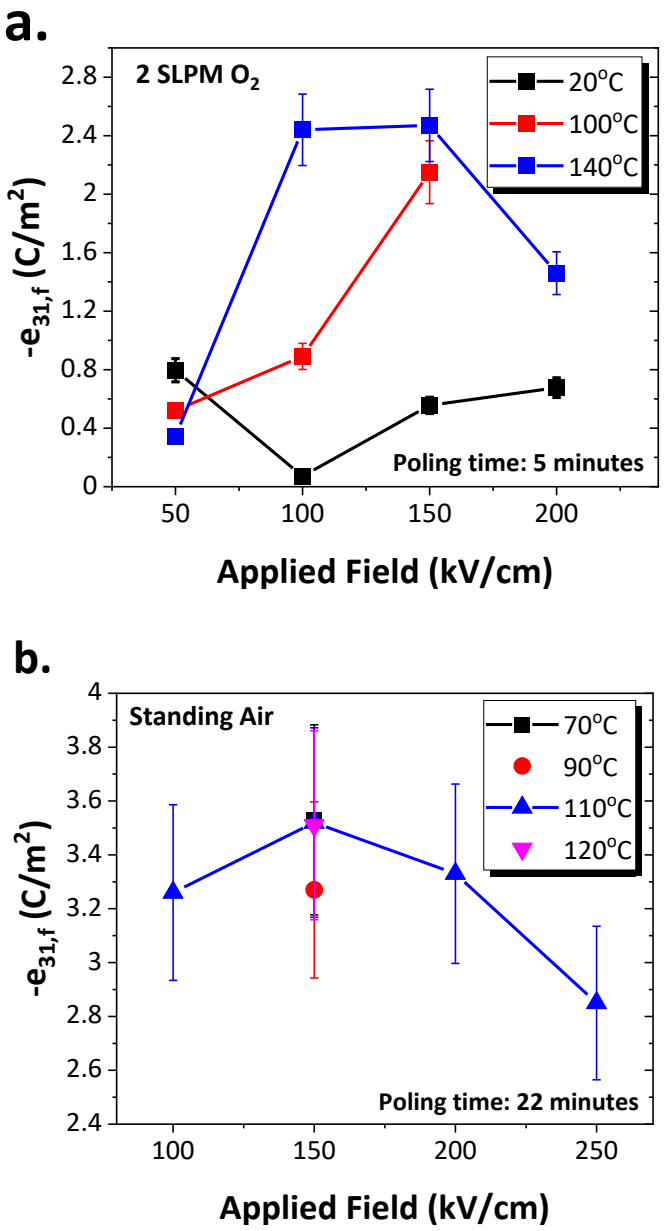

Figure **4-19**: (a) Piezoelectric $-e_{31,f}$ measurements of 1 µm thick KNN-D films following 1-step pyrolysis and annealed in 2 SLPM oxygen flow. Electrodes were poled for 5 minutes at the respective temperatures. (b) Piezoelectric $-e_{31,f}$ measurements of 1 µm thick KNN-D films following 1-step pyrolysis and annealed in standing air. Electrodes were poled for 20 to 22 minutes at the respective temperatures.

In summary, alkali homogeneity and stoichiometry have a strong influence on electrical properties such as breakdown field. Film microstructure does not affect the breakdown field as much as homogeneity and film stoichiometry. To favor (100) orientation, columnar growth from the substrate is important. These properties have been achieved separately. Modifications to the KNN-A or C method may produce a KNN film with high breakdown strength, high density, and columnar microstructure, such as KNN-D has shown.

Chapter 5

Nucleation and Growth Characteristics of KNN Thin Films

5.1 Introduction

This chapter presents a study on the nucleation and growth behavior in KNN thin films. Isothermal anneals were performed in a rapid thermal annealer (RTA) at temperatures near and above the perovskite crystallization temperature. Hold times were chosen to observe the progression of nucleation and growth from early stages of perovskite formation. KNN-C was used for this study because it delayed hydrolysis in solution, thus minimizing the chances of particle formation prior to deposition and changes in solution viscosity within the syringe throughout the deposition process. Comparisons were made to solution A to help determine what characteristics are associated with high breakdown strength. Energy dispersive spectroscopy (EDS) spatial composition maps were used to qualitatively assess film homogeneity and resolve data on secondary phases. The second part of this chapter discusses the activation energies for CSD KNN, which have not yet been reported.

5.2 Composition Segregation in CSD (K,Na)NbO_3 Thin Films

Single-layer films deposited from solution C were approximately 40 nm thick upon annealing between 500°C and 750°C (see Figure 5-1). Crystallization occurred via formation of rosettes that were distributed in an amorphous matrix for low crystallization temperatures. For higher crystallization temperatures, the nucleation rate rose to a point at which individual rosettes could not be discerned.

In the early stages of crystallization, the rosette centers appeared thinner than the surrounding film. This is confirmed by FESEM cross-section images and backscatter electron images showing more electrons scattered from the Pt top electrode, as shown in Figure 5-2. This feature disappeared towards the end of the crystallization process.

Niobium distribution was homogeneous on all film surfaces. Sodium and potassium segregation was observed. Excess sodium acetate precipitated on the film surface at processing temperatures below 300°C (see Figure 5-3). The presence of acetate below 300°C was confirmed by TGA-MS and FTIR (see Appendix). This is likely due to the inability of the excess sodium to

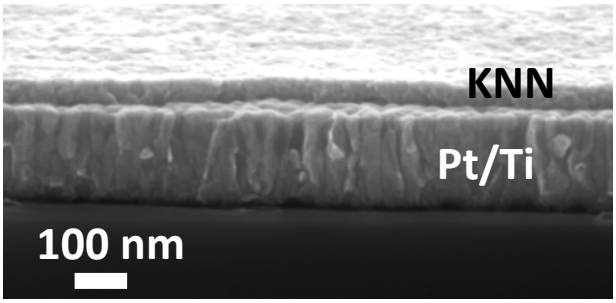

Figure **5-1**: Crystalline rosettes in KNN-C are approximately 40 nm thick.

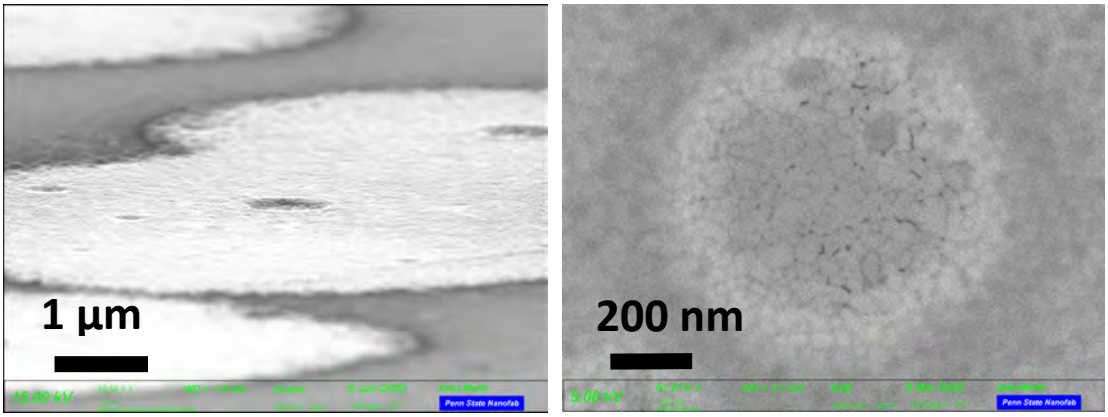

Figure **5-2**: FESEM secondary electron (left) and backscatter electron (right) micrographs of KNN-C annealed at 550°C for 28s revealing a region of reduced film thickness at rosette cores.

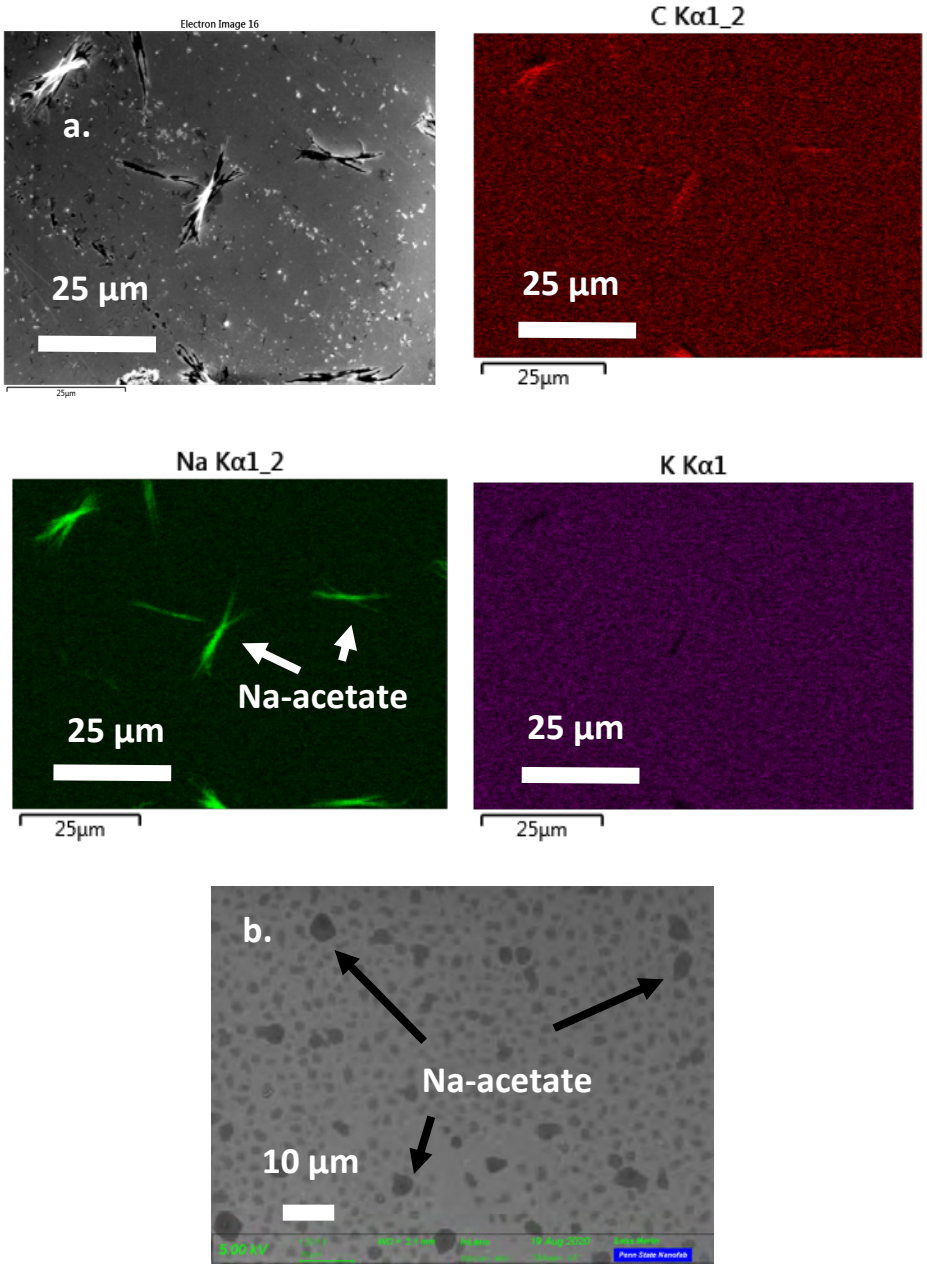

Figure **5-3**: (a.) EDS spatial composition maps showing segregation of sodium acetate after drying KNN-C at 250°C and left in ambient atmosphere. The bottom micrograph (b.) is of KNN-A only subjected to drying for 2 minutes. The dark sports are believe to be sodium acetate that has not yet migrated across the surface to form larger structures seen in (a.). Sodium acetate was confirmed to exist by FTIR in films dried at 250°C (c.f. Figure 5-8).

react with niobium ethoxide and form an oligomer in solution. Although both sodium and potassium excess were added to the solution, potassium, the more reactive ion, preferentially reacted to form oligomers with niobium species in solution and during gelation due to its higher reactivity. As reported elsewhere, NaO^- volatizes at lower temperatures than KO^- in thermal analysis of CSD KNN, despite the higher reactivity of the K^+ ion [60]. In addition, although less Na-acetate excess is added than K-acetate, mostly Na-acetate is observed as precipitates on dried films (see Figure 5-3). It is hypothesized that this occurs because Na that is not able to react with Nb is expelled as its acetate to the surface of the film, and this Na-acetate likely decomposes and is detected in the EGA at a lower temperature than potassium.

The formation enthalpy of potassium niobate (-207 kJ/mol) is more exothermic than sodium niobate (-142 kJ/mol), so it is expected to form preferably in the absence of other reactions [116]. However, the diffusion coefficient for Na through Nb_2O_5 is approximately an order of magnitude higher than that for K [52], and it is possible there may be a similar occurrence in the amorphous matrix prior to crystallization. In addition, regions of excess sodium on film surfaces after pyrolysis increased the local concentration of A-site atoms and promoted nucleation and growth of a sodium-rich KNN composition in the form of cylindrical rosettes. It is hypothesized that since the growth is controlled by diffusion of adatoms to the perimeter of rosettes[81], sodium is kinetically favored to incorporate in the perovsite structure than potassium and leads to the formation of sodium-rich rosettes at the onset of crystallization.

As shown in Fig. 5-4, EDS mapping revealed the formation of sodium rich rosettes at the onset of growth. Immediately after drying the film is covered with dark spots in the FESEM images that were believed to be excess sodium acetate. The presence of sodium acetate was confirmed by FTIR (Figure 5-8), EDS (Figure 5-3a,b), and TGA-MS (Figure 4-2, 4-3). It is believed that if the film is left in atmosphere after the drying step, acetates migrate across the film surface and result in the acetates observed in Figure 5-3a(c.f. Figure 5-8). FESEM micrographs of

films taken shortly after the drying step (Figure 5-3b) show the acetate more evenly dispersed over the surface of the film. These segregated regions of sodium acetate (Figure 5-3b) disappear under high beam currents and cannot be observed by EDS. At temperatures of 300°C and above the acetate peak completely disappears from FTIR spectra, and carbonate and oxalate peaks appear, as they are the final and intermediate decomposition products of sodium and potassium acetates, respectively [17].

In some KNN-C deposition and processing conditions, a ring of potassium-rich material appeared at the rosette edge, as shown in Figure 5-4. For films from KNN-A, the ring was more

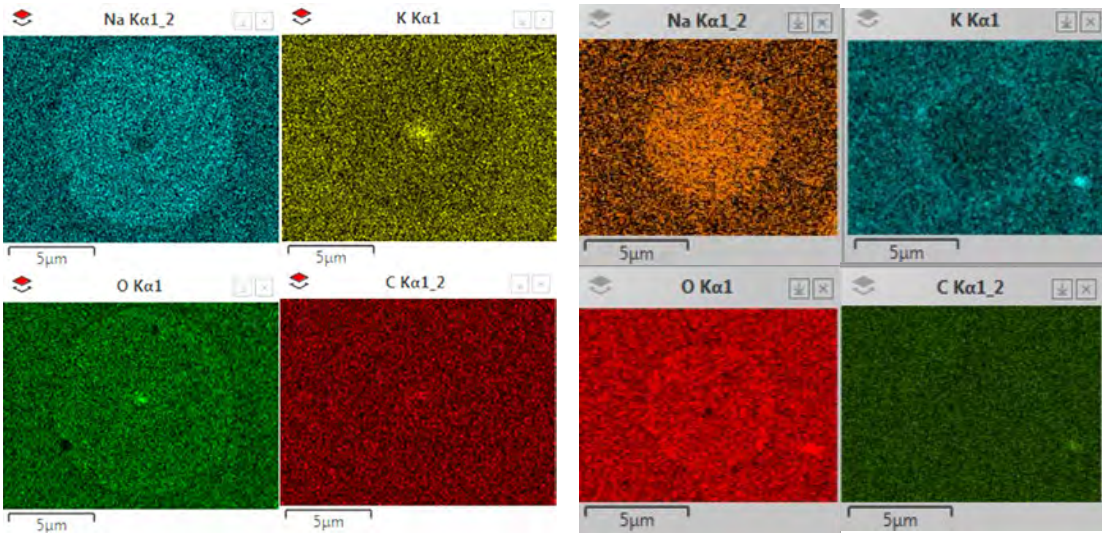

Figure **5-4**: Energy dispersive spectroscopy maps of rosettes in single-layer KNN-C annealed at 550°C for 16 seconds (left) and for 28 seconds (right). Rosettes formed were rich in sodium. Rings of carbon, potassium, and oxygen were formed at rosette edges as the anneals progressed.

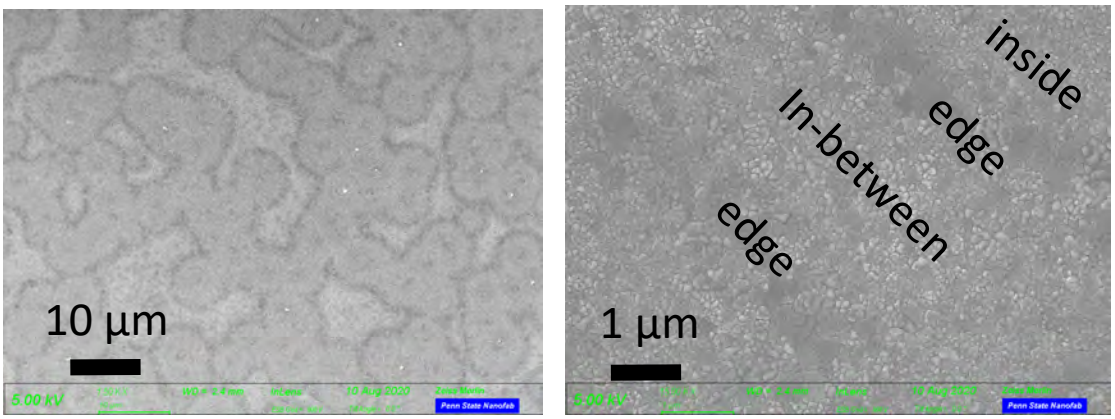

Figure **5-5**: Rosettes are apparent after 5 layers of KNN-C with 10% ex. K and 5% ex. Na crystallized at 750°C for 1 minute. The image on the right illustrates the grain microstructure relative to the rosettes (i.e. inside = inside rosette; edge = edge of rosette, etc.).

evident after 2-step pyrolysis than after 1-step pyrolysis. Reducing the potassium excess from 10% to 5% for KNN-C films prevented the formation of K-rich rings around the rosette for both 1 and 2-step pyrolysis. Processing conditions which favored the formation of this ring resulted in less insulating films and larger grains. This correlates with the observation of degraded electrical properties.

In a fully crystallized film annealed at 750°C for 1 minute (KNN-C with 10% ex. K and 5% ex. Na, 2-step pyrolysis and 5 layers of deposition), large grains and visible rings exist in the same area. At the edges of the rosettes, there are potassium-rich rings and larger, elongated grains with smooth surfaces. Inside the sodium-rich rosettes, smaller and coarser grains appear; a mixture of large and small grains appears in the area in-between the rosettes, as shown in Figure 5-5. It is hypothesized that large grains exist where the rings were because excess A-site atoms segregate there and speed the kinetics for growth. Annealing for up to 5 minutes did not resolve the composition inhomogeneity in the films.

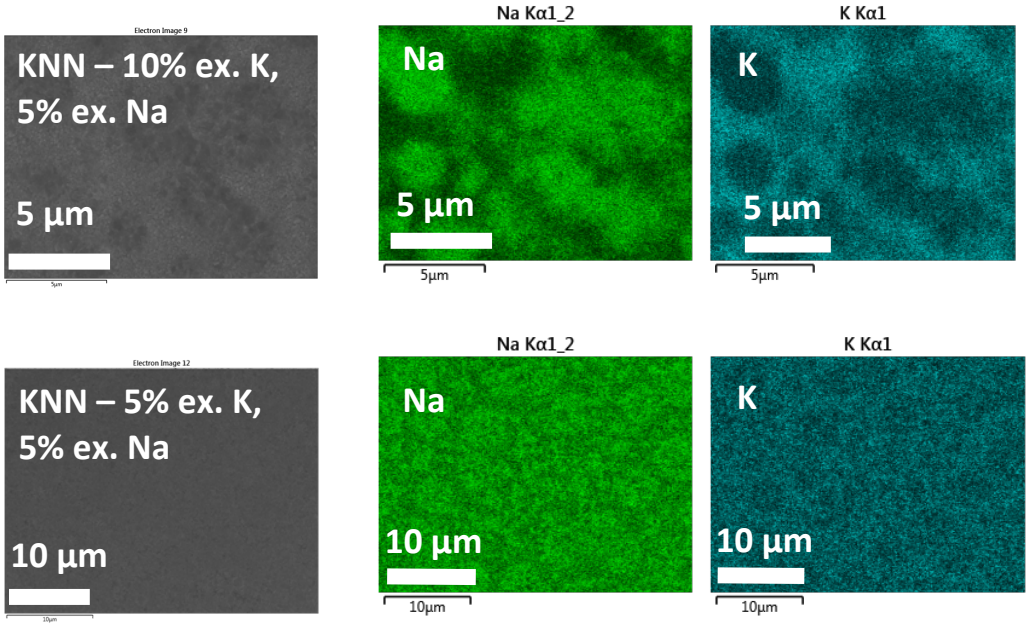

Figure **5-6**: 5-layer KNN-C films with 10% ex. K (top) and 5% ex. K (bottom) annealed at 750°C for 5 minutes per layer. Note the difference in scale.

After reducing the potassium excess in the solution to 5%, ring structures were not apparent in the microstructures. There was a reduced contrast between sodium rich and deficient regions attributed to less composition segregation, as shown in Figure 5-6.

It was found using the MATLAB Image Segmenter App that approximately 60 to 65% of the surface is lighter in contrast than the remainder of the film (c.f. Figure 5-5). This suggests that 60% of the film nucleates and grows with a sodium-rich composition. The literature suggests that interdiffusion between sodium and potassium through niobium oxide may correct composition segregation during longer anneals [52], but that was not observed in the case of CSD KNN thin films with anneal times up to 5 minutes at 750°C. It may be interesting to see if a post anneal can resolve the spatial composition inhomogeneity CSD KNN thin films.

Secondary phases with potassium generally appeared late along the nucleation and growth time coordinate. Elongated rod structures, sometimes with curvature, and with lengths

above tens of microns were observed; these contained potassium, carbon, oxygen, and sometimes sodium. This was confirmed through EDS and can be seen in Figure 5-7. It is unknown which compound this is. It is speculated that this might be an intermediate oxalate.

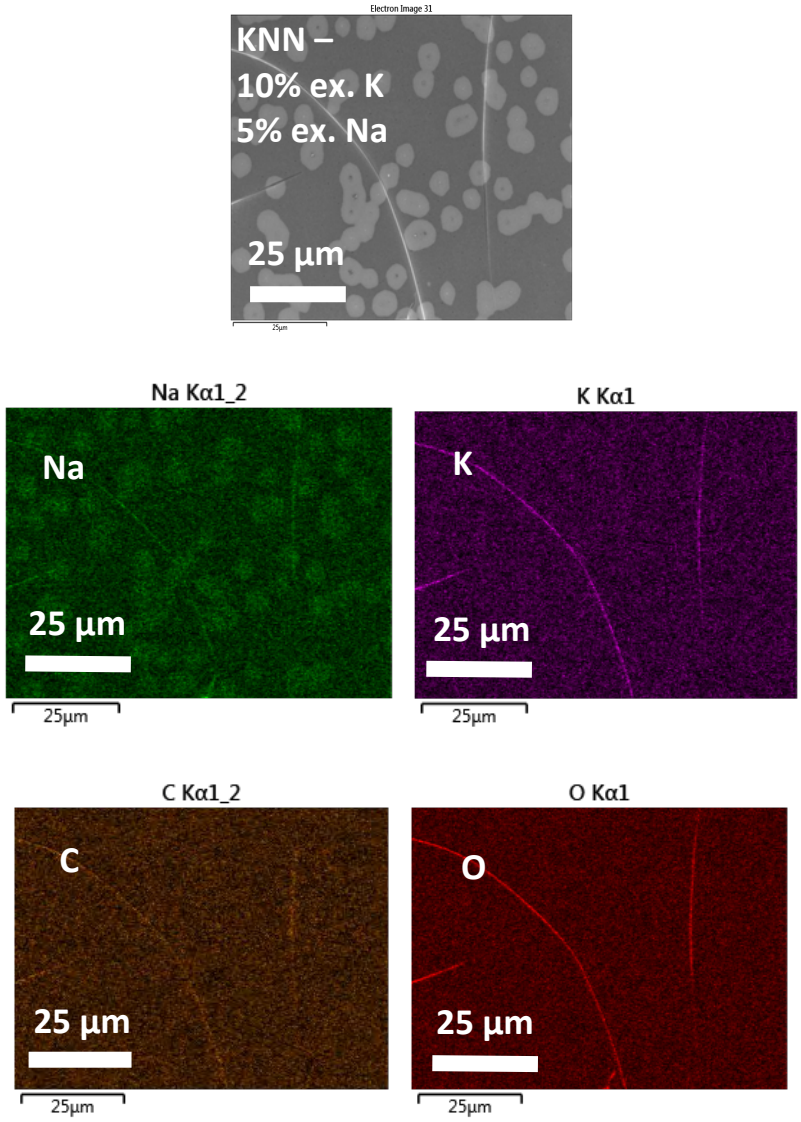

Figure **5-7**: Rod structures containing potassium, sodium, oxygen, and carbon are likely the intermediate oxalate salt prior to decomposition. This sample was annealed at 550°C for 28 seconds, after 1-step pyrolysis at 300°C for 3 minutes.

Fourier Transform Infrared Spectroscopy (FTIR) was performed to discern phases present in KNN thin films. When the film was dried at 200°C, an acetate peak was detected around 1450 cm^{-1}, as shown in Figure 4-6. The acetate peak disappeared after crystallization as shown in Figure 4-6 and Figure 5-8. In partially crystalline films, the carbonate peak which appears after annealing at 525°C for 10 seconds near1474 cm^{-1} disappears by 25 seconds. This suggests a rapid decomposition of the (more likely) sodium oxalates which have a lower decomposition temperature than potassium oxalate [101,102]. Recall that the decomposition pathway for alkali acetates are acetate → oxalate → carbonate [17]. The remaining oxalates at 40s are a mixture of sodium and potassium oxalates. As the anneal progressed, the Nb-O peak

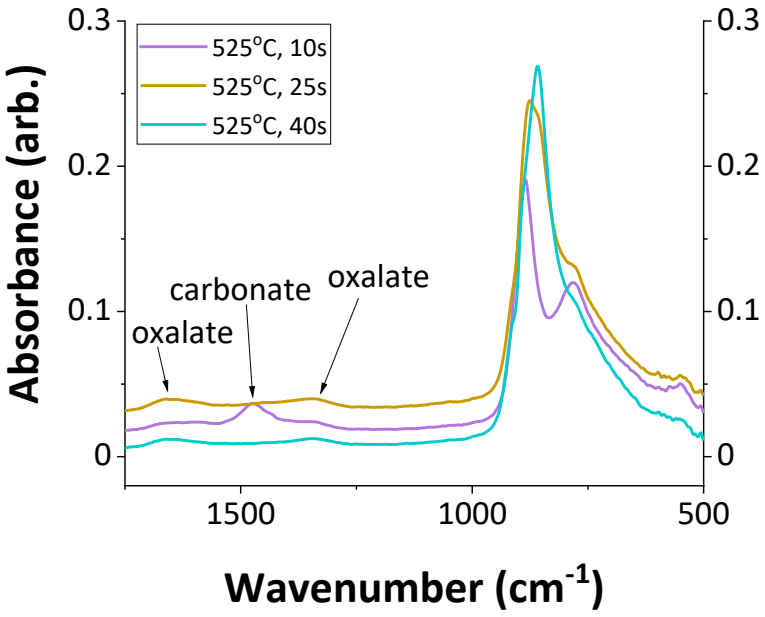

Figure **5-8**: FTIR spectra for dried (c.f. Figure 5.3) and partially crystalline KNN-C annealed in standing air (c.f. Figure 5-11).

near 870 cm^{-1} increases in intensity and shifts to a lower wavenumber. A similar trend was observed for the Nb-O peak in samples annealed at 500°C.

In addition to the intermediate oxalate species, another source of carbon was retained organics due to the addition of acetylacetone to the solutions [19, 32]. The presence of organic phases in thin films can delay crystallization; their decomposition is necessary to crystallize the perovskite phase [20]. As of now it is unknown whether catalytic activity of amorphous niobium oxide affects the formation or decomposition of metalorganic species such as the alkali oxalates.

It is speculated that the nucleation and growth behavior in KNN-C is influenced by the niobium ethoxide precursor. The reaction of niobium ethoxide with 2-methoxyethanol produces monomeric species in solution, rather than oligomers [16]. The formation of oligomers upon gelation, which are molecules with repeating units with other metals, is dependent on the extent of exchange between the ethyl and methoxyethyl groups from the solvent in the solution. Excess solvent can hinder the formation of oligomers upon gelation, ultimately reducing film homogeneity [16]. It is possible that the large amounts of acetic anhydride introduced to solution C further hindered the formation of oligomers.

This problem can be solved by driving the reaction of Nb-ethoxide with 2-methoxyethanol to near completion before other precursors are added to the system [20]. Refluxing for extended times at 130-150°C with organic esters of acetic acid produced nearly complete exchange interactions between the ethyl group on Nb-ethoxide and its respective solvent [117]. The introduction of acetylacetone can drive the reaction between ethyl groups and methoxyethyl groups, but the acetylacetone groups remain bound to niobium, and are difficult to pyrolyze [16].

Niobium ethoxide is dimeric in nature, so it is already coordinated with one Nb through a Nb-O-Nb linkage. However, the ethoxide groups must be replaced with 2-methoxyethoxide groups to encourage homogeneity [16]. The coordination with other Nb atoms increases to 2.5

when fully hydrolyzed [118]. The hydrolyzed Nb is reported to have corner sharing polyhedra with other Nb and a porous structure where other ions can situate prior to densifying heat treatments (Figure 5-9).

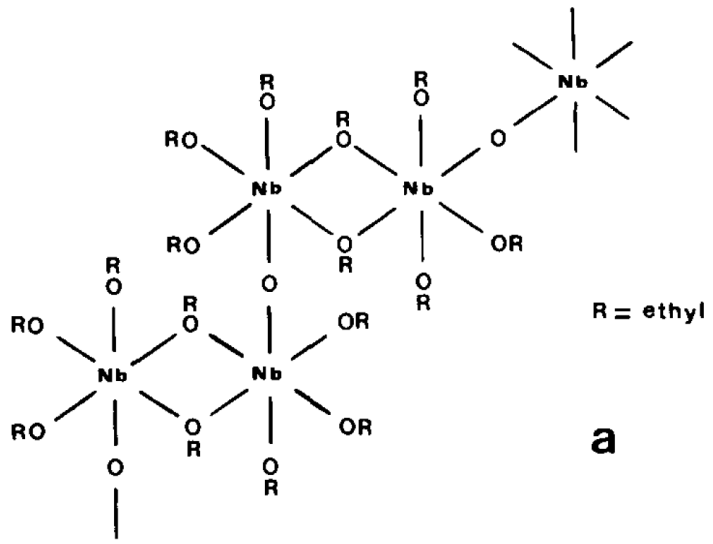

Figure **5-9**: A 2-D sketch of the final product of gelled niobium ethoxide. From reference [118].

5.3 An Activation Energy Study on CSD KNN

5.3.1 Background

An in-depth study on the activation energy for KNN thin films deposited via the sol-gel method has not yet been reported. Kwok and Desu [85] report results for sputtered PZT films annealed in a tube furnace. However, rapid thermal anneals allow a narrow window of time to observe the early stages of nucleation and growth. Therefore, in this study, films were deposited and annealed within a narrow time window to mitigate changes in the solution conditions, which affect the nucleation density [17]. All samples were deposited and annealed following the procedure for solution C in the Solution Deposition and Heat Treatment section (3.2) in the Experimental chapter, followed by a rapid thermal anneal at 500, 525, or 550°C. All samples were deposited within 105 minutes. FESEM images were taken 1 day after deposition.

Deposited layers were approximately 40 nm thick (see Figure 5-1). Perovskite KNN crystallites were on the order of 15 nm upon formation at the rosette perimeters. At the center of the rosettes, grains grew to over 100 nm in dimension after longer annealing times.

5.3.2 Approach

The activation energies for nucleation and growth pertains to the kinetic processes involved in crystallization. Here, the Johnson-Mehl-Avrami-Kalmogorov (JMAK) model [81,82,83,84] was used to describe crystallization kinetics. JMAK kinetics applies to polyhedral growth where growth is uniform in all directions [81,82,83]. There are a number of key assumptions that should be satisfied to apply JMAK kindetics. First, nucleation is presumed to be randomly distributed [83]. Secondly, growth of circular rosettes should change to needle-like

growth as the transformation curve flattens [83]. Thirdly, there should be nucleation events producing rosettes all approximately the same size, followed by later events where other nuclei begin to grow [83]. Fourthly, the growth rate should not decrease with time, such that a nuclei activated in a later nucleation event grows larger than or overtakes a nuclei which became active earlier [82]. Thus, there should be "layers" of crystallized rosettes or grains where each layer consists of a unimodal distribution of rosette sizes [81]. All of these conditions are satisfied early in the crystallization process for this study. The later stages of growth where the transformation curve flattens were not studied here, so there was no observation of a transition to needle-like growth for the perovskite phase. Since the rest of these conditions were satisfied, the random surface assumption is applied [83,85]. It was also assumed that only nucleation and growth contribute to the total perovskite transformation activation energy [81,82,83,84].

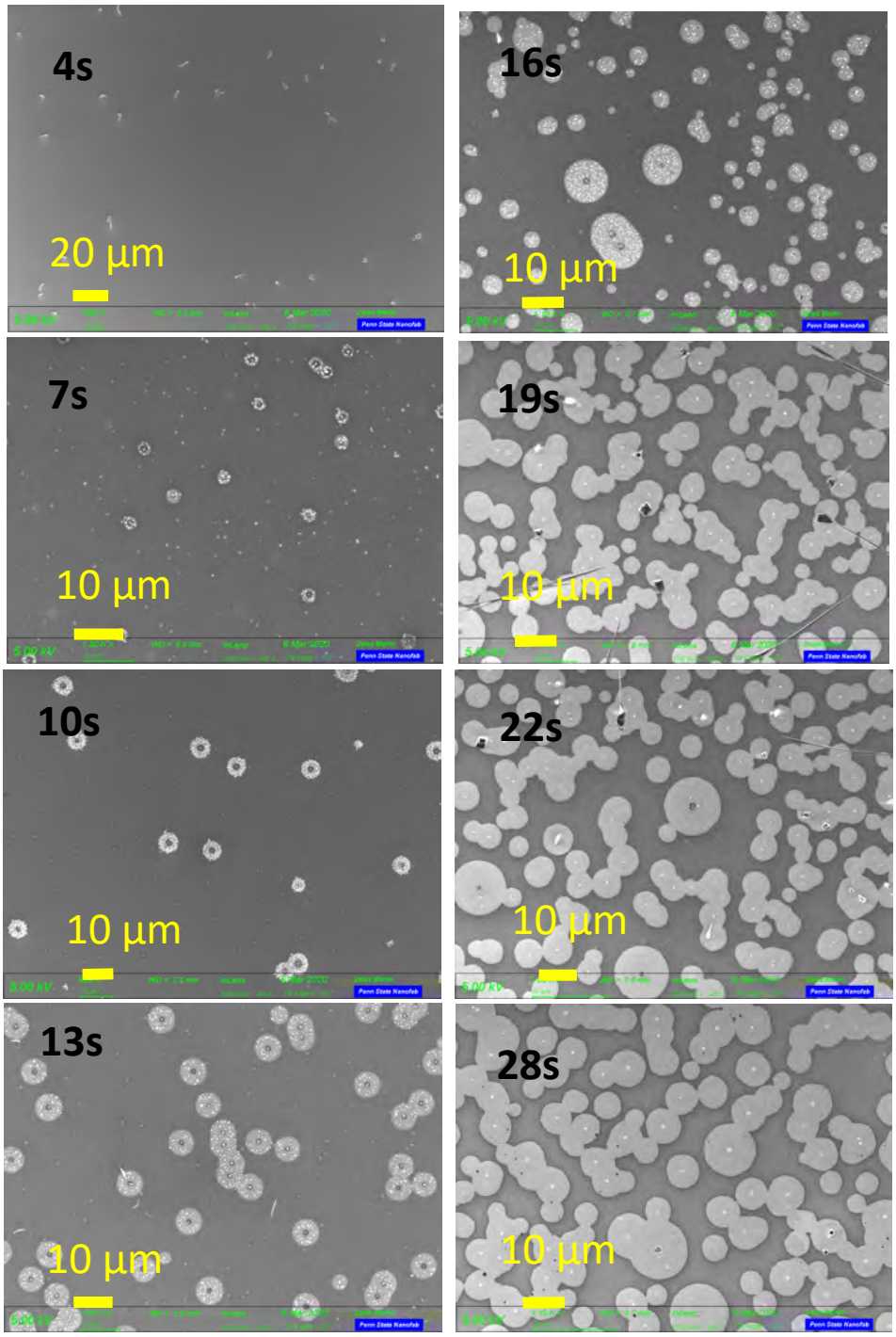

Figure **5-10**: FESEM micrographs of KNN-C films annealed at 550°C for the specified times in a rapid thermal annealer.

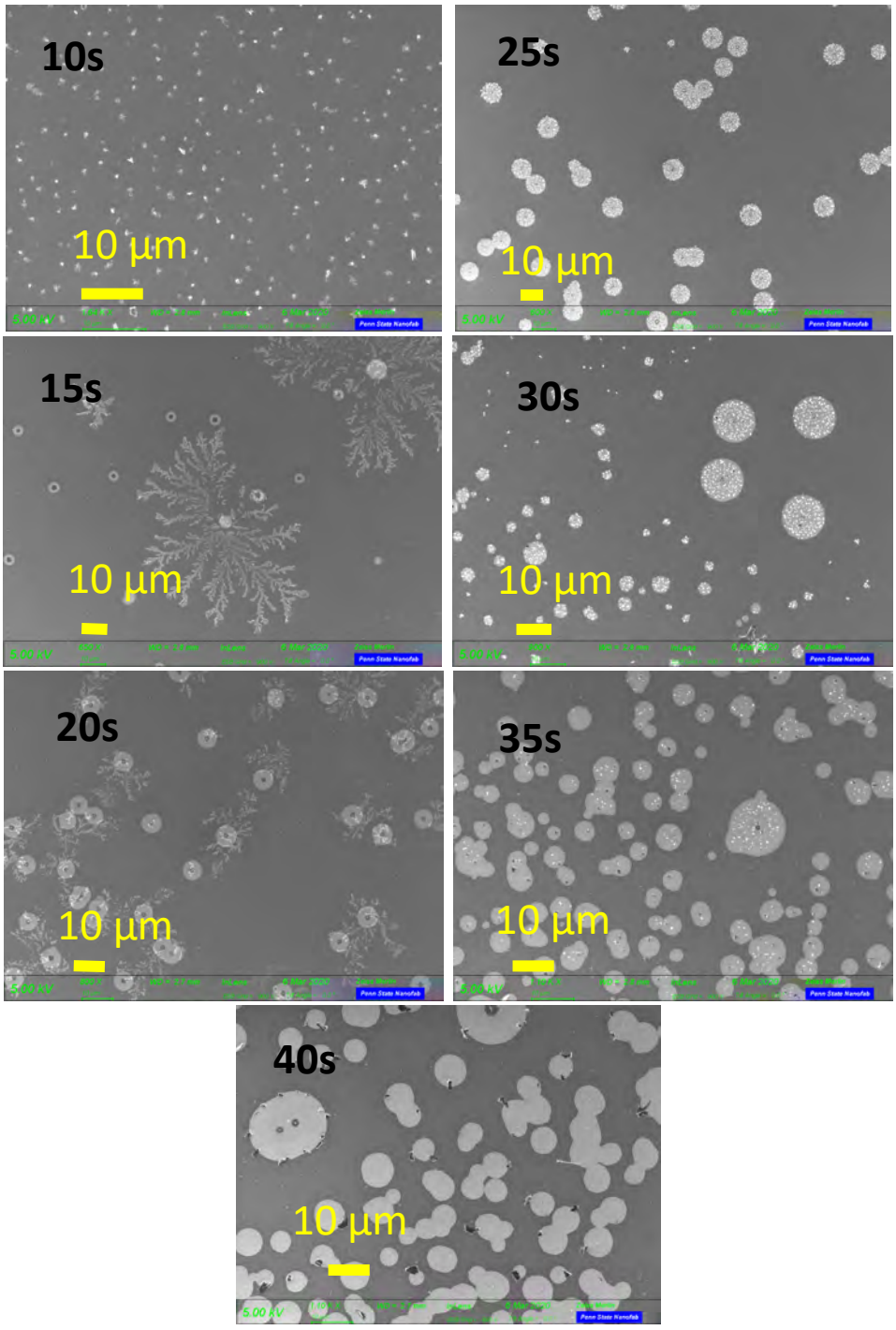

Figure **5-11**: FESEM micrographs of KNN-C films annealed at 525°C for the specified times in a rapid thermal annealer.

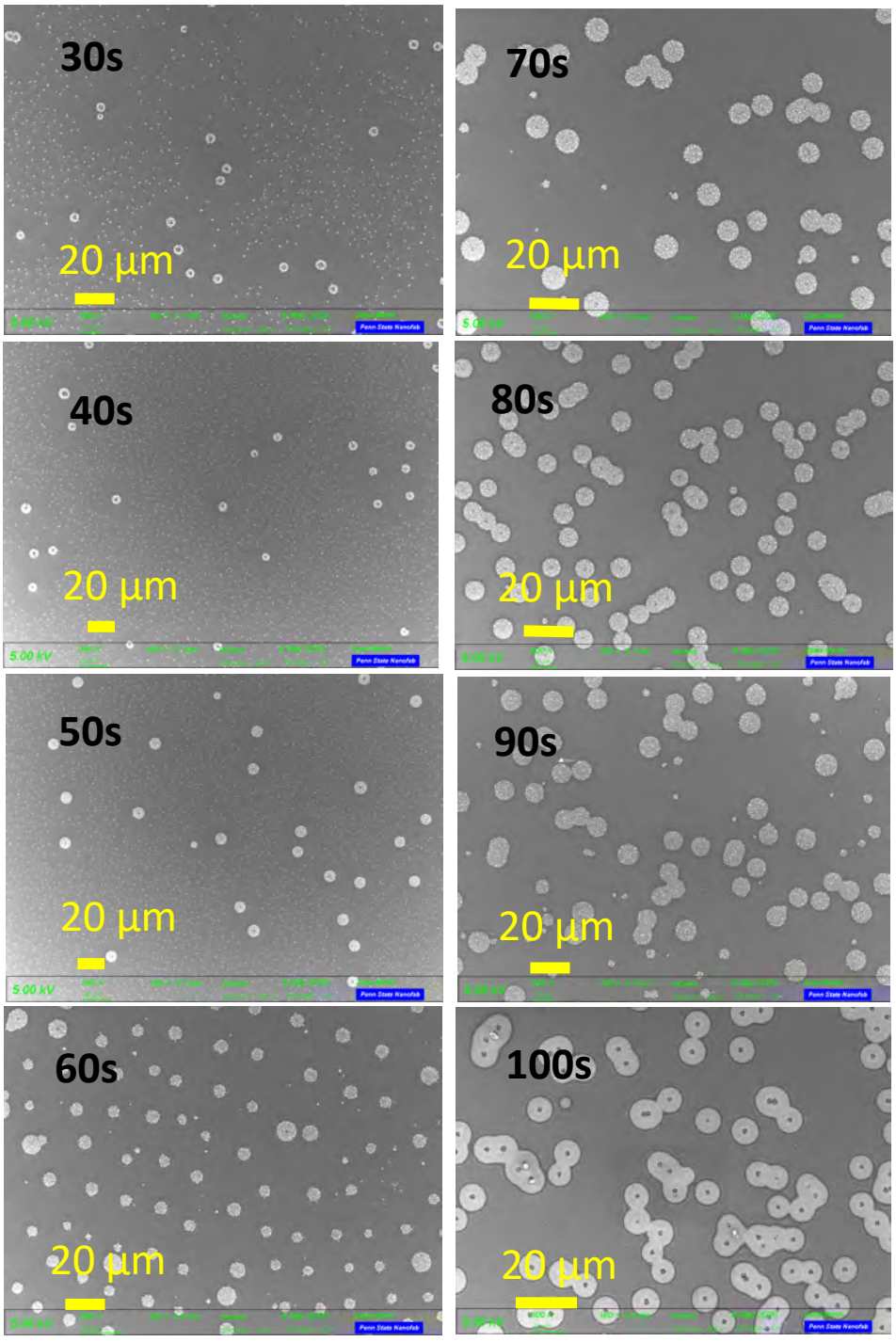

Figure **5-12**: FESEM micrographs of KNN-C films annealed at 500°C for the specified times in a rapid thermal annealer.

5.3.3 Growth

The activation energy for growth, the difference between adsorption and desorption energies for adatoms [119], was calculated from early stages of rosette growth before extensive soft impingement and coalescence. Rosettes grow radially outward as a disk, where the rate of the reaction is proportional to the number of sites on the rosette perimeter [81]. Calculations of the activation energy involved data from 500°C, 525°C, and 550°C (see Figures 5-10, 11, 12, 13). Each of the data sets captured the first nucleation event. After a nuclei is activated, it goes through a phase of slow growth, followed by a constant growth rate [83]; this is consistent with the description of growth provided by Johnson and Mehl [84]. The incubation period is ignored when observing the growth rate. More detailed description of the parameters for measuring the growth rate and calculating the activation energy are in sections 2.15 and 3.12.

The goodness of fit exceeded 0.98 on all regression lines for growth in Figure 5-13. Rate law values n were 1.40 ± 0.11, 1.32 ± 0.08, and 1.10 ± 0.08 for 550°C, 525°C, and 500°C respectively. A n value of 1 indicates interface-controlled growth with a transfer of atoms across the circumference (interface) of the rosette [81]. Rate law values greater than 1 indicate an increase in the dimensionality of growth or rapid film growth, likely due to excess alkali precursors added to the solution. In addition, the presence of dendrites on the film indicate rapid crystal growth and a rate law $n > 1$ (see Figure 5-11) [120]. The activation energy for perovskite growth is calculated to 194 ± 10 kJ/mol. The error was from the linear regression on the Arrhenius plot, as seen in Figure 5-13.

Of an interesting note, sodium oxalate decomposes at measurable rates over transition metal oxides at temperatures between 510°C and 530°C, and decomposes rapidly at higher temperatures [101]. However, the onset of decomposition of potassium oxalate is at 540°C and it

does not decompose at an appreciable rate until higher temperatures [102]. The activation energy for growth of sodium-rich KNN rosettes is similar to that for the decomposition of sodium

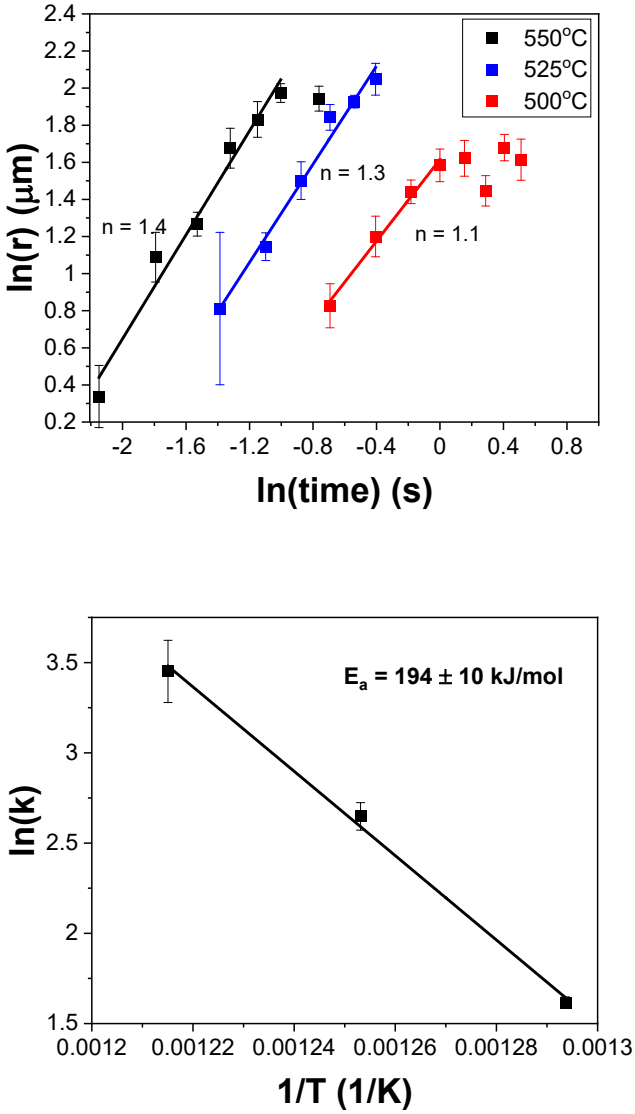

Figure **5-13**: Rosette radius (r) vs. anneal time for the first nucleation event for perovskite KNN rosettes (top). The Arrhenius plot of the activation energy for growth (bottom).

oxalate, where the two activation energies measured for Na-oxalate decomposition were 156 kJ/mol and 197 kJ/mol, for the accelerator and decelerator stages respectively [101]. However,

the activation energy for oxalate decomposition is not expected to affect those for KNN according to Avrami's key assumptions stated in his paper published in 1939 [82]. It is expected that the decomposition of sodium oxalate provides an excess of alkali cations to react at the rosette perimeters for growth. In this case an increased concentration of reactants will not change the activation energy, but will change the time scale of the reaction, or the rate law. This is the reason for observing rate rate laws higher than the theoretical maximum for growth and perovskite transformation seen in Figures 5-13 and 5-14. The activation energy for growth is the difference between the activation energy for adsorption and desorption of adatoms at the rosette perimeter [119], and a change in the concentration of adatoms will change the rate [81]. For example, less excess sodium will require longer anneal times to yield results having the same activation energy.

5.3.4 Perovskite Transformation

The perovskite transformation energy was calculated by measuring the volume fraction crystallized (see Figure 5-14). Rosettes were assumed to be perfect cylinders through the thickness of the film, so only the surface area of the rosettes were measured.

Over multiple trials, growth nearly stopped around 60 vol% crystallized for 525°C and 550°C; no clear tail was found for 500°C, and no volume fraction crystallized over 30% was recorded at that temperature. It remains unclear why crystallization saturated at a lower fraction at 500°C. One hypothesis is that reactant depletion increased the time scale, τ, of the crystallization reaction [85] so the kinetics were delayed. Therefore, short anneal times were used in this study. The rate law exponents were 3.80 ± 0.77, 2.79 ± 1.18, and 3.53 ± 0.30 for 550°C, 525°C, and 500°C respectively. The maximum theoretical rate law is 3 for phase transformation in a thin

film. Hence, similar to growth, higher-than-normal rate laws may indicate rapid crystallization due to excess alkalis [81].

The pattern of deviations from linearity in the $\ln(\ln(\frac{1}{1-x}))$ plot for 500°C, shown in Figure 5-14, are probably due to randomness in the nucleation rate. The last two points taken from the

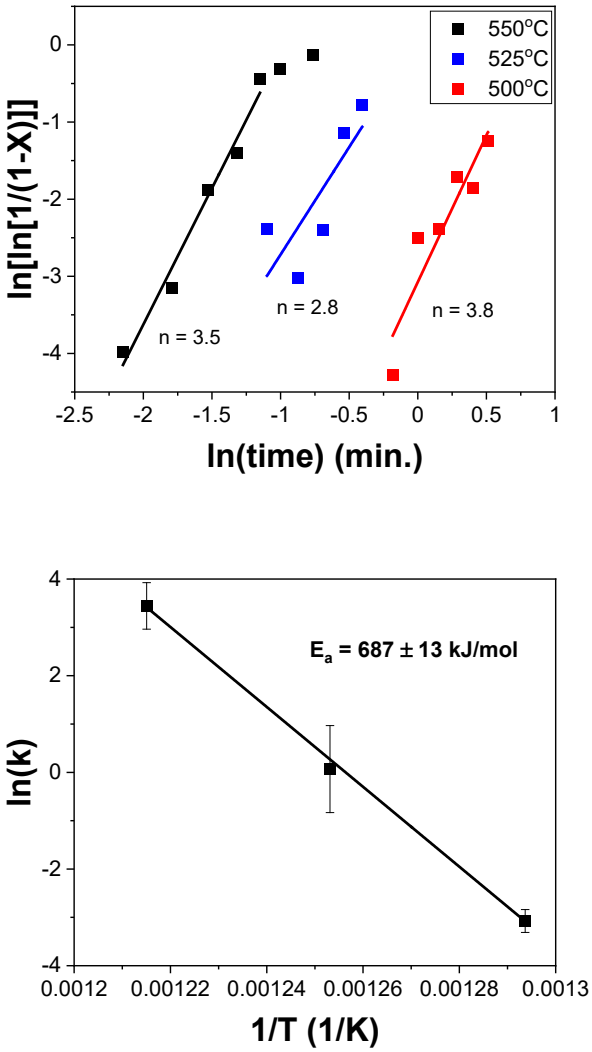

Figure **5-14**: $\ln(\ln(\frac{1}{1-x}))$ vs. ln(anneal time) for the first nucleation event for perovskite KNN rosettes (top). The Arrhenius plot of activation energy for perovskite formation (bottom).

temperature 550°C data set were not included due to the characteristic "fall off" of experimental

points as the JMAK curve begins to flatten [81]. The activation energy for total perovskite transformation was calculated to 687 ± 13 kJ/mol. The coefficient of determination, which describes the goodness of fit, for the Arrhenius plot of the total perovskite transformation was > 0.998 with all the included points. The large activation energy for perovskite growth compared to relatively small activation energies measured for growth emphasize the nucleation dominated crystallization kinetics of KNN thin films from this CSD route.

5.3.5 Nucleation

The activation energies were determined by direct observation as described in section 2.15. Two activation energies for nucleation from the average nucleation rate and the maximum apparent nucleation rate were calculated. Variances in the nucleation density between samples made calculating the activation energy difficult; these variances were due to either randomness of nucleation or experimental error, such as errors caused by small delays when removing the

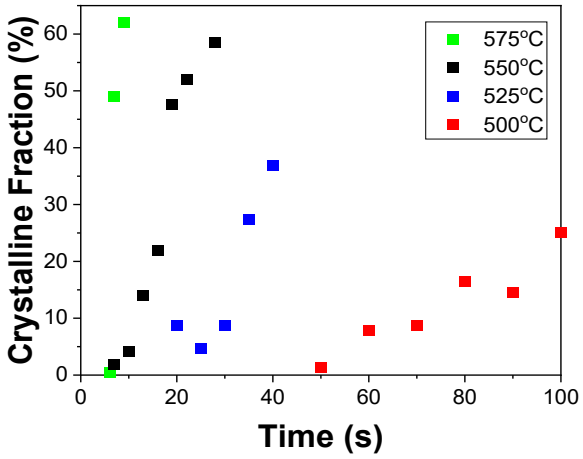

Figure **5-15**: Crystallization progression by volume fraction for temperatures 500°C through 575°C.

sample from the RTP. At 500°C, 525°C, and 550°C the nucleation rates were calculated from the four shortest viable anneal times. At longer anneal times, the coalescence of the rosettes made it difficult to count the number of active or growing nuclei. JMAK kinetics describes a constant nucleation rate where all "phantom" nuclei must be counted as well (c.f. Figure 2-19) [81,83]. Since the apparent nucleation rate was not constant in this study, it was difficult to determine an activation energy for nucleation by direct observation and counting the nucleation densities. It was impossible to perform this experiment at temperatures above 550°C due to the rapid saturation of the crystallized volume to 60%, shown in Figure 5-15.

The nucleation rate was measured by taking the slope between two nucleation densities. Some of the nucleation rates captured are negative due to a lower nucleation density measured at the next time step. The lower nucleation density is not a factor of human error, but of the randomness of nucleation. The fluctuations in nucleation rate (Figure 5-16) are reflected in the total perovskite trasformation (Figure 5-15). For example, an apparently negative nucleation rate between 80 and 90 s at 500°C resulted in a decrease in the total crystalline volume fraction observed at 90s, relative to 80s (see Figures 5-15 and 5-16). Deviations from a consistent increase in nucleation density may be due to the randomness of nucleation. The model provided for crystallization kinetics is a probability estimation [81], so fluctuations like this were not excluded from calculations as outliers. A falling nucleation rate over time was reported by Kwok and Desu due to the decreasing concentration of reactants in the amorphous phase, and "soft impingement" [85] where reactant depletion near a rosette delayed the crystallization kinetics within that region. Negative nucleation rates were not reported by Kwok and Desu [85]. Johnson and Mehl state that a constant nucleation rate [84] exists; this was neither observed in this work nor by Kwok and Desu [97]. Therefore, the calculations from this method can only be a rough approximation, and should not be taken as an accurate activation energy.

According to Johnson and Mehl, the nucleation density should always increase with time, however the growth of activated nuclei overtakes germs and smaller nuclei within the crystallized volume [82,83]. This reduces the observable nuclei as anneaingl time progresses. In other words, multiple "layers" of nucleation events coexist on the film, but the first "layers" partially cover the later "layers," so they cannot be observed. Therefore, the actual nucleation rate cannot be observed. Avrami [83] describes a process in which the germs are overtaken by growing nuclei,

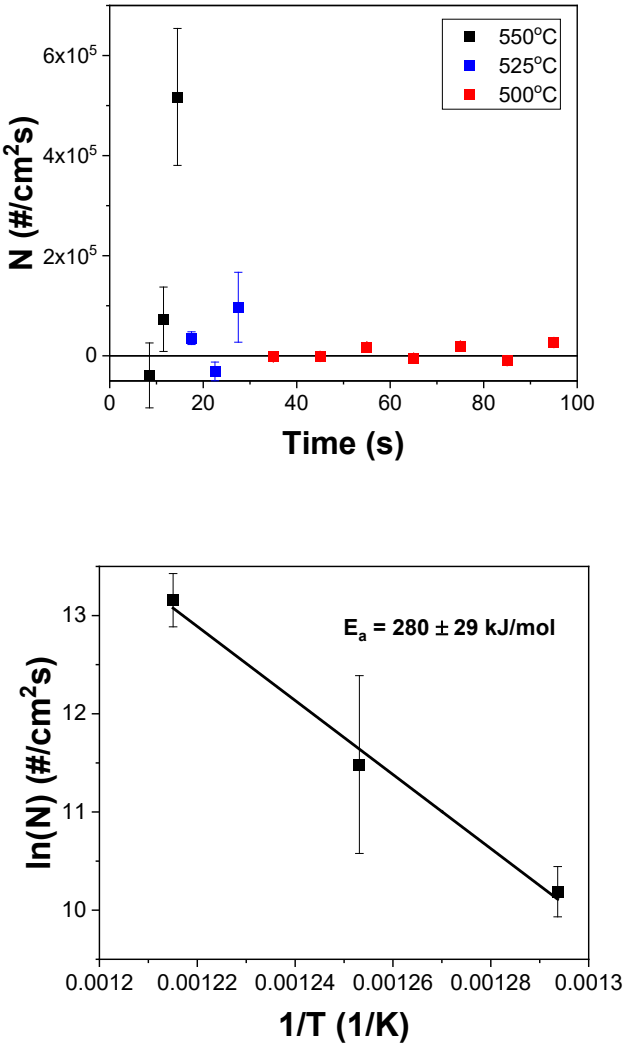

Figure **5-16**: Nucleation rate vs. anneal time for perovskite KNN rosettes (top). The Arrhenius plot of the activation energy for growth (bottom).

act as “phantom” germs or grains. Calculating the activation energy from the nucleation rate requires information from all the “layers”. The phantom grains are not accounted for in activation energy calculation, but are accounted for in the total perovskite transformation energy [83].

FESEM backscatter images suggest the existence of phantom grains in KNN, since the KNN film appears thinner at the center of the nuclei where each germ was located (see Figure 5-17). These appear as lighter-colored spots on backscatter electron images since in this case more electrons will scatter from the platinum substrate which has a higher atomic mass than the elements in KNN. Germ nuclei which have become active do not grow appreciably until an incubation time passes [81,83]. During this time the active nuclei can be overtaken by a growing rosette and become undetectable on secondary electron images. The contrast on electron backscatter images due to the higher Z number of Pt, which is directly below the KNN film, may indicate active nuclei which have not grown yet, since perturbation in the thickness of the KNN layer are otherwise not expected. This phenomenon is responsible for the inability to discern an accurate nucleation density by direct observation [81,85]. In addition to the inability to observe phantom grains, other events like soft impingement and high volume fraction transformed hindered the likelihood of generating accurate nucleation densities. Fro example, it is nearly impossible to determine a nucleation density via direct observation when nearly 50 vol% of the film had crystallized.

Because of fluctuation in data due to these issues, two nucleation activation energy approximations are provided, using the maximum observed nucleation rate, and the average nucleation rate for each set. Because the total perovskite transformation energy accounts for “phantom” grains [83], the most accurate activation energy for nucleation may be obtained by subtracting the growth activation energy from the total perovskite transformation activation energy.

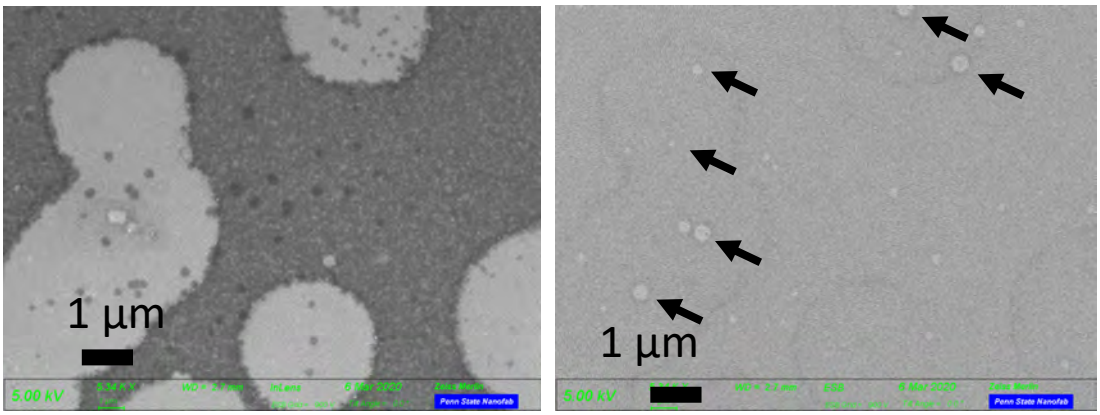

Figure **5-17**: FESEM secondary electron images (left) and BSE image (right) of the same section of film. Phantom grains which are not observable on the secondary electron image are observable on the BSE image as lighter colored dots, some of which are indicated by arrows. Nuclei in the amorphous section are hindered from growing due to "soft impingement" [85] – the depletion in the concentration of reactants near crystallized rosettes.

The goodness of fit was greater than 0.99 on the Arrhenius plots for activation energy calculated from both the maximum and average nucleation rates. The activation energy for nucleation using the maximum nucleation rate is 280 ± 29 kJ/mol. The activation energy for nucleation using the average nucleation rate is 352 ± 56 kJ/mol. Error propagation was performed to calculate the error for this activation energy (see Appendix). Two methods were used because of the difficulty in determining the actual nucleation density. The activation energy for nucleation, obtained by subtracting growth from the total perovskite formation, is 493 ± 23 kJ/mol.

5.3.6 Conclusions

In summary, the JMAK kinetic approach was used to determine the total perovskite transformation energy and the growth activation energy. The nucleation activation energy cannot

be modeled accurately by the JMAK kinetics equations in this study because of the inability to directly observe a constant nucleation rate in isothermal conditions [84]. However, because crystallization is assumed to consist of only nucleation and growth, the nucleation activation energy can be obtained from the difference between the perovskite transformation energy and the growth activation energy. It is not uncommon to have difficulty calculating the nucleation energy, as Kwok and Desu also calculated variable nucleation rates in their sputtered PZT thin films [85]. Their activation energies for nucleation and growth did not sum to the total perovskite transformation energy, albeit error bounds were not specified.

It is notable that, as in PZT, the activation energy for nucleation exceeds that of growth substantially. This suggests that nucleation will be the rate-limiting process. It also suggests that if the nucleation can be adequately controlled, it should be possible to use nucleation from the substrate only to control film orientation.

It is unclear whether the activation energy will change for KNN thin films produced by other deposition methods. If remaining organics exist in the film at the moment of crystallization, this activation energy may also account for the energy required to decompose carboxylate species from the thin film prior to crystallization [81]. This is discussed further in the future work section.

Chapter 6: Conclusions and Future Work

This work desccribes chemical solution deposition methods for ferroelectric KNN thin films. Manganese doping was found to be beneficial for maintaining low leakage currents in KNN, which ultimately allow the films to be poled for piezoelectric measurements. The KNN films presented in this work have leakage current properties comparable with the best CSD Mn-doped KNN deposited on platinized silicon, reported elsewhere [121]. It is anticipated that improved poling procedures can further increase the measured $-e_{31,f}$ coefficient beyond 5 C/m^2.

KNN-A and the modified KNN-D films showed the most promise for piezoelectric applications. They exhibited high breakdown field and decent small-signal $-e_{31,f}$ coefficients for manganese-doped KNN. Columnar KNN-C films which also had low leakage currents and high breakdown strength hold promise for producing strongly oriented KNN films. These films could be poled adequately, however they suffered from composition segregation which limited the maximum measured $-e_{31,f}$ to around 2 C/m^2. Even if the average composition is near the MPB, the large scale composition segregation observed on EDS in KNN-C suggests a sizeable portion of the film was not at the MPB stoichiometry. KNN-C films on platinized silicon substrates suffered from high tensile stress states, which would also be expected to decrease the piezoelectric response. Imprint in KNN-B and KNN-C films suggest the possible existence of aligned defect dipoles, in areas where excess alkali ions had segregated during crystallization to make the film locally alkali-rich. This defect dipole can prevent the polarization of some volume of the film, due to the difficult migration of oxygen vacancies under applied electric field [122]. Further work to reduce composition segregation is required to increase the piezoelectric response of KNN-C films.

The nucleation and growth study was beneficial for understanding how composition segregation is introduced in CSD KNN thin films. The effect of excess alkali precursors on

composition segregation was also observed. Procedures which involved the formation of a ring around the rosette were linked with abnormal grain size distributions and decreased breakdown field. Activation energies were measured for perovskite transformation (687 kJ/mol), growth (194 kJ/mol), and nucleation (493 kJ/mol). The high rate laws observed for perovskite transformation and growth suggest that concentrations of excess alkali precursors hastened the crystallization kinetics. The disparity between the activation energies for growth and nucleation indicate the crystallization of KNN is nucleation-limited, and nucleation can be favored with the choice of a seed layer to orient KNN.

Based on this work, one future experiment of great interest entails changing the precursor chemicals for CSD KNN. First, it would be possible to replace the solvent 2-methoxyethanol with the less toxic 2-butoxyethanol [17]. Niobium was found to react extensivelty with tert-butyl acetate, bringing the reaction almost to completion after refluxing for 8 hours at 130-150°C, and distilling the by-products (ethyl-acetate) intermittently [117]. Then choosing 2-butoxyethanol as the solvent will be preferable for homogeneity for $Nb(OBu^t)_5$ complexes over 2-methoxyethanol [16]. Secondly, changing to an ethoxide precursor for one of both of the alkali precursors, sodium and potassium, may help to isolate the effect of acetic acid on the solution, since it is difficult to rid the solution of acetic acid when acetate precursors are used. Acetylacetone has been beneficial for stabilizing solution, however it is interesting to speculate how the nucleation and growth behavior will change without the addition of acetylacetone to KNN solution, and if composition segregation will be more or less prevalent.

The addition of acetic anhydride to solution C at the beginning of reflux may hinder the reactions involved due the excess redundant component introduced to the solution. In hindsight, it is interesting to speculate if a columnar film can be achieved by following the solution A or D route and adding a small amount of acetic anhydride at the end of the reflux after adding acetylacetone.

Since crystallization is affected by the removal of carbon from the film, it is interesting to speculate crystallization behavior while incorporating ultraviolet irradiation or ozone during the anneal step.

The ultimate goal of a KNN thin film would be to produce a lead-free energy harvesting device, or an implantable piezoelectric medical device, such as an energy harvester for a pacemaker. In this case, the patient would be able to avoid invasive surgery to replace the pacemaker battery, and instead use the human body as an energy source [123,124]. Lead-free devices are especially attractive today as tightening restriction from the Restrictions of Hazardous Substances Directive (RoHS) limit the amount of lead than can be used in electronic devices [78].

References

[1] Jaffe, B., Cook, W.R., Jaffe, H. (1971). *Piezoelectric Ceramics*. Academic Press.

[2] Generalic, E. (2018). Crystal system." *Croatian-English Chemistry Dictionary & Glossary*. 20 Oct. 2018. KTF-Split. 7 Aug. 2020. <https://glossary.periodni.com>.

[3] Jona, F., & Shirane, G. (1962). *Ferroelectric Crystals, International Series of Monographs on Solid State Physics*. Pergamon Press.

[4] Davis, M., Budimir, M., Damjanovic, D., & Setter, N. (2007). Rotator and extender ferroelectrics: Importance of the shear coefficient to the piezoelectric properties of domain-engineered crystals and ceramics. *Journal of Applied Physics, 101*(5), 054112.

[5] Tian, H., Meng, X., Hu, C., Tan, P., Cao, X., Shi, G., Zhou, Z., & Zhang, R. (2016). Origin of giant piezoelectric effect in lead-free $K_{1-x}Na_xTa_{1-y}Nb_yO_3$ single crystals. *Scientific Reports, 6*, 25637.

[6] Noheda, B. (2002). Structure and high-piezoelectricity in lead oxide solid solutions. *Current Opinion in Solid State and Materials Science, 6*(1), 27-34.

[7] Tao, H., & Wu, J. (2017). New poling method for piezoelectric ceramics. *Journal of Materials Chemistry C, 5*(7), 1601-1606.

[8] Borman, T. M. (2016). {001} Textured growth of doped, gradient free, lead zirconate titanate thin films by chemical solution deposition. *Doctoral Dissertation,* The Pennsylvania State University.

[9] Hollenstein, E., Damjanovic, D., & Setter, N. (2007). Temperature stability of the piezoelectric properties of Li-modified KNN ceramics. *Journal of the European Ceramic Society, 27*(13-15), 4093-4097.

[10] Zhuang, Z., Haun, M. J., Jang, S.-J., & Cross, L. E. (1989). Composition and temperature dependence of the dielectric, piezoelectric and elastic properties of pure PZT ceramics. *IEEE Transactions on Ultrasonics, Ferroelectrics, and Frequency Control, 36*(4), 413-416.

[11] Baker, D., Thomas, P., Zhang, N., & Glazer, A. (2009). A comprehensive study of the phase diagram of $K_xNa_{1-x}NbO_3$. *Applied Physics Letters, 95*(9), 091903.

[12] Petkov, V., Kim, J.-W., Shastri, S., Gupta, S., & Priya, S. (2020). Geometrical frustration and piezoelectric response in oxide ferroics. *Physical Review Materials, 4*(1), 014405.

[13] Huan, Y., Wei, T., Wang, Z., Lei, C., Chen, F., & Wang, X. (2019). Polarization switching and rotation in KNN-based lead-free piezoelectric ceramics near the polymorphic phase boundary. *Journal of the European Ceramic Society*, *39*(4), 1002-1010.

[14] Noheda, B., & Cox, D. (2006). Bridging phases at the morphotropic boundaries of lead oxide solid solutions. *Phase Transitions, 79*(1-2), 5-20.

[15] Zhang, B.P., Li, J.F., Wang, K. and Zhang, H. "Compositional dependence of piezoelectric properties in $Na_xK_{1-x}NbO_3$ lead-free ceramics prepared by spark plasma sintering." *Journal of the American Ceramic Society* 89.5 (2006): 1605-1609.

[16] Sedlar, M., & Sayer, M. (1995). Reactivity of titanium isopropoxide, zirconium propoxide and niobium ethoxide in the system of 2-methoxyethanol, 2, 4-pentanedione and water. *Journal of Sol-Gel Science and Technology, 5*(1), 27-40.

[17] Schneller, T., Waser, R., Kosec, M., & Payne, D. (2013). *Chemical Solution Deposition of Functional Oxide Thin Films*. Springer.

[18] Glinšek, S., Arčon, I., Malič, B., Kodre, A., & Kosec, M. (2012). Structural evolution of the $KTa_{0.6}Nb_{0.4}O_3$ alkoxide-based solutions: probing the transition metals local environment by X-ray absorption spectroscopy. *Journal of Sol-Gel Science and Technology, 62*(1), 1-6.

[19] Remondiere, F., Malič, B., Kosec, M., & Mercurio, J.-P. (2008). Study of the crystallization pathway of $Na_{0.5}Bi_{0.5}TiO_3$ thin films obtained by chemical solution deposition. *Journal of Sol-Gel Science and Technology, 46*(2), 117-125.

[20] Chowdhury, A., Bould, J., Londesborough, M. G., & Milne, S. J. (2010). Fundamental issues in the synthesis of ferroelectric $Na_{0.5}K_{0.5}NbO_3$ thin films by sol− gel processing. *Chemistry of Materials, 22*(13), 3862-3874.

[21] Wang, Y., & Li, W. (2000). Kinetics of acetic acid esterification with 2-methoxyethanol over a pillared clay catalyst. *Reaction Kinetics and Catalysis Letters, 69*(1), 169-176.

[22] Kupec, A., Uršič, H., Frunză, R. C., Tchernychova, E., & Malič, B. (2015). Microstructure-dependent leakage-current properties of solution-derived $(K_{0.5}Na_{0.5})NbO_3$ thin films. *Journal of the European Ceramic Society*, *35*(13), 3507-3511.

[23] Livage, J., Henry, M., & Sanchez, C. (1988). Sol-gel chemistry of transition metal oxides. *Progress in Solid State Chemistry, 18*(4), 259-341.

[24] Yi, G., Wu, Z., & Sayer, M. (1988). Preparation of $Pb(Zr,Ti)O_3$ thin films by sol gel processing: Electrical, optical, and electro-optic properties. *Journal of Applied Physics, 64*(5), 2717-2724.

[25] Ahmad, M., & Rusop, M. (2009). Influence of glacial acetic acid and nitric acid as a chelating agent in sol-gel process to the nanostructured titanium dioxide thin films. *AIP Conference Proceedings*.

[26] Nashimoto, K., Moriyama, H., & Osakabe, E. (1996). Control of crystallinity in sol-gel derived epitaxial $LiNbO_3$ thin films on sapphire. *Japanese Journal of Applied Physics, 35*(9S), 4936.

[27] Yan, X., Ren, W., Wu, X., Shi, P., & Yao, X. (2010). Lead-free $(K,Na)NbO_3$ ferroelectric thin films: Preparation, structure and electrical properties. *Journal of Alloys and Compounds, 508*(1), 129-132.

[28] Zhang, S. W., Luo, J., Zhou, Z., & Li, J. F. (2019). Sol-gel processed highly (100)-textured (K,Na)NbO_3-based lead-free thin films: Effect of pyrolysis temperature. *Journal of the American Ceramic Society, 102*(5), 2696-2705.

[29] Malic, B., Kupec, A., Vojisavljevic, K., & Pecnik, T. (2016). Lead-free ferroelectric thin films. *Handbook of Sol-Gel Science and Technology*.

[30] Yu, Q., Li, J. F., Chen, Y., Cheng, L. Q., Sun, W., Zhou, Z., & Wang, Z. (2014). Effect of pyrolysis temperature on sol–gel synthesis of lead-free piezoelectric (K,Na)NbO_3 films on Nb:$SrTiO_3$ substrates. *Journal of the American Ceramic Society, 97*(1), 107-113.

[31] Röscher, M., Schneller, T., & Waser, R. (2010). Comments on the processing of the niobium component for chemical solution derived niobium oxide-based thin-films. *Journal of Sol-Gel Science and Technology, 56*(3), 236-243.

[32] Kessler, V. G., Hubert-Pfalzgraf, L. G., Daniele, S., & Gleizes, A. (1994). Single-source precursors for $BaTiO_3$: synthesis and characterization of β-Diketonato alkoxides and molecular structure of $Ba_2Ti_2(thd)_4(\mu_3\text{-}OEt)_2(\mu\text{-}OEt)_4(OEt)_2(EtOH)_2$. *Chemistry of Materials, 6*(12), 2336-2342.

[33] Houng, B., Huang, C.-L., & Tsai, S.-Y. (2007). Effect of the pH on the growth and properties of sol–gel derived boron-doped ZnO transparent conducting thin film. *Journal of Crystal Growth, 307*(2), 328-333.

[34] Bretos, I., Jiménez, R., Ricote, J., & Calzada, M. L. (2018). Low-temperature crystallization of solution-derived metal oxide thin films assisted by chemical processes. *Chemical Society Reviews, 47*(2), 291-308.

[35] Hardy, A., Mondelaers, D., Van Bael, M., Mullens, J., Van Poucke, L., Vanhoyland, G., & D'Haen, J. (2004). Synthesis of $(Bi, La)_4Ti_3O_{12}$ by a new aqueous solution-gel route. *Journal of the European Ceramic Society, 24*(6), 905-909.

[36] Kang, C., Park, J.-H., Shen, D., Ahn, H., Park, M., & Kim, D.-J. (2011). Growth and characterization of $(K_{0.5}Na_{0.5})NbO_3$ thin films by a sol–gel method. *Journal of Sol-Gel Science and Technology, 58*(1), 85-90.

[37] Mauro, J.C. (2019). Nucleation and Crystallization. *Kinetics Lecture,* The Pennsylvania State University.

[38] Scherer, G. W. (1997). Sintering of sol-gel films. *Journal of Sol-Gel Science and Technology, 8*(1-3), 353-363.

[39] Kwok, C. K., & Desu, S. B. (1993). Low temperature perovskite formation of lead zirconate titanate thin films by a seeding process. *Journal of Materials Research, 8*(2), 339-344.

[40] Trolier-McKinstry, S., & Newnham, R. E. (2018). *Materials Engineering: Bonding, Structure, and Structure-Property Relationships*. Cambridge University Press.

[41] Cheng, C.-H., Xu, Y., & Mackenzie, J. D. (1994). Epitaxial growth of $KNbO_3$ and Fe-doped $KNbO_3$ films via sol-gel processing. *Sol-Gel Optics III*.

[42] Aksay, I. A., McVay, G., Ulrich, D. R., Miller, K., & Lange, F. (1989). *Processing Science of Advanced Ceramics* (Vol. 155). Materials Research Society Symposium.

[43] Coffman, P., Barlingay, C., Gupta, A., & Dey, S. (1996). Structure evolution in the PbO-ZrO_2-TiO_2 sol-gel system: Part II—Pyrolysis of acid and base-catalyzed bulk and thin film gels. *Journal of Sol-Gel Science and Technology, 6*(1), 83-106.

[44] Leikina B.B., Kostikov Y.P., & Olesk A.O. (1989) Effect of the chemical composition of titanium containing raw material on the properties of $BaTiO_3$. *Inorganic Materials,* 25:2050–2052.

[45] Norga, G., Vasiliu, F., Fé, L., Wouters, D., & Van der Biest, O. (2003). Role of fluorite phase formation in the texture selection of sol-gel-prepared Pb $(Zr_{1-x,}Ti_x)O_3$ films on Pt electrode layers. *Journal of Materials Research, 18*(5), 1232-1238.

[46] Wang, D. (2020). Low Temperature Processing of Electro-Ceramic Materials and Devices. *Doctoral Dissertation,* The Pennsylvania State University.

[47] Guo, H., Guo, J., Baker, A., & Randall, C. A. (2016). Hydrothermal-assisted cold sintering process: a new guidance for low-temperature ceramic sintering. *ACS Applied Materials & Interfaces, 8*(32), 20909-20915.

[48] Guo, H., Baker, A., Guo, J., & Randall, C. A. (2016). Protocol for ultralow-temperature ceramic sintering: an integration of nanotechnology and the cold sintering process. *ACS Nano, 10*(11), 10606-10614.

[49] Lange, F. (1996). Chemical solution routes to single-crystal thin films. *Science, 273*(5277), 903-909.

[50] Hasenkox, U., Hoffmann, S., & Waser, R. (1998). Influence of precursor chemistry on the formation of $MTiO_3$ (M=Ba,Sr) ceramic thin films. *Journal of Sol-Gel Science and Technology, 12*(2), 67-79.

[51] Kumar, S., Messing, G. L., & White, W. B. (1993). Metal organic resin derived barium titanate: I, Formation of barium titanium oxycarbonate intermediate. *Journal of the American Ceramic Society, 76*(3), 617-624.

[52] Malic, B., Jenko, D., Holc, J., Hrovat, M., & Kosec, M. (2008). Synthesis of sodium potassium niobate: A diffusion couples study. *Journal of the American Ceramic Society*, *91*(6), 1916-1922.

[53] Onwudili, J. A., & Williams, P. T. (2010). Hydrothermal reactions of sodium formate and sodium acetate as model intermediate products of the sodium hydroxide-promoted hydrothermal gasification of biomass. *Green Chemistry*, *12*(12), 2214-2224.

[54] Yoshioka, T., Ota, M., & Okuwaki, A. (2003). Conversion of a used poly (ethylene terephthalate) bottle into oxalic acid and terephthalic acid by oxygen oxidation in alkaline

solutions at elevated temperatures. *Industrial & Engineering Chemistry Research*, *42*(4), 675-679.

[55] Othmer, D. F., Gamer, C. H., & Jacobs, J. J. (1942). Oxalic acid from sawdust-optimum conditions for manufacture. *Industrial & Engineering Chemistry*, *34*(3), 262-267.

[56] Cohen, J. B. (1924). *Practical Organic Chemistry*. Macmillan.

[57] Calzada, M. L., Bretos, I., Jiménez, R., Guillon, H., & Pardo, L. (2004). Low-temperature processing of ferroelectric thin films compatible with silicon integrated circuit technology. *Advanced Materials, 16*(18), 1620-1624.

[58] Popovič, A., Bencze, L., Koruza, J., & Malič, B. (2015). Vapour pressure and mixing thermodynamic properties of the $KNbO_3$–$NaNbO_3$ system. *RSC Advances*, *5*(93), 76249-76256.

[59] Matsuda, T., Sakamoto, W., Lee, B.-Y., Iijima, T., Kumagai, J., Moriya, M., & Yogo, T. (2012). Electrical properties of lead-free ferroelectric Mn-doped $K_{0.5}Na_{0.5}NbO_3$–$CaZrO_3$ thin films prepared by chemical solution deposition. *Japanese Journal of Applied Physics, 51*(9S1), 09LA03.

[60] Wang, Y., Yao, K., Sharifzadeh Mirshekarloo, M., & Tay, F. E. H. (2016). Effects and mechanism of combinational chemical agents on solution-derived $K_{0.5}Na_{0.5}NbO_3$ piezoelectric thin films. *Journal of the American Ceramic Society, 99*(5), 1631-1636.

[61] Ahn, C., Lee, S., Lee, H., Ullah, A., Bae, J., Jeong, E., Choi, J., Park, B., & Kim, I. (2009). The effect of K and Na excess on the ferroelectric and piezoelectric properties of $K_{0.5}Na_{0.5}NbO_3$ thin films. *Journal of Physics D: Applied Physics, 42*(21), 215304.

[62] Kupec, A., Malic, B., Tellier, J., Tchernychova, E., Glinsek, S., & Kosec, M. (2012). Lead-free ferroelectric potassium sodium niobate thin films from solution: composition and structure. *Journal of the American Ceramic Society, 95*(2), 515-523.

[63] Marshall, J., Corkovic, S., Zhang, Q., Whatmore, R., Chima-Okereke, C., Roberts, W., Bushby, A., & Reece, M. (2006). The electromechanical properties of highly [100] oriented [$Pb(Zr_{0.52}Ti_{0.48})O_3$, PZT] thin films. *Integrated Ferroelectrics, 80*(1), 77-85.

[64] Lee, S. Y., Seog, H. J., Ahn, C. W., Ullah, A., & Kim, I. W. (2012). Interfacial Dead Layers on Lead Free Ferroelectric $(K_{0.5}Na_{0.5})(Mn_{0.005}Nb_{0.995})O_3$ Thin Films. *Japanese Journal of Applied Physics, 51*(9S2), 09MD03.

[65] Chowdhury, A., Bould, J., Londesborough, M. G., Večerníková, E., & Milne, S. J. (2010). Evidence of phase heterogeneity in sol–gel $Na_{0.5}K_{0.5}NbO_3$ system. *Materials Chemistry and Physics, 124*(1), 159-162.

[66] Kobayashi, K., Randall, C. A., Ryu, M., Doshida, Y., & Mizuno, Y. (2012, July). New opportunity in alkali niobate ceramics processed in low oxygen partial pressure. In *Proceedings of ISAF-ECAPD-PFM 2012* (pp. 1-4). IEEE.

[67] Hussain, F., Sterianou, I., Khesro, A., Sinclair, D. C., & Reaney, I. M. (2018). p-Type/n-type behaviour and functional properties of $K_xNa_{(1-x)}NbO_3$ ($0.49 \leq x \leq 0.51$) sintered in air and N2. *Journal of the European Ceramic Society*, *38*(9), 3118-3126.

[68] Kim, B. Y., Seong, T. G., Seo, I. T., Kim, J. S., Kang, C. Y., Yoon, S. J., & Nahm, S. (2012). Effects of oxygen pressure on electrical properties of $(Na_{0.5}K_{0.5})NbO_3$ films grown on Pt/Ti/SiO2/Si substrates. *Acta materialia*, *60*(20), 7034-7040.

[69] Shibata, K., Oka, F., Ohishi, A., Mishima, T., & Kanno, I. (2008). Piezoelectric properties of $(K,Na)NbO_3$ films deposited by RF magnetron sputtering. *Applied Physics Express, 1*(1), 011501.

[70] Kanno, I., Ichida, T., Adachi, K., Kotera, H., Shibata, K., & Mishima, T. (2012). Power-generation performance of lead-free $(K,Na)NbO_3$ piezoelectric thin-film energy harvesters. *Sensors and Actuators A: Physical, 179*, 132-136.

[71] Maier, R., Pomorski, T., Lenahan, P. M., & Randall, C. A. (2015). Acceptor-oxygen vacancy defect dipoles and fully coordinated defect centers in a ferroelectric perovskite lattice: Electron

paramagnetic resonance analysis of Mn^{2+} in single crystal $BaTiO_3$. *Journal of Applied Physics, 118*(16), 164102.

[72] Maier, R. A. (2014). Dynamics of oxygen vacancies and defect complexes in the perovskite oxide stricture. *Doctoral Dissertation,* The Pennsylvania State University.

[73] Kingery, W. D., Bowen, H. K., & Uhlmann, D. R. (1976). *Introduction to Ceramics* (Vol. 17). John Wiley & Sons.

[74] Kondo, N., Sakamoto, W., Lee, B. Y., Iijima, T., Kumagai, J., Moriya, M., & Yogo, T. (2010). Improvement in ferroelectric properties of chemically synthesized lead-free piezoelectric $(K,Na)(Nb,Ta)O_3$ thin films by Mn doping. *Japanese Journal of Applied Physics, 49*(9S), 09MA04.

[75] Zhang, B. P., Li, J. F., Wang, K., & Zhang, H. (2006). Compositional dependence of piezoelectric properties in $Na_xK_{1-x}NbO_3$ lead-free ceramics prepared by spark plasma sintering. *Journal of the American Ceramic Society, 89*(5), 1605-1609.

[76] Huan, Y., Wang, X., Shen, Z., Kim, J., Zhou, H., & Li, L. (2014). Nanodomains in KNN-based lead-free piezoelectric ceramics: Origin of strong piezoelectric properties. *Journal of the American Ceramic Society, 97*(3), 700-703.

[77] Rubio-Marcos, F., Ochoa, P., & Fernandez, J. (2007). Sintering and properties of lead-free $(K,Na,Li)(Nb,Ta,Sb)O_3$ ceramics. *Journal of the European Ceramic Society, 27*(13-15), 4125-4129.

[78] Shrout, T. R., & Zhang, S. J. (2007). Lead-free piezoelectric ceramics: Alternatives for PZT? *Journal of Electroceramics, 19*(1), 113-126.

[79] Li, J. F., Wang, K., Zhang, B. P., & Zhang, L. M. (2006). Ferroelectric and piezoelectric properties of fine-grained $Na_{0.5}K_{0.5}NbO_3$ lead-free piezoelectric ceramics prepared by spark plasma sintering. *Journal of the American Ceramic Society, 89*(2), 706-709.

[80] Pop-Ghe, P., Stock, N., & Quandt, E. (2019). Suppression of abnormal grain growth in $K_{0.5}Na_{0.5}NbO_3$: phase transitions and compatibility. *Scientific Reports, 9*(1), 1-10.

[81] Fanfoni, M., & Tomellini, M. (1998). The johnson-mehl-avrami-kohnogorov model: a brief review. *Il Nuovo Cimento D*, *20*(7-8), 1171-1182.

[82] Avrami, M. (1939). Kinetics of phase change. I General theory. *The Journal of Chemical Physics*, *7*(12), 1103-1112.

[83] Avrami, M. (1940). Kinetics of phase change. II transformation-time relations for random distribution of nuclei. *The Journal of Chemical Physics*, *8*(2), 212-224.

[84] William, J., & Mehl, R. (1939). Reaction kinetics in processes of nucleation and growth. *Transactions of the Metallurgical Society of AIME*, *135*, 416-442.

[85] Kwok, C. K., & Desu, S. B. (1994). Formation kinetics of $PbZr_xTi_{1-x}O_3$ thin films. *Journal of Materials Research, 9*(7), 1728-1733.

[86] Yu, Q., Zhu, F. Y., Cheng, L. Q., Wang, K., & Li, J. F. (2014). Determination of crystallographic orientation of lead-free piezoelectric (K,Na)NbO_3 epitaxial thin films grown on $SrTiO_3$ (100) surfaces. *Applied Physics Letters*, *104*(10), 102902.

[87] Peng, C. H., & Desu, S. B. (1991). Investigation of structure development in MOD $Pb(Zr_xTi_{1-x})O_3$ films by an optical method. *MRS Online Proceedings Library Archive*, *243*.

[88] Du, Z. H., Zhang, T. S., Zhu, M. M., & Ma, J. (2009). Perovskite crystallization kinetics and dielectric properties of the PMN-PT films prepared by polymer-modified sol-gel processing. *Journal of Materials Research*, *24*(4), 1576-1584.

[89] Griswold, E. M., Weaver, L., Sayer, M., & Calder, I. D. (1995). Phase transformations in rapid thermal processed lead zirconate titanate. *Journal of materials research*, *10*(12), 3149-3159.

[90] Lakeman, C. D., & Payne, D. A. (1992). Processing effects in the sol–gel preparation of PZT dried gels, powders, and ferroelectric thin layers. *Journal of the American Ceramic Society, 75*(11), 3091-3096.

[91] Kovacova, V., Yang, J. I., Jacques, L., Ko, S. W., Zhu, W., & Trolier-McKinstry, S. (2020). Comparative solution synthesis of Mn doped (Na,K)NbO_3 thin films. *Chemistry–A European Journal*.

[92] Yanovskaya, M., Obvintseva, I., Solovyova, L., Kovsman, E., Vorotilov, K., & Vasilyev, V. (1998). Alkoxy-derived ferroelectric PZT films: the effect of lead acetate dehydration techniques and lead content in the electrochemically prepared solutions on the properties of the films. *Integrated Ferroelectrics, 19*(1-4), 193-209.

[93] Kotova, N., Vorotilov, K., Seregin, D., & Sigov, A. (2014). Role of precursors in the formation of lead zirconate titanate thin films. *Inorganic Materials, 50*(6), 612-616.

[94] Wang, L., Yao, K., Goh, P. C., & Ren, W. (2009). Volatilization of alkali ions and effects of molecular weight of polyvinylpyrrolidone introduced in solution-derived ferroelectric $K_{0.5}Na_{0.5}NbO_3$ films. *Journal of Materials Research, 24*(12), 3516-3522.

[95] Wiegand, S., Flege, S., Baake, O., & Ensinger, W. (2012). Influence of different heat treatment programs on properties of sol–gel synthesized $(Na_{0.5}K_{0.5})NbO_3$ (KNN) thin films. *Bulletin of Materials Science, 35*(5), 745-750.

[96] Vorotilov, K., Yanovskaya, M., Turevskaya, E., & Sigov, A. (1999). Sol-gel derived ferroelectric thin films: avenues for control of microstructural and electric properties. *Journal of Sol-Gel Science and Technology, 16*(1-2), 109-118.

[97] Li, G., Wu, X., Ren, W., Yan, X., Shi, P., Chen, X., & Yao, X. (2010). Phase Formation and Properties of Mod Derived $(Na_{0.52}K_{0.48})NbO_3$ Thin Films. *Ferroelectrics, 404*(1), 63-68.

[98] Wilke, R. H., Moses, P. J., Jousse, P., Yeager, C., & Trolier-McKinstry, S. (2012). Wafer mapping of the transverse piezoelectric coefficient, $e_{31,f}$, using the wafer flexure technique with sputter deposited Pt strain gauges. *Sensors and Actuators A: Physical, 173*(1), 152-157.

[99] Shepard Jr, J., Moses, P., & Trolier-McKinstry, S. (1998). The wafer flexure technique for the determination of the transverse piezoelectric coefficient (d_{31}) of PZT thin films. *Sensors and Actuators A: Physical, 71*(1-2), 133-138.

[100] Wolf, R., & Trolier-McKinstry, S. (2004). Temperature dependence of the piezoelectric response in lead zirconate titanate films. *Journal of Applied Physics, 95*(3), 1397-1406.

[101] John, M. J., Muraleedharan, K., Kannan, M. P., & Devi, T. G. (2012). Effect of semiconducting metal oxide additives on the kinetics of thermal decomposition of sodium oxalate under isothermal conditions. *Thermochimica Acta*, *534*, 71-76.

[102] Higashiyama, T., & Hasegawa, S. (1971). The differential thermal analysis of potassium oxalate. *Bulletin of the Chemical Society of Japan*, *44*(7), 1727-1730.

[103] Bamford, C. H., & Dewar, M. J. S. (1949). 608. The thermal decomposition of acetic acid. *Journal of the Chemical Society (Resumed)*, 2877-2882.

[104] Abdel-Rahman, M. A., Al-Hashimi, N., Shibl, M. F., Yoshizawa, K., & El-Nahas, A. M. (2019). thermochemistry and Kinetics of the thermal Degradation of 2-Methoxyethanol as Possible Biofuel Additives. *Scientific Reports*, *9*(1), 1-15.

[105] Choudhury, T. K., & Lin, M. C. (1990). Homogeneous pyrolysis of acetylacetone at high temperatures in shock waves. *International Journal of Chemical Kinetics*, *22*(5), 491-504.

[106] Hoene, J. V., Charles, R. G., & Hickam, W. M. (1958). Thermal decomposition of metal acetylacetonates: mass spectrometer studies. *The Journal of Physical Chemistry*, *62*(9), 1098-1101.

[107] Potassium Acetate (2020) Standard Reference Database 69: *NIST Chemistry WebBook*.

[108] Potassium Oxalate (2020) Standard Reference Database 69: *NIST Chemistry WebBook*.

[109] Lee, S. Y., Ahn, C. W., Ullah, A., Seog, H. J., Kim, J. S., Bae, S. H., & Kim, I. W. (2011). Effect of Mn substitution on ferroelectric and leakage current characteristics of lead-free $(K_{0.5}Na_{0.5})(Mn_xNb_{1-x})O_3$ thin films. *Current Applied Physics, 11*(3), S266-S269.

[110] Lu, T., Zhu, K., Liu, J., Wang, J., & Qiu, J. (2014). Lead-free (K,Na)NbO_3 thin films derived from chemical solution deposition modified with EDTA. *Journal of Materials Science: Materials in Electronics*, *25*(2), 1112-1116.

[111] Lotgering, F. K. (1959). Topotactical reactions with ferrimagnetic oxides having hexagonal crystal structures—I. *Journal of Inorganic and Nuclear Chemistry*, *9*(2), 113-123.

[112] Yilmaz, H. (2002). Texturing of $Na_{1/2}Bi_{1/2}TiO_3$-$BaTiO_3$ Ceramics by Templated Grain Growth. *Doctoral Dissertation,* The Pennsylvania State University.

[113] Kimura, H., Tanahashi, R., Zhao, H., & Yao, Q. (2012). Weak ferroelectricity of potassium niobate $K_4Nb_6O_{17}$ single crystal grown by pulling down technique. *Materials Letters*, *84*, 16-19.

[114] Zhong, T., Tang, J., Zhu, M., Hou, Y., Wang, H., & Yan, H. (2005). Synthesis and characterization of layered niobate $K_4Nb_6O_{17}$ thin films by niobium-chelated precursor. *Journal of Crystal Growth*, *285*(1-2), 201-207.

[115] Ihlefeld, J. F., Harris, D. T., Keech, R., Jones, J. L., Maria, J. P., & Trolier-McKinstry, S. (2016). Scaling effects in perovskite ferroelectrics: fundamental limits and process-structure-property relations. *Journal of the American Ceramic Society*, *99*(8), 2537-2557.

[116] Ozmen, O., Ozsoy-Keskinbora, C., & Suvaci, E. (2018). Chemical stability of $KNbO_3$, $NaNbO_3$, and $K_{0.5}Na_{0.5}NbO_3$ in aqueous medium. *Journal of the American Ceramic Society*, *101*(3), 1074-1086.

[117] Mehrotra, R. C., & Kapoor, P. N. (1964). Organic compounds of niobium: I. Reactions of niobium penta-ethoxide with organic esters. *Journal of the Less Common Metals*, *7*(2), 98-101.

[118] Vandenborre, M. T., Poumellec, B., Alquier, C., & Livage, J. (1989). EXAFS study of the hydrolysis of niobium pentaethoxide. *Journal of Non-Crystalline Solids*, *108*(3), 333-337.

[119] Holloway, P. H., & Hudson, J. B. (1974). Kinetics of the reaction of oxygen with clean nickel single crystal surfaces: I. Ni (100) surface. *Surface Science*, *43*(1), 123-140.

[120] Trivedi, R., & Kurz, W. (1994). Dendritic growth. *International Materials Reviews*, *39*(2), 49-74.

[121] Won, S. S., Lee, J., Venugopal, V., Kim, D. J., Lee, J., Kim, I. W., Kingon, A., & Kim, S. H. (2016). Lead-free Mn-doped $(K_{0.5},Na_{0.5})NbO_3$ piezoelectric thin films for MEMS-based vibrational energy harvester applications. *Applied Physics Letters*, *108*(23), 232908.

[122] Li, R., Sun, X. X., Zheng, T., & Wu, J. (2020). Defect engineering electrical properties of lead-free potassium sodium niobate-based ceramics. *Journal of the American Ceramic Society*, *103*(1), 444-453.

[123] Hwang, G. T., Park, H., Lee, J. H., Oh, S., Park, K. I., Byun, M., Park, H., Ahn, G., Jeong, C. K., No, K., Kwon, H., Lee, S., Joung, B., & Lee, K. J. (2014). Self-powered cardiac pacemaker enabled by flexible single crystalline PMN-PT piezoelectric energy harvester. *Advanced materials*, *26*(28), 4880-4887.

[124] Jung, W. S., Lee, M. J., Kang, M. G., Moon, H. G., Yoon, S. J., Baek, S. H., & Kang, C. Y. (2015). Powerful curved piezoelectric generator for wearable applications. *Nano Energy*, *13*, 174-181.

Appendix

Precursor Calculations

Weights for precursors were calculated using a Microsoft Excel® spreadsheet with the following calculations.

1	KNN Precursor Calculator by Leonard Jacques						
2							
3			By Molarity:			Precursor weight (g):	
4							
5		INPUT:	Sol. Molarity (M)	0.4	Output:	Na-acetate	0.69661
6		Output:	Sol Volume (mL)	40.4191	Output:	K-acetate	0.85754
7	https://wv	INPUT:	Nb Analysis conc. (wt. %)	28.6	Output:	Mn-acetate tetrahydrate	0.03963
8			Excess Na (mol %)	4			
9			Excess K (mol %)	7			
10			Manganese (mol %)	1			
11		INPUT:	Nb Precursor wt. (g)	5.2			
12							
13			Stoich. Frac. Na	0.5			
14			Stoich. Frac. K	0.5			
15			Na Purity (%)	99			
16			K Purity (%)	99			
17			Mn ac-4H2O Purity (%)	99.99			

Figure **A-1**: Microsoft Excel calculator for KNN precursors.

Inputs: desired solution molarity, weight percent of niobium from industry analysis of the niobium precursor, and the weight of niobium precursor added to the solution, manganese content, sodium and potassium excess content, purities, and molar ratio of Na:K.

Where:

M = target solution molarity

f_n = stoichiometric fraction of Na

f_k = stoichiometric fraction of K

f_m = stoichiometric fraction of Mn

Na_{ex} = % excess Na

K_{ex} = % excess K

Na_p = % purity of Na-acetate precursor

K_p = % purity of K-acetate precursor

Mn_p = % purity of Mn-acetate tetrahydrate precursor

V_{mL} = target solution volume – in mL

YIELD (grams)

$$Na - acetate\ (wt., grams) = M \times f_n \times \frac{100 + Na_{ex}}{100} \times \frac{100}{Na_p} \times \frac{V_{mL}}{1{,}000} \times 82.03 \frac{grams\ Na\ acetate}{mol}$$

$$K - acetate\ (wt., grams) = M \times f_k \times \frac{100 + K_{ex}}{100} \times \frac{100}{K_p} \times \frac{V_{mL}}{1{,}000} \times 98.15 \frac{grams\ K\ acetate}{mol}$$

$$Mn - acetate\ tetrahydtate\ (wt., grams) = M \times \frac{f_m}{100} \times \frac{100}{Mn_p} \times \frac{V_{mL}}{1{,}000} \times 245.09 \frac{grams\ Mn\ acetate\ tetrahydrate}{mol}$$

TGA-DSC and XRD on KNN-A, B, and C Powders

Carbonate decomposition is known to be endothermic [20], however the peaks under 700°C are exothermic. It is likely that the endotherm at the conclusion of each DSC scan is due to carbonate decomposition. A late rise in evolved CO_2 is detected above 800°C in the MS due to the decomposition of residual carbonates.

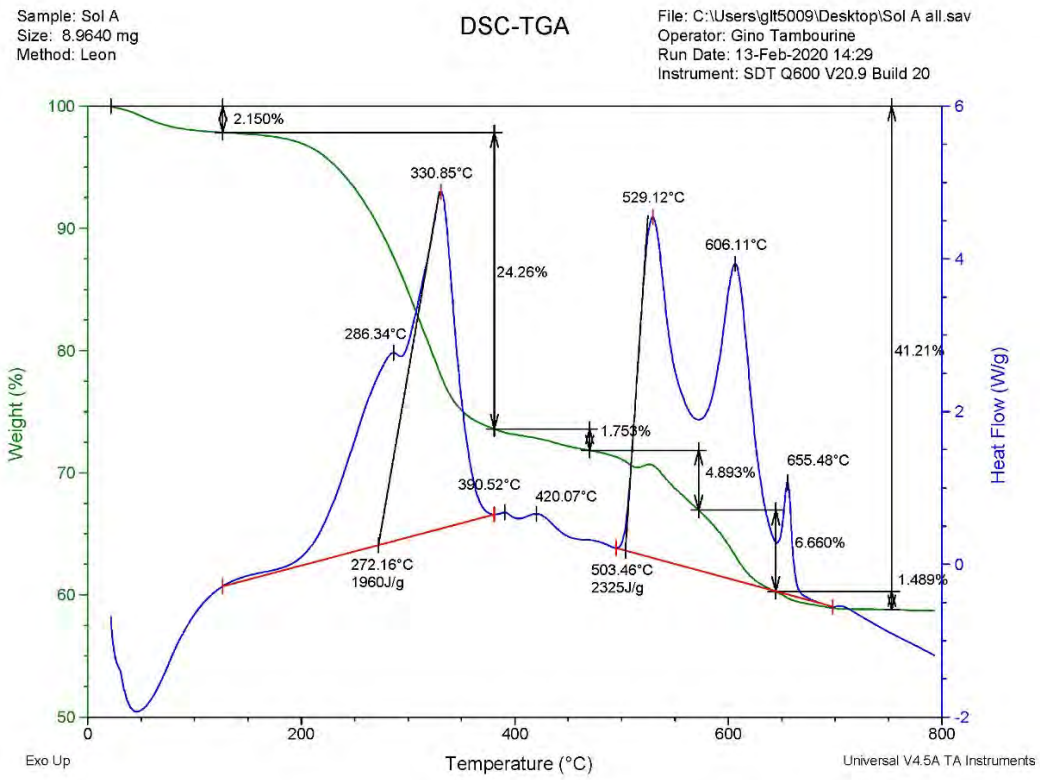

Figure **A-2**: Simultaneous TGA-DSC on KNN-A powders.

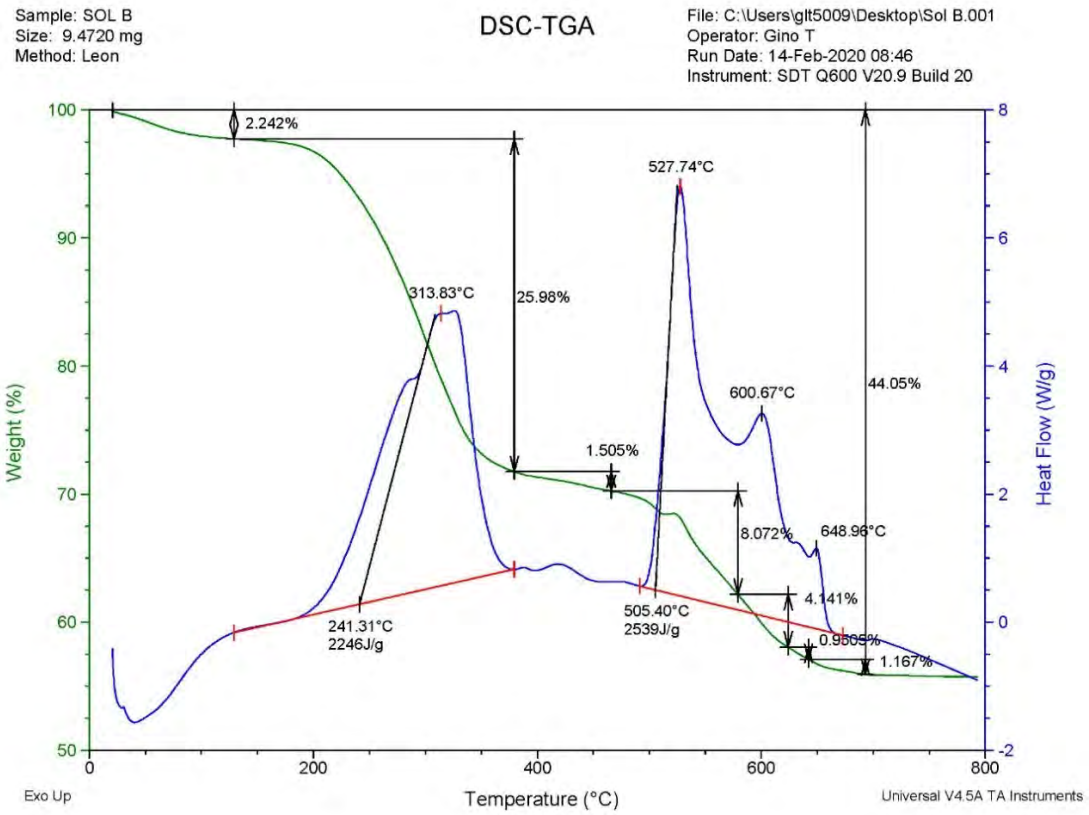

Figure **A-3**: Simultaneous TGA-DSC on KNN-B powders.

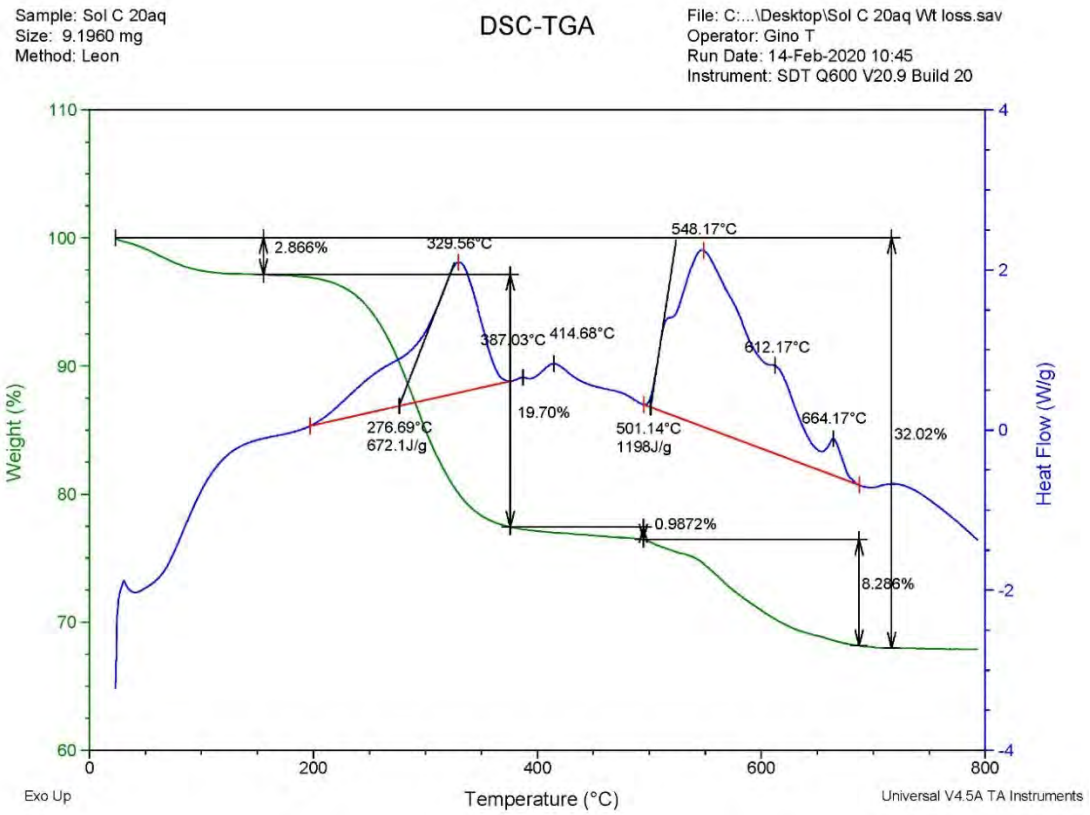

Figure **A-4**: Simultaneous TGA-DSC on KNN-C powders from solution C aged for 5 months. 20 mL of acetic anhydride was added to the solution before refluxing.

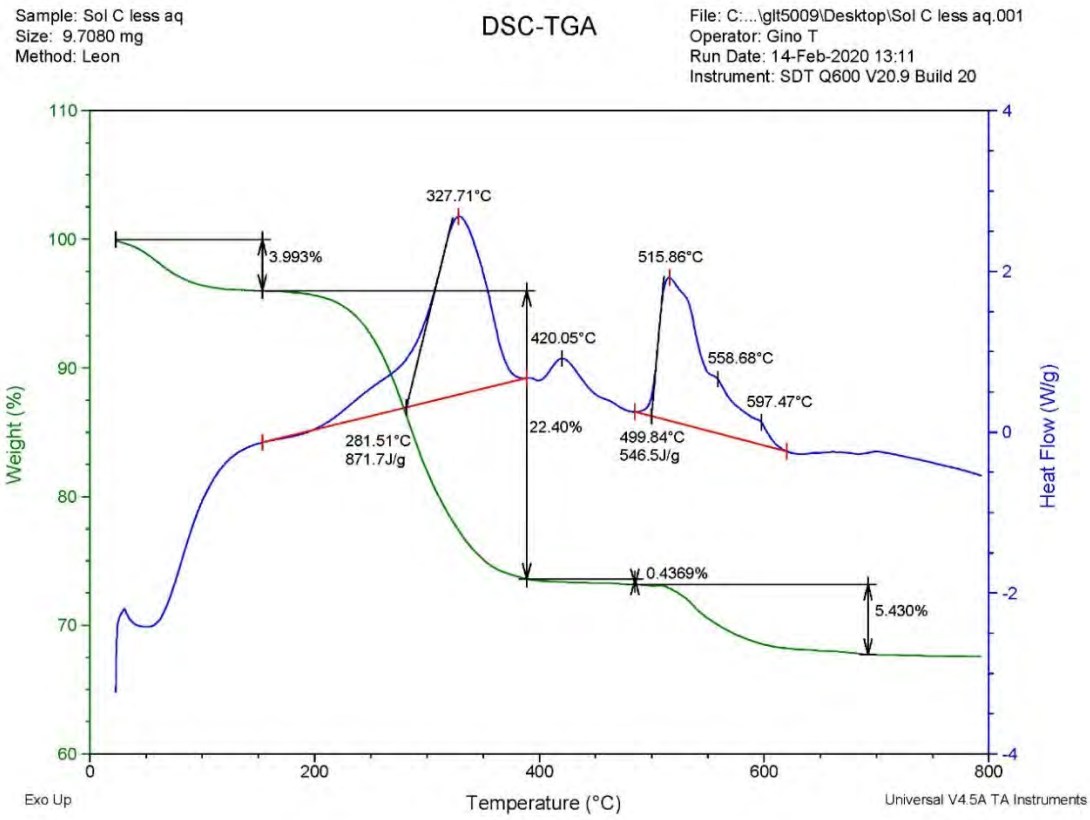

Figure **A-5**: Simultaneous TGA-DSC on KNN-C powders. 13 mL of acetic anhydride was added to the solution before refluxing.

Figure **A-6**: XRD pattern of KNN-A, B, and C powders after their respective TGA-DSC scans. Sol C20 was refluxed with 20 mL of acetic anhydride, and solC 13 with 13 mL of acetic anhysride.

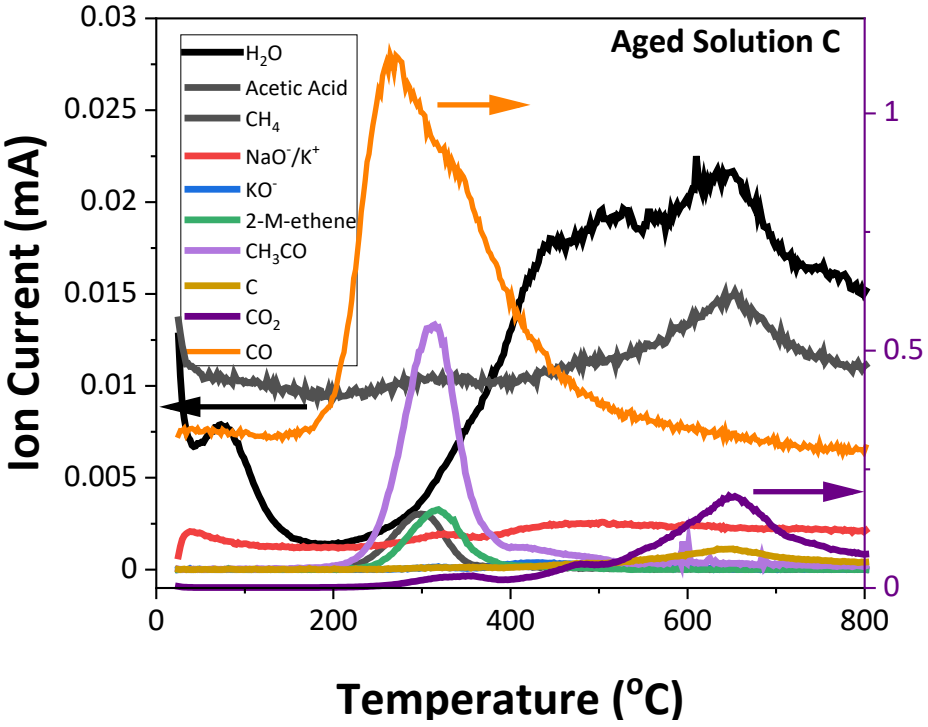

Figure **A-7**: Mass spectrometry of KNN-C powder from aged solution (c.f. Figure A-4). Most of the CO_2 evolution is at higher temperatures. The corresponding XRD of this powder reveals the existence of hydrated carbon species (c.f. Figure A-6, Sol C20).

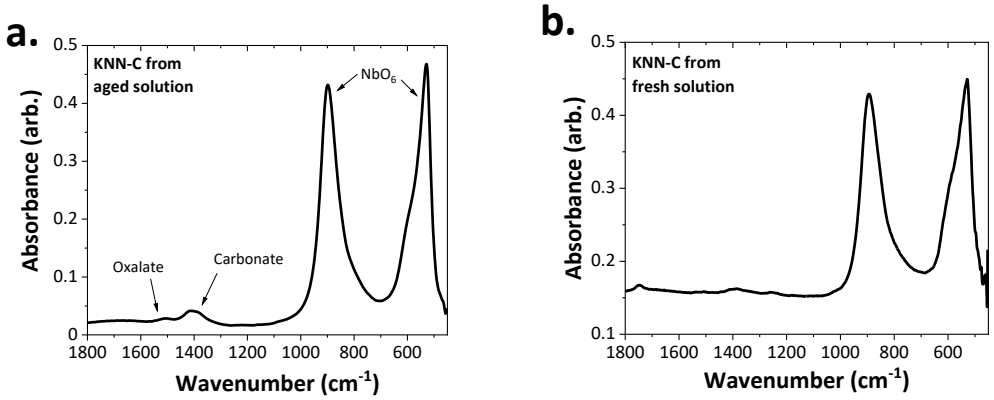

Figure **A-8**: FTIR spectra of fully crystalline KNN-C deposited from aged solution (a) (c.f. Figure A-8) and from 2 week old solution (b) (c.f. Figure 4-16c). (a.) was deposited four months after the solution was made, and was exposed to ambient atmosphere for about 2 months before the FTIR spectra was taken. (b.) was deposited about 2-weeks after the solution was made and was exposed to atmosphere for 11 months before the FTIR spectra was taken.

In Fig. A-8, films prepared from fresh KNN-C solutions showed little retained carbon, while in partially crystalline films from aged KNN-C solutions, the presence of residual carbonates and oxalates were detected (see Figure 4-5, c.f. Figure 5-8). As was shown in Chapter 5, retained carbon was also observed in partially crystalline films from fresh KNN-C solutions.

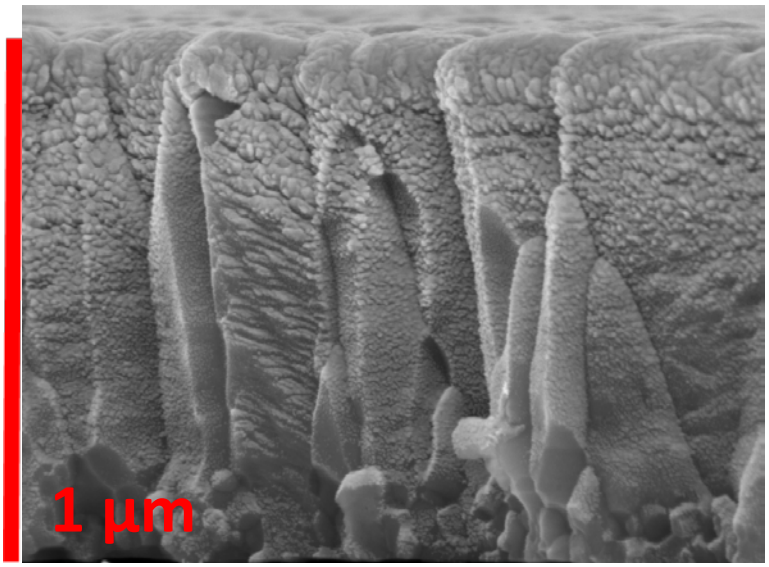

Figure **A-9**: A cross-section micrograph of a film deposited from 20-week old solution C and with 1-step pyrolysis at 300°C, showing columnar grain boundaries in some sections covered with secondary phases through the thickness, and on the surface. This film was annealed in standing air, and the comparison annealed in in 2 SLPM O_2 did not show these microstructures.

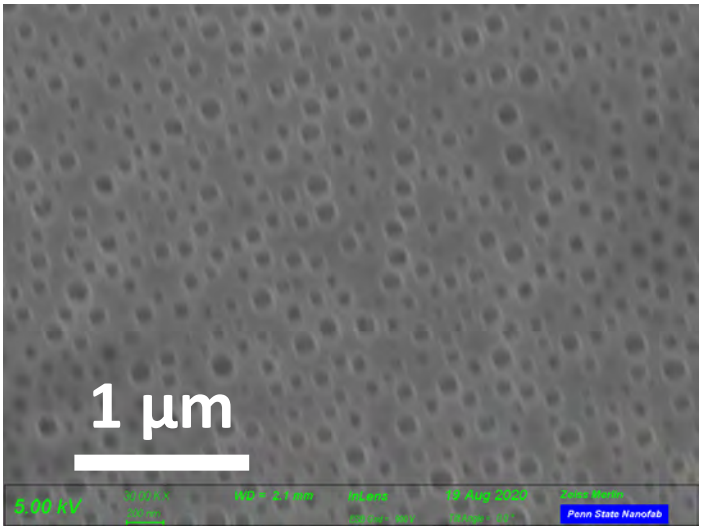

Figure **A-10**: Porosity in KNN-A films after drying at 250°C – only.

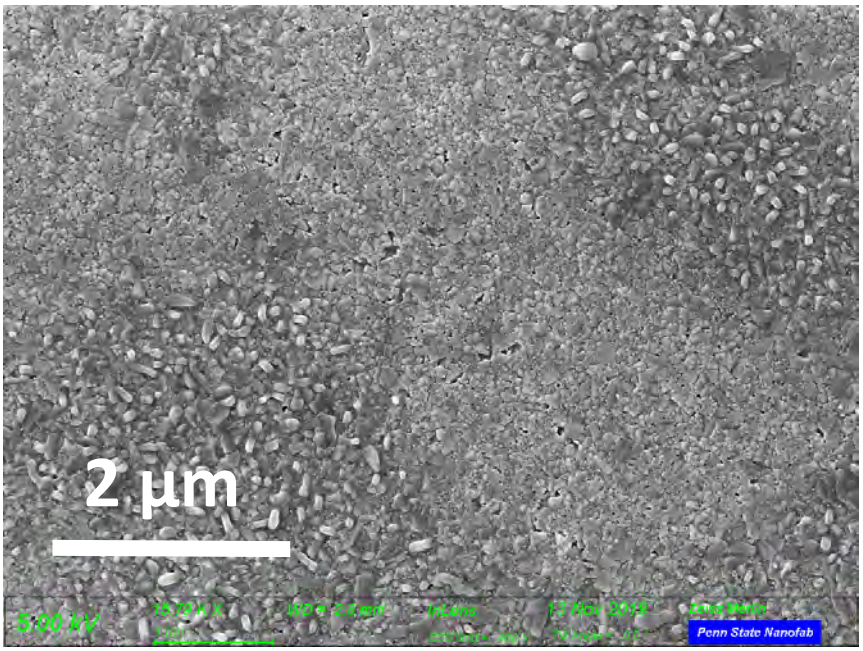

Figure **A-11**: FESEM micrographs of KNN-C films annealed in nitrogen typically show multiple mictostructures on the surface of the film, as in the micrograph shown here.

Calculation of the Mass Loss Due to Excess Alkali on TGA

<u>For calculating the mass loss from K_2O due to excess</u>

Molar Mass of $K_{0.5}Na_{0.5}NbO_3$ = 171.9496 g/mole

$$\frac{0.5(K)}{KNN}(molar\ mass) = 0.1137$$

The mass fraction of K in KNN is = 0.1137

$$0.1 \times (mass\ fraction\ potassium) = 0.01137$$

For 10% excess K the fraction of the value of the molar mass of KNN = 0.01137

$$\frac{K_2O}{2(K)} = 1.205;\ 1.205 \times (excess\ mass\ fraction) = 0.0137$$

Converting the K to K_2O (adding the mass of one oxygen for every two K) → the molar mass fraction is now 0.0137

$$0.0137 \times TG_{\%,800°C} = \%\ ex.K_2O\ loss$$

For calculating the mass loss from Na_2O due to excess

Multiply 0.0137 by the mass at 800°C on the TG plot and that is the percent mass loss due to Na_2O

Fraction that is Na = 0.0669

For 5% excess Na the fraction of the value of the molar mass of KNN = 0.00334

Converting the Na to Na_2O (adding the mass of one oxygen for every two K) → the molar mass fraction is now 0.0045

Multiply 0.0045 by the mass reading at 800°C on the TG plot and that is the percent mass loss due to Na_2O

The following calculation is following the assumption that all Na and K transforms to the perovskite phase from the oxalate phases:

Mass loss due to CO_2 and CO evolution from $K_2C_2O_4$

Mass of CO_2 and CO = 72 g/mol

Loss per K: $\frac{0.5(CO_2,CO)}{(K)}(molar\ mass) = 0.92\ (mass\ ratio\ of\ C_2O_3\ relative\ to\ K\ in\ K_2C_2O_4\ )$

Mass fraction of K (relative to stoichiometric KNN) (including excess) = 0.1137+0.01137=0.1251

$(mass\ ratio\ of\ C_2O_3\ relative\ to\ each\ K\ in\ K_2C_2O_4\ ) \times (mass\ fraction\ potassium\ w\ ex.) = 0.115$ Multiply mass ratio of (CO_2, CO) by the mass fraction of K = 0.115

→ gives the fraction of the mass of CO2 and CO evolved relative to the amount of remaining stoichiometric perovskite phase.

$$0.115 \times TG_{\%,800°C} = \%\ (CO_2, CO)\ loss\ from\ K_2C_2O_4$$

Multiply by the weight % reading in the TG at 800°C

Mass loss due to CO_2 and CO evolution from $Na_2C_2O_4$

Mass of CO_2 and CO = 72 g/mol

Loss per K: $\frac{0.5(CO_2,CO)}{(Na)}(molar\ mass) = 1.57\ (mass\ ratio\ of\ C_2O_3\ relative\ to\ each\ Na\ in\ Na_2C_2O_4\ )$

Mass fraction of Na (relative to stoichiometric KNN) (including excess) = 0.0669+0.00334=0.0702

$(mass\ ratio\ of\ C_2O_3\ relative\ to\ each\ Na\ in\ Na_2C_2O_4\ ) \times (mass\ fraction\ sodium\ w\ ex.) = 0.1102$ Multiply mass ratio of (CO_2, CO) by the mass fraction of Na = 0.11

→ gives the fraction of the mass of CO2 and CO evolved relative to the amount of remaining stoichiometric perovskite phase.

$$0.11 \times TG_{\%,800°C} = \%\ (CO_2, CO)\ loss\ from\ Na_2C_2O_4$$

Multiply by the weight % reading in the TG at 800°C

MATLAB Code for Volume Fraction Calculation

Activation Energy Calculations:

Volume % (MATLAB code):

```
% BW_ = The binary matrix where white pixels (crystalline) have
the value
% 1 and black pixels (amorphous) have the value 0.
%
% "sum()" calculates the sum of each binary matrix, BW_
%
% X = vector containing the sum of 10 BW_ matrices
%
% X_ave = The average of vector X


X =
[sum(BW(:));sum(BW1(:));sum(BW2(:));sum(BW3(:));sum(BW4(:));sum(BW5(:))
;sum(BW6(:));sum(BW7(:));sum(BW8(:));sum(BW9(:))]
X_ave = sum(X)/10
```

Failure to Clean with a Sonicating Bath in IPA:

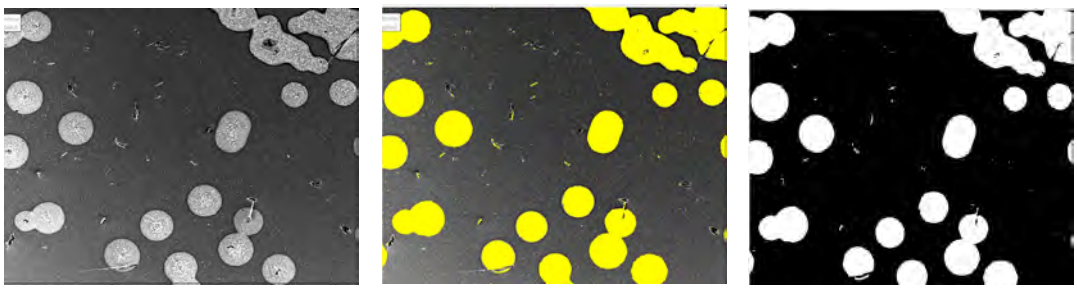

Figure **A-12**: Microscopy of a partially crystallized KNN film without a sonicating IPA bath prior to deposition. The dark area is the amorphous matrix. The brighter areas are the crystalline rosettes. The raw FESEM image (left) was segmented using adaptive image segmentation or the graph-cut method (middle) to generate a binary image (right). Small amounts of debris are falsely recognized as crystalline KNN.

Activation Energy for Nucleation from the Average Nucleation Rate

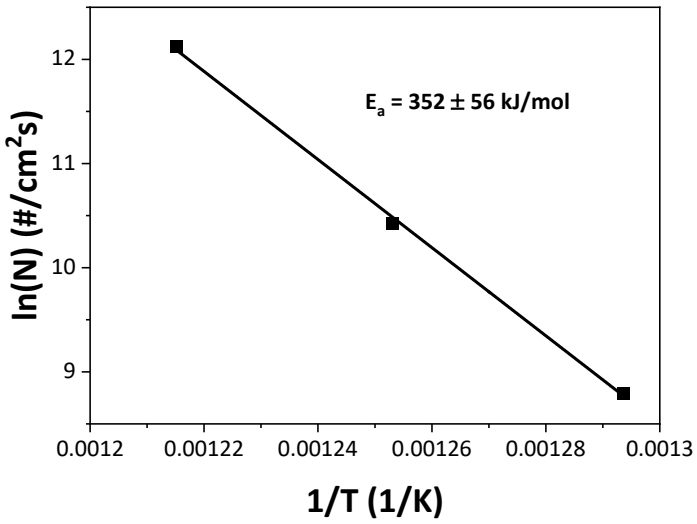

Figure **A-13**: Arrhenius plot for the activation energy of nucleation by the average nucleation rates at 500°C, 525°C, and 550°C.

Error Propagations for the Activation Energies

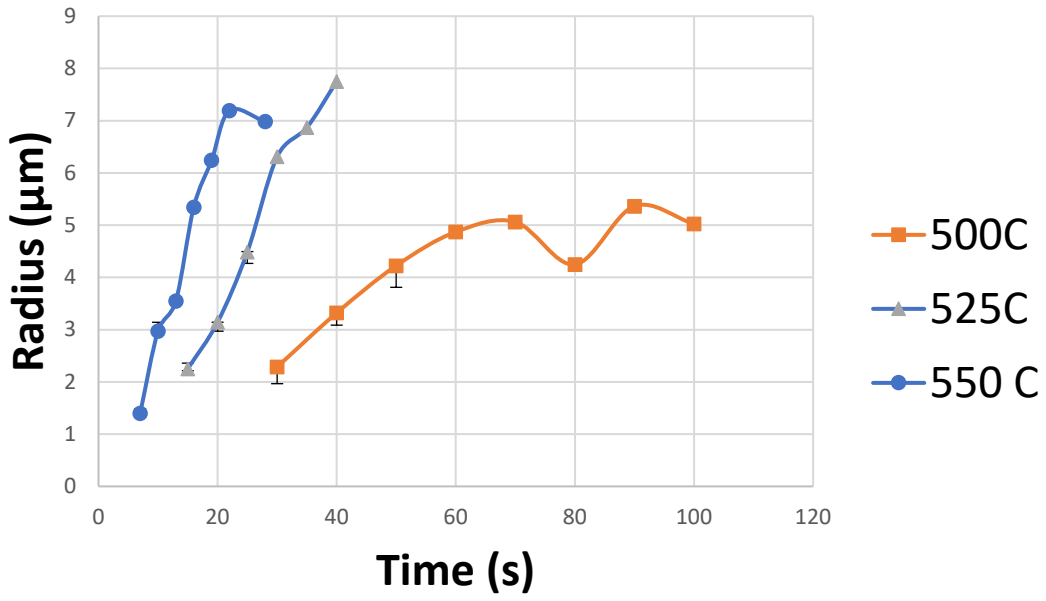

Figure **A-14**: Measurement error in determining the linear dimension (radius) of KNN rosettes.

The measurement error for rosette radius was determined by measuring one rosette from each temperature at high resolution and making 10 measurements of the same rosette at the magnification used for determining rosette size. Rosettes measured at that magnification were compared with the same rosette measured at high magnification. The error bars on the measured data represent the comparison of radius at standard measurement magnification to the "true" or average radius at high resolution. Deviations for the first three measurements at each temperature are shown in Figure A-10.

The error in activation energy for rosette growth was calculated by finding the standard error of slope from a linear regression for the lines on the plot of ln(k) vs. 1/T in Figure A-8. The standard error of the slope multiplied by the gas constant 8.314 J/mol*K gives the standard error of ± 10 kJ/mol for the growth activation energy.

$$SE(slope) = \sqrt{\frac{1}{n-2} \cdot \frac{\sum(y_i - \hat{y}_i)^2}{\sum(x_i - \hat{x}_i)^2}}$$

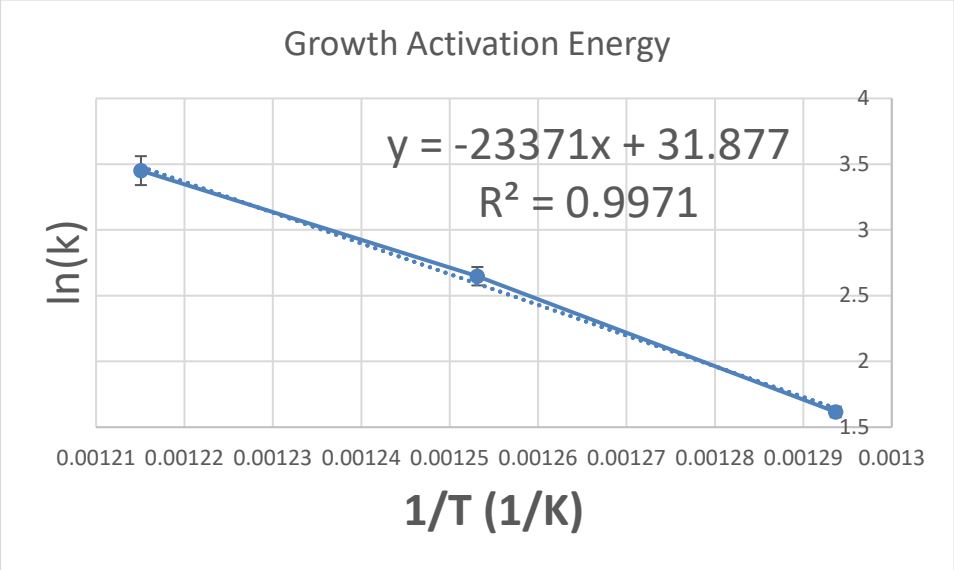

Figure **A-15**: The activation energy for rosette growth. Natural log of the rate constant plotted vs. 1/T. The dashed line is the linear regression. Error bars for the rate constants are displayed.

The error for perovskite formation was calculated following the same method for rosette growth, and in this method yielded a standard error of 13 kJ/mol. A second method to calculate error considering the standard errors of ln(k) shown in Figure A-11. The error bars in Figure A-13 -are the standard error of the y-intercept for linear regression of the plot in Figure A-12, where the y-intercept is ln(k).

Standard error in the y-intercept was calculated using the function below.

$$SE(y - intercept) = \sqrt{\frac{1}{n^2 - 2n} \cdot \frac{\sum x_i^2 \sum(y_i - \hat{y}_i)^2}{\sum(x_i - \hat{x}_i)^2}}$$

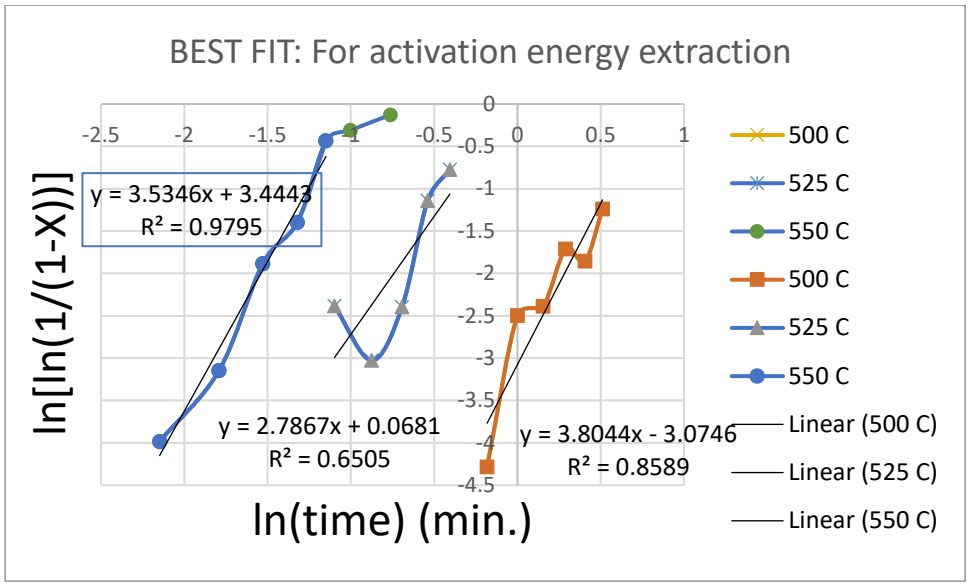

Figure **A-16**: A Johnson-Avrami-Mehl plot for volume faction crystallized, where the slope is the time constant and the y-intercept is ln(k) which are used for the Arrhenius plot in Figure A-13. The solid black line through each data set is a linear regression. Data at 550°C, 525°C, and 500°C are plotted.

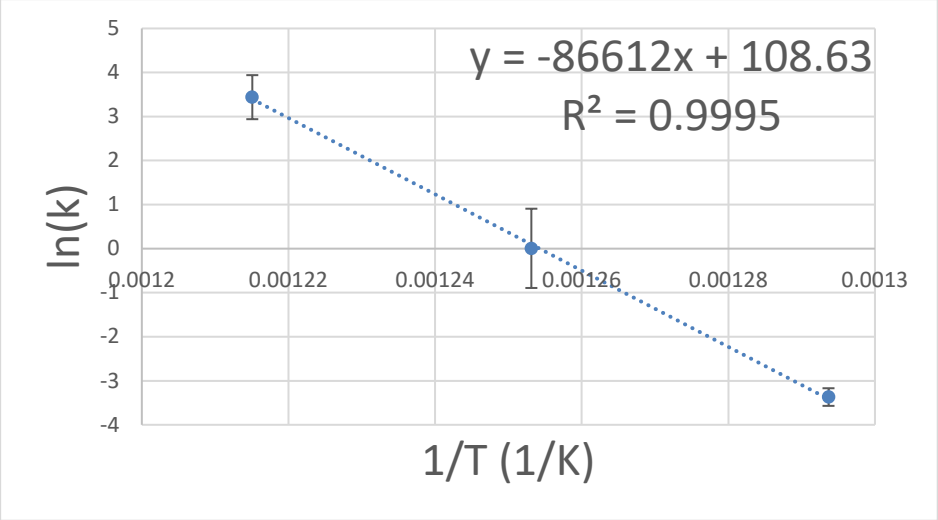

Figure **A-17**: The activation energy for perovskite KNN formation. Natural log of the rate constant plotted vs. 1/T. The dashed line is the linear regression. Solid black lines are used for the second error method. Error bars for the rate constants are displayed at 550°C, 525°C, and 500°C.

The maximum and minimum slopes considering the standard deviations at temperatures 500°C and 550°C in Figure A-12 were used to calculate error by another method. The error bounds by this method is ± 76 kJ/mol.

$$E_{a,\ max} = \frac{\ln(k_{max})_{550°C} - \ln(k_{min})_{500°C}}{\Delta\left(\frac{1}{T}\right)} \times 8.314 \frac{J}{K \cdot mol}$$

$$E_{a,\ min} = \frac{\ln(k_{min})_{550°C} - \ln(k_{max})_{500°C}}{\Delta\left(\frac{1}{T}\right)} \times 8.314 \frac{J}{K \cdot mol}$$

Where $\ln(k_{max})$ and $\ln(k_{min})$ at designated temperatures correspond to the maximum and minimum values for ln(k) according to the bounds set by the error bars. Error propagation for the

activation energy of nucleation was calculated. Standard deviations of the measured nucleation densities were used to determine the maximum and minimum nucleation rates.

$$\dot{N}_{max} = \frac{(N_i+\sigma_i)-(N_{i-1}-\sigma_{i-1})}{\Delta t} \quad , \quad \dot{N}_{min} = \frac{(N_i-\sigma_i)-(N_{i-1}+\sigma_{i-1})}{\Delta t}$$

N_i is the last and greatest measured nucleation density for each temperature. N_{i-1} is the second-to-last nucleation density measured in the nucleation density plot (see Figure A-13). The capped lines are the standard deviation and Δt is the time interval between N_i and N_{i-1}.

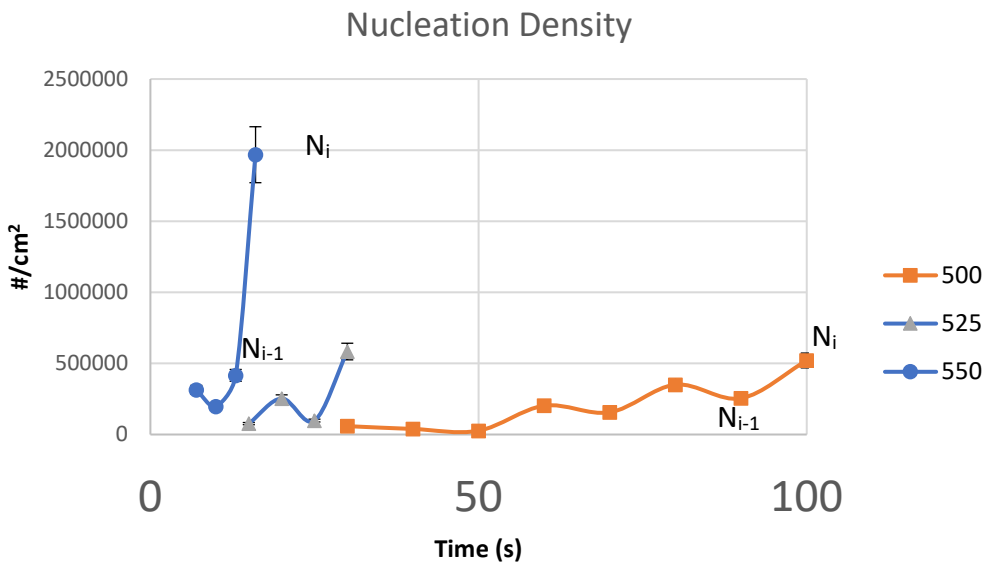

Figure **A-18**: A plot of nucleation density vs. time.

Then the average error for the slope was calculated (± error):

$$\dot{N}_{avg\ error} = \frac{\left|\dot{N}_{max} - \dot{N}_{avg}\right| + \left|\dot{N}_{min} - \dot{N}_{avg}\right|}{2}$$

where the average nucleation rate is the slope between the two points at N_i and N_{i-1}.

Maximum and minimum slopes (activation energies) were calculated for the $\ln(\dot{N})$ vs. 1/T:

$$E_{a,\ max} = \frac{\ln\left(\dot{N}_{min}\right)_{500℃} - \ln\left(\dot{N}_{max}\right)_{550℃}}{\Delta\left(\frac{1}{T}\right)} \times 8.314 \frac{J}{K \cdot mol}$$

$$E_{a,\ min} = \frac{\ln\left(\dot{N}_{max}\right)_{500℃} - \ln\left(\dot{N}_{min}\right)_{550℃}}{\Delta\left(\frac{1}{T}\right)} \times 8.314 \frac{J}{K \cdot mol}$$

$$\pm E_{a,error} = \frac{\left|E_{a,\ max} - E_a\right| + \left|E_{a,\ min} - E_a\right|}{2}$$

The error in activation energy was calculated from the average difference in activation energy between the maximum and minimum, where the error in the maximum nucleation rate in this study is ± 56